

Enhanced Sub-kpc Scale Star-formation: Results From A JWST Size Analysis of 341 Galaxies At $5 < z < 14$

TAKAHIRO MORISHITA ¹, MASSIMO STIAVELLI ², RANGA-RAM CHARY ¹, MICHELE TRENTI ^{3,4},
PIETRO BERGAMINI ^{5,6}, MARCO CHIABERGE ^{7,8}, NICHIA LEETHOCHAWALIT ⁹, GUIDO ROBERTS-BORSANI ^{10,11},
XUEJIAN SHEN ^{12,13} AND TOMMASO TREU ¹⁰

¹*IPAC, California Institute of Technology, MC 314-6, 1200 E. California Boulevard, Pasadena, CA 91125, USA*

²*Space Telescope Science Institute, 3700 San Martin Drive, Baltimore, MD 21218, USA*

³*School of Physics, University of Melbourne, Parkville 3010, VIC, Australia*

⁴*ARC Centre of Excellence for All Sky Astrophysics in 3 Dimensions (ASTRO 3D), Australia*

⁵*Dipartimento di Fisica, Università degli Studi di Milano, Via Celoria 16, I-20133 Milano, Italy*

⁶*INAF - OAS, Osservatorio di Astrofisica e Scienza dello Spazio di Bologna, via Gobetti 93/3, I-40129 Bologna, Italy*

⁷*Space Telescope Science Institute for the European Space Agency (ESA), ESA Office, 3700 San Martin Drive, Baltimore, MD 21218, USA*

⁸*The William H. Miller III Department of Physics and Astronomy, Johns Hopkins University, Baltimore, MD 21218, USA*

⁹*National Astronomical Research Institute of Thailand (NARIT), Mae Rim, Chiang Mai, 50180, Thailand*

¹⁰*Department of Physics and Astronomy, University of California, Los Angeles, 430 Portola Plaza, Los Angeles, CA 90095, USA*

¹¹*Department of Astronomy, University of Geneva, Chemin Pegasi 51, 1290 Versoix, Switzerland*

¹²*TAPIR, California Institute of Technology, Pasadena, CA 91125, USA*

¹³*Department of Physics & Kavli Institute for Astrophysics and Space Research, Massachusetts Institute of Technology, Cambridge, MA 02139, USA*

(Accepted Dec 4, 2023)

Submitted to ApJ

ABSTRACT

We present a comprehensive search and analysis of high-redshift galaxies in a suite of nine public JWST extragalactic fields taken in Cycle 1, covering a total effective search area of ~ 358 arcmin². Through conservative (8σ) photometric selection, we identify 341 galaxies at $5 < z < 14$, with 109 having spectroscopic redshift measurements from the literature, including recent JWST NIRSpec observations. Our regression analysis reveals that the rest-frame UV size-stellar mass relation follows $R_{\text{eff}} \propto M_*^{0.19 \pm 0.03}$, similar to that of star-forming galaxies at $z \sim 3$, but scaled down in size by ~ 0.7 dex. We find a much slower rate for the average size evolution over the redshift range, $R_{\text{eff}} \propto (1+z)^{-0.4 \pm 0.2}$, than that derived in the literature. A fraction ($\sim 13\%$) of our sample are marginally resolved even in the NIRC*am* imaging ($\lesssim 100$ pc), located at $\gtrsim 1.5\sigma$ below the derived size-mass slope. These compact sources exhibit a high star formation surface density $\Sigma_{\text{SFR}} > 10 M_{\odot} \text{ yr}^{-1} \text{ kpc}^{-2}$, a range in which only $< 0.01\%$ of the local star-forming galaxy sample is found. For those with available NIRSpec data, no evidence of ongoing supermassive black hole accretion is observed. A potential explanation for the observed high [O III]-to- $H\beta$ ratios could be high shock velocities, likely originating within intense star-forming regions characterized by high Σ_{SFR} . Lastly, we find that the rest-frame UV and optical sizes of our sample are comparable. Our results are consistent with these early galaxies building up their structures inside-out and yet to exhibit the strong color gradient seen at lower redshift.

1. INTRODUCTION

In a hierarchical universe, dark matter starts collapsing at initial density peaks, giving rise to the underlying structure. Baryons then start accreting in the dark matter potential wells and forming stars. Depending on the initial conditions of gas and dark matter halos, the ap-

pearance of the resulting system may differ dramatically (e.g., Mo et al. 1998; Bullock et al. 2001b).

Within this context, the size of galaxies is a fundamental and essential proxy for understanding galaxy formation and evolution. Galaxies occupy a relative narrow portion of the size and stellar mass/luminosity plane. The distribution of galaxies within this so-called size–stellar mass/luminosity relation, the average size growth rate across cosmic time, and the distribution of other structural parameters, such as the Sérsic index and axis ratio, are key diagnostics of early galaxy formation.

In the local universe, the large statistics enabled by the Sloan Digital Sky survey revealed a fundamental relation of galaxy structures and sizes with mass (e.g., Kauffmann et al. 2003). For example, it has been found that local early-type and late-type galaxies follow different slopes in the size-mass plane (e.g., Shen et al. 2003; Guo et al. 2009; Simard et al. 2011; Cappellari 2013). Such differences are believed to arise from a combination of initial conditions, evolutionary paths, and environmental influences.

In contrast, observations of galaxies at higher redshifts have revealed a variety of galaxy morphologies (Conselice et al. 2004; Wuyts et al. 2011; Guo et al. 2012; Szomoru et al. 2012). These observations indicate active physical processes within and between galaxies, establishing the structural sequences seen in the local universe. Prior to JWST, the Hubble Space Telescope (HST) pushed the frontier of the fundamental galaxy size-mass relation to $z \sim 7$ (Bruce et al. 2012; Mosleh et al. 2012; van der Wel et al. 2012, 2014; Morishita et al. 2014; Allen et al. 2017; Yang et al. 2021). Beyond that redshift, however, the investigation has been severely limited by spatial resolution (~ 1 kpc), as well as the limited number of infrared filters at $> 2 \mu\text{m}$, which is critical to robustly infer galaxy stellar masses. As such, the effort beyond the redshift has been largely limited to small samples of relatively luminous galaxies (Oesch et al. 2010; Ono et al. 2013; Holwerda et al. 2015) or a small volume through strong gravitational lens (Kawamata et al. 2015, 2018; Yang et al. 2022a).

These observable properties are believed to reflect the initial conditions of the gas and dark matter halos from which galaxies form. However, over time, such fundamental properties are susceptible to contamination through a sequence of stochastic, non-linear physical processes, including mergers. Therefore, a detailed characterization of galaxy size becomes imperative, as they may offer insights into not only the physical mechanisms on act, but also their interplay with interstellar medium (e.g., Marshall et al. 2022; Roper et al. 2022a) and the nature of dark matter (e.g., Shen et al. 2023).

Early results from Cycle 1 have already demonstrated the remarkable capabilities of JWST, with its red sensitivity and resolution, revealing early galaxy morphologies down to scales of $\lesssim 100$ pc, throughout rest-frame UV to optical wavelengths (e.g., Yang et al. 2022b; Naidu et al. 2022; Finkelstein et al. 2022; Treu et al. 2023; Morishita & Stiavelli 2023; Huertas-Company et al. 2023; Tacchella et al. 2023; Robertson et al. 2023). Given the substantial number of observations completed in Cycle 1, this study aims to undertake a comprehensive analysis of galaxy sizes, offering the first large scale systematic study of the galaxy size-mass relation at $z > 5$. To achieve this, we perform an analysis based on consistently reduced data from several publicly available extragalactic fields observed during Cycle-1, encompassing a total effective area of ~ 358 arcmin². This extensive coverage enables us to construct a robust sample comprising 341 galaxies within the redshift range of $5 < z < 14$.

The paper is structured as follows: we present our data reduction in Sec. 2, followed by our photometric analyses in Sec. 3. We then characterize the structure of identified galaxies and infer the distributions of their structural parameters in Sec. 4. We investigate the inferred physical properties and discuss the origin of early galaxies in comparison with lower- z galaxies in Sec. 5. We summarize our key conclusions in Sec. 6. Where relevant, we adopt the AB magnitude system (Oke & Gunn 1983; Fukugita et al. 1996), cosmological parameters of $\Omega_m = 0.3$, $\Omega_\Lambda = 0.7$, $H_0 = 70 \text{ km s}^{-1} \text{ Mpc}^{-1}$, and the Chabrier (2003) initial mass function. Distances are in proper units unless otherwise stated.

2. DATA

We base our analysis on nine public deep fields from JWST Cycle 1. For all fields, except for the GLASS/UNCOVER and JADES-GDS fields where the final mosaic images are made publicly available by the teams, we retrieve the raw-level images from the MAST archive and reduce those with the official JWST pipeline, with several customized steps as detailed below. We then apply our photometric pipeline, *borgpipe* (Morishita 2021), on all mosaic images to consistently extract sources and measure fluxes. Our final high- z source candidates are selected by applying the Lyman-break dropout technique (Steidel et al. 1998) supplemented by photometric-redshift selection, as implemented by Morishita & Stiavelli (2022).

2.1. Uniform data reduction of NIRC*am* images

In each field, we start with raw (*uncal.fits*) images retrieved from MAST. We use *Grizli* (ver 1.8.3)

to reduce raw images to generate calibrated images (`cal.fits`). In this step, in addition to the official pipeline’s `DETECTOR` step, `Grizli` includes additional processes for flagging artifacts, such as snowball halos, claws, and wisps.

We then apply `bbpn`¹ on the calibrated images, to subtract $1/f$ -noise. The tool follows the procedure proposed by [Schlawin et al. \(2021\)](#). Briefly, `bbpn` first creates object masks; then it calculates background level in each of the four detector segments (each corresponds to the detector amplifiers) and subtracts the estimated background; it then runs through the detector in the vertical direction and again subtracts the background estimated in each row (that consists of 2048 pixels minus masked pixels); lastly, to compensate for any local over-subtraction of sky near e.g., bright stars or large foreground galaxies, `bbpn` estimates spatially varying background and subtract from the entire image.

After the $1/f$ -noise subtraction step, we align the calibrated images using the `tweakreg` function of the JWST pipeline. For large mosaic fields (i.e. `PRIMER` and `CEERS`), we divide the images into subgroups beforehand and process each of those separately, to optimize computing speed and memory usage. In those fields, images are split into subgroups based on the distance of each image to the other images. We here set the maximum distance of $6'$ for images to be in the same subgroup. We ensure that the images taken in the same visits (i.e. eight detector images for the blue channel and two detector images for the red channel of `NIRCam`) are grouped together, as their relative distance should remain consistent in the following alignment step.

Images in each subgroup are aligned on a filter-by-filter basis. We provide `tweakreg` a set of images associated with source catalogs, generated by running `SExtractor` ([Bertin & Arnouts 1996](#)) on each image. This enables us to eliminate potential artifacts (such as stellar spikes and saturated stars), which are often included by the automated algorithm by `tweakreg`, and secure alignment calculation by using only reliable sources. For all subgroups, each image is aligned to, when available, the WCS reference of a single, contiguous source catalog taken from a large FoV ground-based imaging (see below). This is to avoid alignment issues in some fields and/or subregions, e.g., misalignment in overlapping regions caused by insufficient reference stars. It is noted that `tweakreg` estimates a single alignment solution for images that are taken in the same visit and applies it coherently to those images, such that

the distance between the imaging detectors remains the same for all visits.

Once the images are aligned to the global WCS reference, we drizzle and combine the images into a (sub)mosaic using the pipeline step `IMAGE3`. The pixel scale and pixel frac for drizzling are set to 0.0315 and 0.7 for all filters. For the fields that have multiple subgroups, we then create a single mosaic using a python function `reproject`. Lastly, to eliminate any residual shifts, we once again apply `tweakreg` to a set of multi-band mosaics, but based on the source catalog generated by using the `F444W` mosaic. The images are resampled after the final alignment in the same pixel grid using `reproject`.

2.2. JWST NIRCam Extragalactic Fields

To ensure our selection of high-redshift sources is as consistent as possible, we consider fields that have images in at least six filters (`F115W`, `F150W`, `F200W`, `F277W`, `F356W`, `F444W`). Some fields have additional blue filters (`F070W`, `F090W`) and several medium bands (`F300M`, `F335M`, `F410M`, `F430M`, `F480M`), that extend the search range toward lower redshift and improve photometric redshift estimates. When spectroscopic redshift measurements are available (from either ground or recent JWST observations), we include and use them for photometric flux calibration (Sec. 3.1), as well as for sample selection (spec-z supercede dropout or photo-z).

2.2.1. PAR1199

The `PAR1199` field (11:49:47.31, +22:29:32.1) was taken as part of a Cycle1 GTO program (PID 1199, [Stivelli et al. 2023](#)) in May and June 2023, attached as coordinated parallel to the `NIRSpec` primary, and released immediately without a proprietary period. The `NIRCam` imaging consists of eight filters, including `F090W` and `F410M`, with a total science exposure of ~ 16 hrs with the `MEDIUM8` readout mode. Due to scheduling constraints, the parallel field falls in a field where only shallow (1–2 orbits) `HST ACS F606W` and `F814W` images are available. In addition, because of a bright star that is located near the edge of Module A, the sensitivity limit of the blue channel is slightly shallower in this module compared to the other Module due to the increased scatter light and artifacts. The impact is found to be less in red filters. Galactic reddening is $E(B - V) = 0.024$ mag ([Schlegel et al. 1998](#)). The images are aligned to bright sources in the `Pan-STARRS DR2` catalog ([Chambers et al. 2016](#)). The effective area in the detection image is 10.1 arcmin².

2.2.2. J1235

¹ <https://github.com/mtakahiro/bbpn>

The J1235 field (12:35:54.4631, +04:56:8.50) is one of the low-ecliptic latitude fields that were observed as part of a commissioning program used for NIRC-Cam flatfield (PID 1063, PI Sunnquist). Among the fields available from this program, the J1235 field offers deep NIRC-Cam coverage by 10 filters, including F070W, F090W, F300M, and F480M. Two separate visits were made in March-April 2022 and May 2022. During the first visit, the telescope mirror alignment was not complete, and thus we exclude the data taken during that visit. With the second visit, the exposure time goes as deep as 5.8 hrs in a single filter (with 50.9 hrs in total for the entire field), making it one of the deepest NIRC-Cam multi-band fields. Galactic reddening is $E(B - V) = 0.024$ mag.

The total field coverage extends to ~ 34 arcmin² in the effective detection area, about ~ 3.7 NIRC-Cam footprints; however, some filter images are shifted from others, making the effective area for dropout selection dependent on target redshift. The NIRC-Cam images were aligned to bright sources in the Pan-STARRS DR2 catalog.

2.2.3. North Ecliptic Pole Time-Domain Field

The NIRC-Cam imaging in the North Ecliptic Pole Time-domain field (17:22:47.896, +65:49:21.54; Jansen & Windhorst 2018) was taken as part of a GTO program (PID 2738, Windhorst et al. 2023). The imaging data used here was taken and immediately released after the first epoch of the visit, consisting of eight filters, including F090W and F410M. For the WCS alignment of our JWST data, we use a publicly available catalog that consists of sources observed with the Subaru/HSC instrument (Miyazaki et al. 2018) as part of the Hawaii EROsita Ecliptic pole Survey (HEROES, PI G. Hasinger & E. Hu).² Galactic reddening is $E(B - V) \sim 0.028$ mag. The effective area in the detection image is 16.9 arcmin².

2.2.4. Primer-UDS and COSMOS

Two large NIRC-Cam mosaics are scheduled in a Cycle 1 GO program, Public Release Imaging For Extragalactic Research (PRIMER, PID 1837, PI Dunlop). PRIMER observed two extragalactic fields, the CANDELS UDS and COSMOS fields (Grogin et al. 2011; Koekemoer et al. 2011). The visits are configured with a consistent set of filters (eight filters, including F090W and F410M) and exposure time. In this study, we use the data taken during the first visit in both fields, which covers most of the entire planned fields. However, several images

were identified as failed guide star acquisitions and were removed from our reduction.

The UDS mosaics are aligned to the SPLAXH SXDS catalog (Mehta et al. 2018). We include spec- z measurements available in the same catalog. The COSMOS mosaics is aligned to the COSMOS2020 catalog (Weaver et al. 2022). We include spec- z measurements made by the Keck/DEIMOS instrument and published in Hasinger et al. (2018). Galactic reddening is $E(B - V) \sim 0.023$ mag and 0.017 mag, respectively. The effective area in the detection images are 128.2 arcmin² and 93.9 arcmin².

2.2.5. New Generation Deep Field

The Next Generation Deep Extragalactic Exploratory Public survey, NGDEEP (PID 2079, PI Finkelstein; Bagley et al. 2023a), is a deep spectroscopic+imaging program using the NIRISS WFSS as the primary mode and the NIRC-Cam imaging attached as coordinated parallel in the HUDF-Par2 field (Stiavelli 2005; Oesch et al. 2007; Illingworth 2009). In this study, we use the epoch1 NIRC-Cam imaging data, whereas the epoch2 imaging is currently scheduled in early 2024.

The NIRC-Cam field consists of six filters. Due to the use of the DEEP8 readout mode for many of the NIRC-Cam exposures, a small portion of the final images are severely contaminated by CR hits, which moderately reduces the effective field area and increases the contamination fraction in the high- z source selection. We include spec- z measurements made by the VANDELS collaboration (Pentericci et al. 2018). Galactic reddening is $E(B - V) \sim 0.007$ mag. The effective area in the detection image is 10.2 arcmin².

2.2.6. CEERS

The Cosmic Evolution Early Release Science Survey, or CEERS (Bagley et al. 2023b; Finkelstein et al. 2023), is an ERS program (PID 1345, PI Finkelstein). The data set consists of eight NIRC-Cam filters in the EGS field, previously studied with HST, including as part of CANDELS. The images are aligned to the WCS of the HST F606W image released by the CEERS team (HDR1), which is originally aligned to the GAIA-EDR3 WCS.

The CEERS observations had two separate visits, one in June 2022 (for four sub-regions, #1, 2, 3, 6) and the other in December 2022 (#4, 5, 7, 8, 9, 10). We reduce the NIRC-Cam images separately in each subfield for the reason described in Sec. 2.1. Galactic reddening is $E(B - V) \sim 0.010$ mag.

We include spec- z measurements from multiple studies (Skelton et al. 2014; Momcheva et al. 2016; Roberts-Borsani et al. 2016; Larson et al. 2022), as well as recent JWST spectroscopy studies (Arrabal Haro et al.

² <http://lambda.la.asu.edu/jwst/neptdf/Subaru/index.html>

2023a,b; Harikane et al. 2023a,b; Fujimoto et al. 2023; Larson et al. 2023; Kocevski et al. 2023; Nakajima et al. 2023; Sanders et al. 2023; Tang et al. 2023). The effective area in the detection image is 117.5 arcmin^2 .

2.2.7. GLASS-JWST/UNCOVER

Multiple Cycle 1 programs observed the Abell 2744 field (00:14:21, -30:24:03), including the GLASS-JWST Early Release Science Program (PID 1324; Treu et al. 2022), a Treasury Survey program the Ultradeep NIR-Spec and NIRC*am* Observations before the Epoch of Reionization (UNCOVER, PID 2561; Bezanson et al. 2022), and a JWST DDT program (PID 2756; PI. W. Chen; Roberts-Borsani et al. 2022b). In this study, we utilize the public imaging data made available by the GLASS-JWST team (Merlin et al. 2022; Paris et al. 2023). Their reduction processes include several customized steps, to eliminate detector artifacts. The data set consists of eight NIRC*am* filters, including F090W and F410M. We use the public lens model by Bergamini et al. (2023a) to correct lens magnification of the background sources. We include spectroscopic measurements made available in the literature (Braglia et al. 2009; Owers et al. 2011; Schmidt et al. 2014; Richard et al. 2021; Bergamini et al. 2023b), including those from recent JWST observations (Roberts-Borsani et al. 2022c,b; Morishita et al. 2023; Mascia et al. 2023; Jones et al. 2023). Galactic reddening is $E(B - V) \sim 0.013 \text{ mag}$. The effective area in the detection image is 48.4 arcmin^2 . We hereafter refer to the field as A2744 for the sake of simplicity.

2.2.8. JADES-GDS

We include a deep field from the JWST Advanced Deep Extragalactic Survey (JADES; Robertson et al. 2023; Tacchella et al. 2023; Eisenstein et al. 2023). As of the time of writing, NIRC*am* imaging data in one of the deep fields in the GOODS-South field (3:32:39.3, -27:46:59) are publicly available (Hainline et al. 2023; Rieke & the JADES Collaboration 2023). We retrieve the fully processed images and spectroscopic catalogs made available by the team. The data set consists of nine NIRC*am* filters, including F090W, F335M, and F410M. We include spectroscopic sources listed in the MSA spectroscopic catalog (Bunker et al. 2023), as well as those from the VANDELS survey (Pentericci et al. 2018). Galactic reddening is $E(B - V) \sim 0.007 \text{ mag}$. The effective area in the detection image is 26.7 arcmin^2 .

3. ANALYSIS

3.1. Photometry

The photometric catalog in each field is constructed following Morishita & Stiavelli (2022), using *borgpipe* (Morishita 2021). Briefly, we first prepare a detection image for each field by stacking the F277W, F356W, and F444W filters weighted by each of their RMS maps. Source identification is made in the detection image using SExtractor (Bertin & Arnouts 1996). Fluxes are then estimated for the detected sources with a $r = 0.''16$ aperture. For the aperture flux measurement, images are PSF-matched to the PSF size of F444W beforehand. The image convolution kernels are generated by using *pypher* (Boucaud et al. 2016) on the psf images generated by *webbpsf* (Perrin et al. 2014).

We follow the standard procedure used in the literature (Trenti et al. 2012b; Bradley et al. 2012; Calvi et al. 2016; Morishita et al. 2018; Morishita & Stiavelli 2022), including correction for Galactic extinction and RMS scaling that accounts for correlation noise in drizzled images. Limiting magnitudes of the images are measured by using the same aperture size and reported in Table 1. Aperture fluxes of individual sources are then corrected by applying the correction factor $C = f_{\text{auto},F444W}/f_{\text{aper},F444W}$ universally to all filters, where $f_{\text{auto},F444W}$ is FLUX_AUTO of SExtractor, measured for individual sources. With this approach, colors remain those measured in apertures, whereas the total measurements derived in the following analyses (such as stellar mass, and star formation rate) represent the total fluxes (see also Sec 3.3).

Lastly, since several fields have a number of spectroscopic objects across a wide redshift range, we run *eazypy*, a python wrapper of photometric redshift code *eazy* (Brammer et al. 2008), to fine-tune fluxes across all filters. A set of correction factors for all filters is derived in each field, from the redshift fitting results on those with spectroscopic redshift. The derived correction factors are found to be $< 2\%$ relative to the pivot filter, here set to F150W in all fields, only requiring minor correction.

3.2. Selection of high-redshift galaxy candidates

In what follows, we present our selection of high-redshift galaxies and galaxy candidates. To construct a robust photometric sample, we adopt a two-fold selection method, which has been established in our previous studies (Morishita et al. 2018; Roberts-Borsani et al. 2022a; Ishikawa et al. 2022), and is described in the following two subsections.

3.2.1. Lyman-break dropout selection

Table 1. 5σ -limiting magnitudes (in ABmag).

Field ID	F070W	F090W	F115W	F150W	F200W	F277W	F300M	F335M	F356W	F410M	F444W	F480M
PAR1199	–	29.0	29.0	29.0	29.2	29.4	–	–	29.5	28.9	28.9	–
J1235	28.6	28.6	28.6	28.3	28.9	29.1	28.8	–	29.2	–	28.3	27.7
NEP	–	28.4	28.5	28.6	28.7	29.0	–	–	29.2	28.4	28.6	–
PRIMERUDS [†]	–	27.8	27.8	28.0	28.1	28.4	–	–	28.4	27.6	27.9	–
PRIMERCOS [†]	–	27.8	27.8	28.0	28.1	28.4	–	–	28.5	27.8	28.2	–
NGDEEP	–	–	29.8	29.6	29.7	29.6	–	–	29.7	–	29.2	–
CEERS	–	–	28.7	28.6	28.8	29.0	–	–	29.0	28.2	28.5	–
A2744	–	29.2	28.9	28.8	28.8	29.0	–	–	29.1	28.5	28.9	–
JADESGDS	–	29.6	29.9	29.8	29.9	30.2	–	29.6	30.1	29.6	29.8	–

NOTE— Limiting magnitudes measured in empty regions of the image with $r = 0.''16$ apertures. [†]: Mosaic images have been created using the first epoch data that are available as of June 2023.**Table 2.** Numbers of the final sources in fields.

Field	F070W-d	F090W-d	F115W-d	F150W-d
PAR1199	0 (0)	7 (0)	0 (0)	0 (0)
J1235	20 (0)	1 (0)	0 (0)	0 (0)
NEP	0 (0)	11 (0)	0 (0)	0 (0)
PRIMERUDS	0 (0)	44 (0)	10 (0)	0 (0)
PRIMERCOS	2 (2)	24 (0)	3 (0)	1 (0)
NGDEEP	1 (1)	0 (0)	1 (0)	0 (0)
CEERS	33 (33)	8 (8)	9 (2)	0 (0)
A2744	19 (19)	15 (9)	10 (1)	0 (0)
JADESGDS	26 (26)	86 (5)	9 (2)	1 (1)
ALL	101 (81)	196 (22)	42 (5)	2 (1)

NOTE— “-d” represents dropout. Numbers of spectroscopically confirmed sources (see Sec. 3.2.3) are shown in brackets.

Here we identify dropout sources in four redshift ranges. For those detected at Signal-to-noise ratio (S/N) > 4 in the detection band, we apply one of the following criteria:

F070W-dropouts ($5.0 < z < 7.2$)

$$S/N_{115} > 8$$

$$S/N_{070} < 2.0$$

$$z_{\text{set}} = 4.5$$

F090W-dropouts ($7.2 < z < 9.7$)

$$S/N_{150} > 8$$

$$S/N_{090,070} < 2.0$$

$$z_{\text{set}} = 6$$

F115W-dropouts ($9.7 < z < 13.0$)

$$S/N_{200} > 8$$

$$S/N_{115,090,070} < 2.0$$

$$z_{\text{set}} = 8$$

F150W-dropouts ($13.0 < z < 18.6$)

$$S/N_{277} > 8$$

$$S/N_{150,115,090,070} < 2.0$$

$$z_{\text{set}} = 10$$

where S/N is measured in a $r = 0.''16$ aperture. In each redshift range, we ensure secure selection by requiring a $S/N > 8$ detection in a filter that covers rest-frame UV ($\sim 1600 \text{ \AA}$, but not including the blue side of Lyman break). This stringent requirement ensures high completeness ($> 50\%$) and reliable size measurements (Appendix C). For the source to be selected as dropout, we require non-detection of fluxes ($S/N < 2$) in all available dropout filters (listed as subscripts above). Furthermore, to secure the non-detection, we repeat the non-detection step with a smaller aperture, $r = 0.''08$ (~ 2.5 pixel). Note that a photometric selection is not attempted for fields where no dropout filter is available (but see Sec. 3.2.3).

A major difference from the conventional Lyman break technique in the literature (e.g., Bouwens et al. 2023a) is that our selection method above does not cut samples based on the color of the rest-frame UV but only on the strength of Lyman break. The choice is made to preserve as many potential sources as possible and make the selection comprehensive — for example, in a conventional color-cut selection, sources may be dismissed for

their color that *barely* miss the selection window, even if the color is consistent within the photometric uncertainty. This also means that the fraction of low- z interlopers misidentified as high- z sources is likely increased with regard to the standard technique. Therefore, we further secure the sample in the following step.

3.2.2. Photometric-redshift selection

We here secure the dropout sources by applying photometric-redshift selection to the dropout sources selected above. This is to minimize the fraction of low- z interlopers, such as galaxies of relatively old stellar populations (e.g., Oesch et al. 2016) and with dust extinction, or foreground dwarfs (e.g., Morishita et al. 2020). Such interlopers are often distinguished by their distinctive red color, readily discernible in our wavelength coverage with NIRC*am*.

To estimate photometric redshifts, we run `eazy` with the default magnitude prior (Fig. 4 in Brammer et al. 2008). The fitting redshift range is set to $0 < z < 30$, with a step size of $\log(1+z) = 0.01$. By comparing photometric redshifts with spectroscopic ones, we find that the template library provided by Hainline et al. (2023) offers an improved photometric redshift accuracy over the default (v1.3) template library, and thus in this work we adopt the former.

Following Morishita et al. (2018), we exclude sources that satisfy $p(z < z_{\text{set}}) > 0.2$, i.e. total redshift probability at $z < z_{\text{set}}$ is greater than 20%, where z_{set} is set separately for each selection redshift range (see Sec. 3.2.1). To eliminate potential contamination by cool (T/L/M-type) stars (i.e. brown dwarfs), we follow Morishita (2021) and repeat the phot- z analysis with dwarf templates. A set of dwarf templates taken from the IRTF spectral Library (Rayner et al. 2003) is provided to `eazy` and fit to the data with redshift fixed to 0. The fitting result is inferred for every photometric source that is unresolved (see Sec. 4.4), and the source is removed if the χ^2/ν value is smaller than the one from the galaxy template fitting above. We have excluded 60 sources in this step.

Lastly, we visually inspect all sources that pass the two selections above. In this step, we exclude any suspicious sources whose flux measurements may be significantly affected, including those with residuals of CRs, close to/overlapping with a brighter galaxy (caused by deblending), misidentified stellar spikes, and those near the detector edge where a part of the source is truncated. We have discarded 342 sources.

3.2.3. Spectroscopic Sample

In addition to the photometric sample constructed above, we include those with spectroscopic redshift con-

firmed by previous spectroscopic observations as described in Sec. 2.2. We add sources when their spectroscopic redshift is within the redshift range defined for each selection window *and* when they satisfy detection criteria in the detection ($S/N > 4$) and rest-frame UV (> 8) bands.

The addition of spec- z sources aids in particular the F070W-dropout sample, which would need F070W as a non-detection filter. All fields except for J1235 do not have the filter coverage, leaving the sample size relatively small without spectroscopically confirmed objects. On the other hand, this could introduce a potential bias toward strong line emitters. However, in Sec. 4.2 we investigate this in our size-mass analysis and find that the addition of spec- z sources does not impact any of our final conclusions.

3.3. Size measurements

Our primary analysis is based on the size measurement of galaxies. Following standard practice, we adopt the Sérsic profile (Sérsic 1963):

$$I(r) \propto \exp[-b_n \left(\frac{r}{R_e}\right)^{1/n} - 1] \quad (1)$$

where size is characterized by the effective radius, R_e , which encloses half of the total light of the galaxy. n is the Sérsic index and b_n is an n -dependent normalization parameter. We model the two-dimensional light profile of each galaxy using `galfit` (Peng et al. 2002, 2010).

We follow Morishita et al. (2014, 2017) for detailed procedures, with a few modifications to accommodate efficiency and accuracy. Briefly, for each galaxy, we first generate image cutouts (here set to 151×151 pixel in size, equivalent to $4.''8 \times 4.''8$) of original (i.e. pre-psf matched) science map, rms map, and segmentation map. We fix Sérsic index n to 1, a value that is found to offer reasonable fit to high- z Lyman-break galaxies in the literature (Shibuya et al. 2015; Yang et al. 2022a; Ono et al. 2022). As a test, we repeated the analysis with n as a free parameter and indeed found its distribution to be centered around ~ 1 . However, this led to an increased fraction ($\sim 13\%$) of unsuccessful fits, where the solutions either did not converge or converged to unrealistic parameters (i.e. $n < 0.2$ or $n > 10$). To mitigate potential bias from this constraint, we reevaluate the uncertainty of each size measurement by adding the difference in R_e resulting from the two procedures (n -fixed and n -free) in quadrature. Consequently, those with n deviating significantly from 1 incur a larger uncertainty in the size measurement.

The psf image generated by `webbpsf` of the corresponding filter is fed to `galfit`, for convolution of the

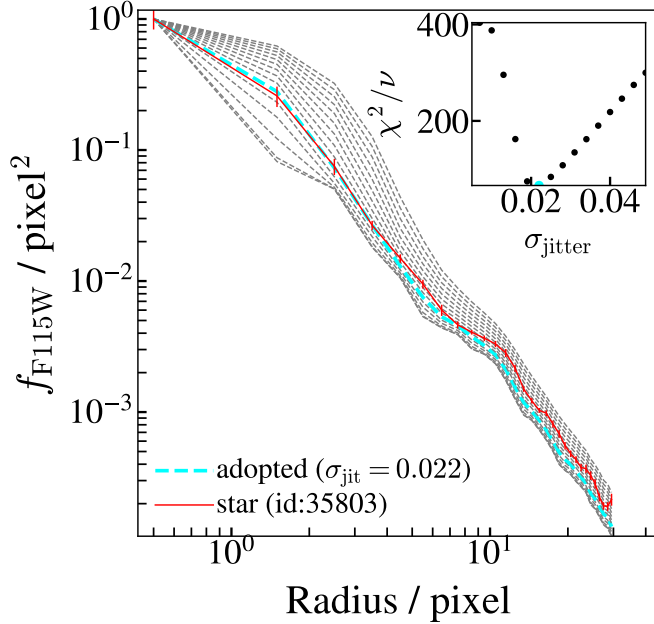


Figure 1. Radial flux profiles of `webbpsf` with various σ_{jitter} values (dashed lines) generated for the JADESGDS F115W image, where the adopted profile ($\sigma_{\text{jitter}} = 0.022$) is color-coded in cyan. The profile of an example bright star taken from the image is shown for comparison (red solid line). The inset shows the distribution of χ^2/ν of the same star fitted by the `webbpsf` for different σ_{jitter} values.

model profile at each iteration. The psf image is generated for each field by retrieving the Optical Path Difference files of the observed date³. As reported in several studies (Ono et al. 2022; Tacchella et al. 2023; Ito et al. 2023), we find that the default output of `webbpsf` exhibits a narrower psf profile compared to observed stars in our reduced images. This is potentially caused by e.g., drizzling/resampling of the actual images, as well as jitter in pointing, which could affect more significantly in a longer exposure. We therefore find an optimal psf that describes the actual psf size of our image by tweaking the `jitter.sigma` parameter of `webbpsf`. To do this, we visually identify unsaturated, bright stars that do not have any companion within < 50 pixels. We then fit these stars with various psf models by using `galfit` and select a model that offers the minimum χ^2 value. While it is ideal to repeat the analysis and determine the jitter value in each field, some fields do not have sufficient number of stars that can be used for this. We thus adopt the median value that is determined by stars in all fields for each filter. Figure 1 shows an example radial flux profile of an actual star, compared with those of `webbpsf` generated with different σ_{jitter} values. The

final `jitter.sigma` value is set ~ 0.022 arcsec for the blue-channel filters and ~ 0.034 arcsec for the redder channel.

Neighboring sources that are close to and relatively bright compared to the main galaxy are fit simultaneously, while the rest of the sources in the stamp are masked using the segmentation map generated by `SExtractor` above. We include any neighbouring source at distance d from the main galaxy when its flux is above the limiting flux defined as:

$$f_{\text{nei,lim}} = \gamma f_{\text{main}} (d/d_s)^{\alpha_{\text{nei}}}, \quad (2)$$

with $\gamma = 0.8$, $\alpha_{\text{nei}} = 2.0$, and $d_s = 60$ pixel.

We run `galfit` in the order of the target source magnitudes. The fitting results of the primary galaxy are continuously stored, so that the parameters for the repeated galaxies are fixed to the previously determined values when they appear in the cutout of a fainter galaxy later in the fitting session.

For each galaxy, we repeat the fit in two filters that corresponds to rest-frame UV and optical wavelengths. We then inspect all fitting results to ensure the measurements. We have flagged 24 sources that show significant residuals, e.g., from multiple clumps within the defined segment region and/or clear features of interaction with nearby sources. These flagged sources are excluded from statistical analyses in the following sections. The measured sizes are presented in Appendix.

3.4. Physical Properties inferred by spectral energy distribution analysis

We infer the spectral energy distribution (SED) of the individual galaxies through SED fitting using photometric data that covers $0.6\text{--}5\ \mu\text{m}$. We use the SED fitting code `gsf` (ver1.8; Morishita et al. 2019), which allows flexible determinations of the SED by adopting binned star formation histories, also known as *non-parametric*. `gsf` determines an optimal combination of stellar and interstellar medium (ISM) templates among the template library. For this study, we generate templates of different ages, [10, 30, 100, 300, 1000, 3000] Myrs, and metallicities $\log Z_*/Z_\odot \in [-2, 0]$ at an increment of 0.1 by using `fsps` (Conroy et al. 2009; Foreman-Mackey et al. 2014). A nebular component (emission lines and continuum) that is characterized by an ionization parameter $\log U \in [-3, -1]$ is also generated by `fsps` (see also Byler et al. 2017) and added to the template after multiplication by an amplitude parameter. Dust attenuation and metallicity of the stellar templates are treated as free parameters during the fit, whereas the metallicity of the nebular component is synchronized with the metallicity of the stellar component during the fitting process.

³ https://webbpsf.readthedocs.io/en/latest/available_opds.html

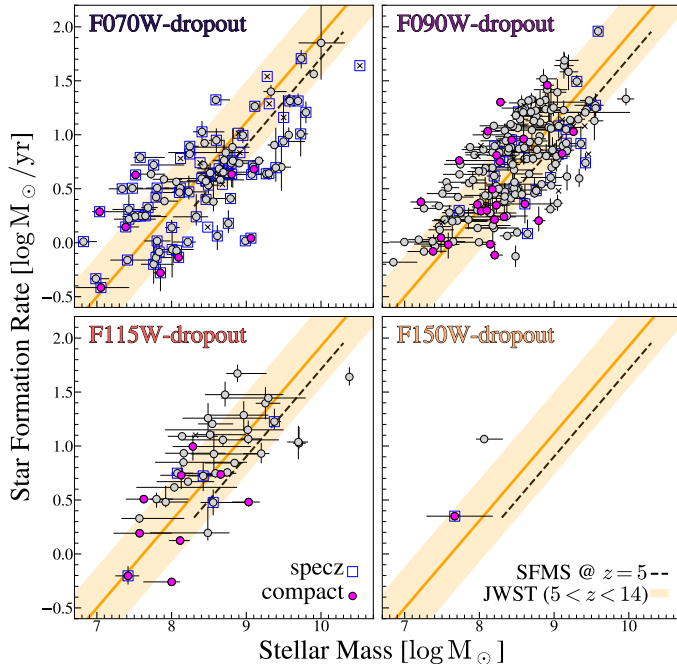


Figure 2. Sample distribution in the star formation rate–stellar mass plane (circles). Those with spectroscopic redshift (blue square) and flagged as compact (magenta; Sec. 4.4) are marked accordingly. Those flagged in *galfit* results (Sec. 3.3) are shown by open symbols. The SFMS slope at $z = 5$ (black dashed lines; Speagle et al. 2014), the linear regression slope derived for our entire sample, $\log \text{SFR} = 0.81 \log(M_*/10^8 M_\odot) + 0.31$ (with the slope fixed to the Speagle et al. 2014’s at $z = 5$), and the derived range for the intrinsic scatter (0.37 dex; shaded regions) are shown.

The posterior distribution of the parameters is sampled by using *emcee* for 10^4 iterations with the number of walkers set to 100. The final posterior is collected after excluding the first half of the realizations (known as burn-in). The resulting physical parameters (such as stellar mass, star formation rate, rest-frame UV slope β_{UV} , metallicity, dust attenuation A_V , and mass-weighted age) are quoted as the median of the posterior distribution, along with uncertainties measured from the 16th to 84th percentile range. The star-formation rate of individual galaxies is calculated with the rest-frame UV luminosity ($\sim 1600 \text{ \AA}$) using the posterior SED. The UV luminosity is corrected for dust attenuation using the β_{UV} slope, which is measured by using the posterior SED, as in Smit et al. (2016):

$$A_{1600} = 4.43 + 1.99 \beta_{\text{UV}} \quad (3)$$

The attenuation corrected UV luminosity is then converted to SFR via the relation in Kennicutt (1998):

$$\text{SFR} [M_\odot \text{ yr}^{-1}] = 1.4 \times 10^{-28} L_{\text{UV}} [\text{erg s}^{-1} \text{ Hz}^{-1}]. \quad (4)$$

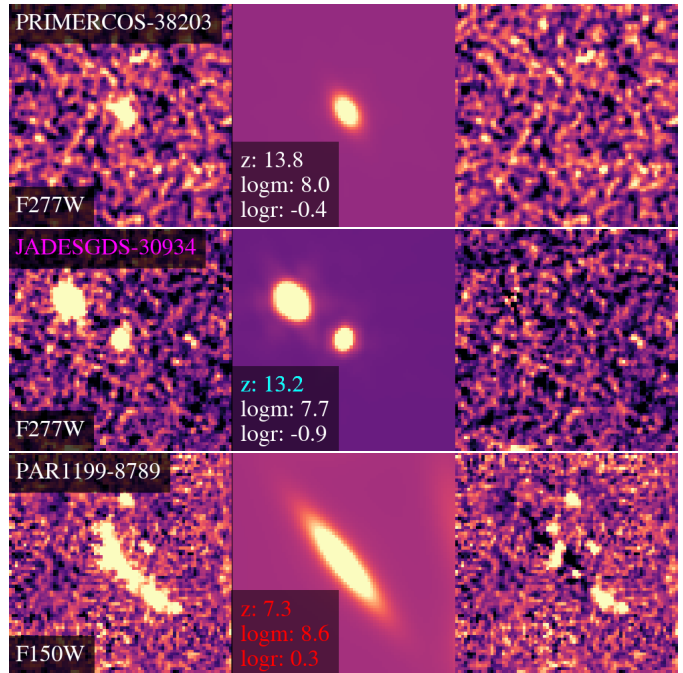


Figure 3. Example of *galfit* fitting results in 2D-images (left: original, middle: model, right: residual). (top row): PRIMERCOS-38203, one of the highest redshift sources in our sample. (middle row): JADESGDS-30934 (spectroscopically confirmed to $z = 13.2$; Curtis-Lake et al. 2023), an example of those classified as compact (Sec. 4.4). (bottom row): F090W-dropout source that is flagged in *galfit* fitting analysis. Flagged objects are not included in our statistical discussion.

Lastly, we correct both stellar mass and star formation rate measurements to the total model magnitude derived by *galfit*, as in Morishita et al. (2014), by multiplying the correction factor:

$$C_{\text{galfit}} = 10^{-0.4(m_{\text{galfit}} - m_{\text{total}})} \quad (5)$$

where m_{galfit} is the best-fit total magnitude derived by *galfit* and m_{total} is the total magnitude derived in Sec. 3.1, both measured in the rest-frame UV filter of interest for the target redshift range. Sources flagged in the *galfit* results are set $C_{\text{galfit}} = 1$. The inferred physical properties are presented in Appendix.

4. RESULTS

4.1. Overview of the final sample

In Table 2, we report the number of our final sources selected in each field and dropout selection window. From all fields, we identify 101 F070W-dropout sources (81 of which are spec- z confirmed), 196 F090W-dropout sources (22), 42 F115W-dropout sources (5), and 2

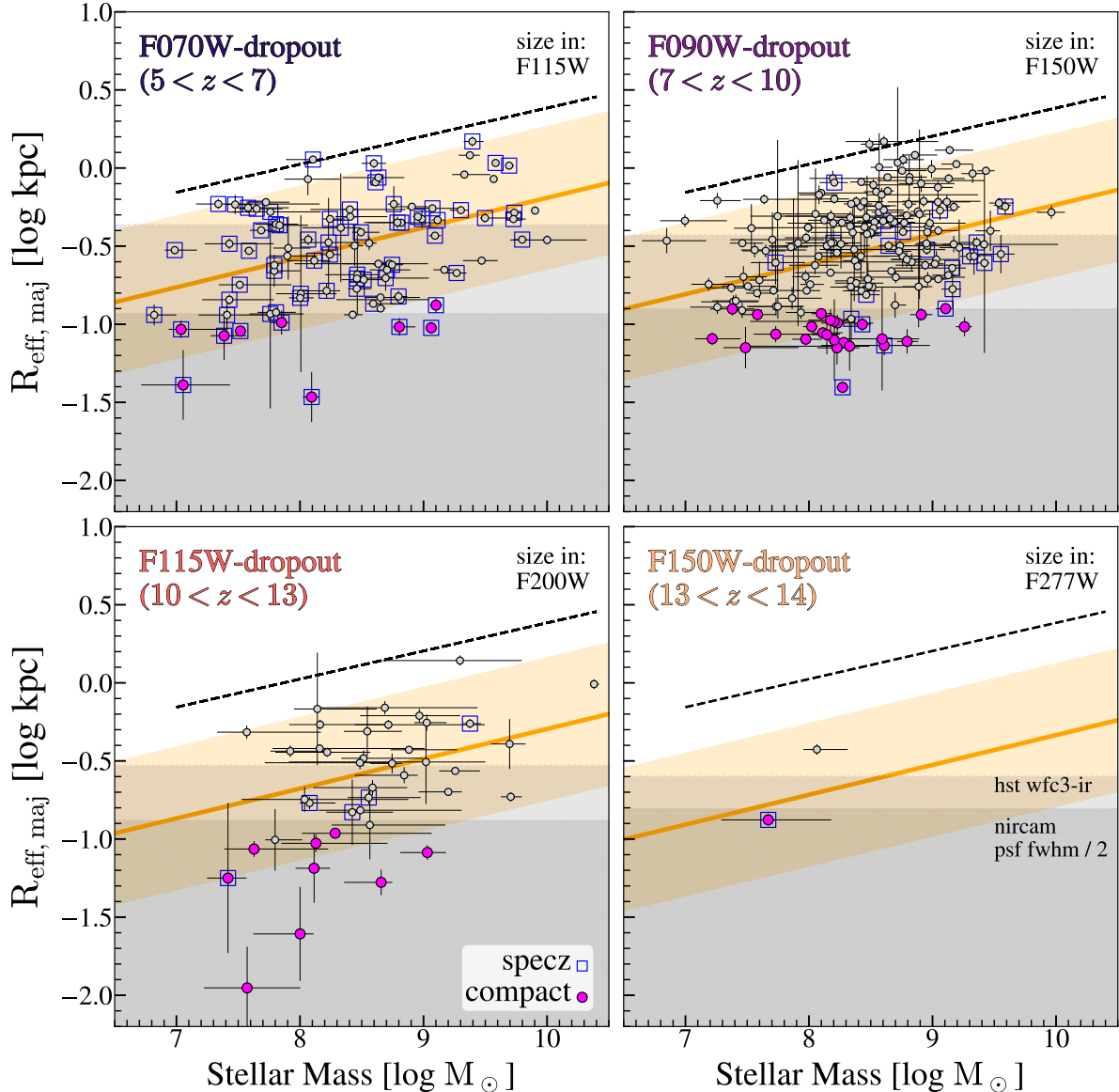


Figure 4. Distribution of our sample galaxies at $5 < z < 14$ in the stellar mass-size plane (gray circles), in four redshift panels. The linear slope derived by regression analysis for the full sample (orange solid lines, with the shaded regions covering the $\pm 1.5\sigma_{\log R_e}$ range from the median slope; Table 3) is shown. For comparison, the slope derived for late-type galaxies at $z \sim 2.7$ (van der Wel et al. 2014, black dashed lines) is shown. Those classified as compact (Sec. 4.4) are shown by magenta symbols. Those with spectroscopic redshift are marked by open blue squares. Two horizontal hatched regions show the physical size of FWHM/2 for NIRCAM (dark gray) and HST/WFC3-IR F160W (light gray) at the median redshift of the sources in each redshift window.

F150W-dropout sources (1). As we present in the following sections, the sample spans a wide range of stellar mass ($6.8 \lesssim \log M_*/M_\odot \lesssim 10.4$) and absolute UV magnitude ($-23 \lesssim M_{UV}/\text{mag} \lesssim -17$). The final sources are identical when a larger aperture ($0''.32$) is adopted for the source selection in Sec. 3.2.1.

In Fig. 2, we show the distribution of the final sample in the stellar mass-star formation rate plane. Despite the wide mass (more three orders of magnitude) and

redshift ($5 < z < 14$) ranges, our galaxies are found to distribute along a sequence, suggesting that most of our sample galaxies are a typical star-forming population. To compare the location of our galaxies with those at lower redshift, we derive a linear regression, with the slope fixed to 0.81 i.e. the one for $z = 5$ using the formulae of Speagle et al. (2014). The regression is derived to be $\log \text{SFR} = 0.81 \log(M_*/10^8 M_\odot) + 0.31$, with the intrinsic scatter of 0.37 dex.

Table 3. Size–Mass Relations of Galaxies at $5 < z < 14$: Linear Regression Best-Fit Coefficients

All sample					Resolved sample ($R_e > \text{FWHM}/2$)				
N	α	β_z	α_z	$\sigma_{\log R_e}$	N	α	β_z	α_z	$\sigma_{\log R_e}$
317	$0.19^{+0.03}_{-0.03}$	$-0.21^{+0.20}_{-0.20}$	$-0.44^{+0.21}_{-0.21}$	$0.30^{+0.01}_{-0.01}$	278	[0.19]	$-0.33^{+0.18}_{-0.18}$	$-0.24^{+0.20}_{-0.20}$	$0.25^{+0.01}_{-0.01}$

NOTE— Best-fit coefficients for the single slope regression, $\log R_e/\text{kpc} = \alpha \log(M_*/10^8 M_\odot) + B(z)$, where $B(z) = \beta_z + \alpha_z \log(1+z)$. Note that $\sigma_{\log R_e} = \sigma_{\ln R_e} / \ln(10)$.

While the full details of the selected sources will be presented in a forthcoming paper, we highlight two F150W-dropout galaxies ($z \gtrsim 13$). One, JADESGDS-30934, is spectroscopically confirmed to be at $z = 13.2$ (Curtis-Lake et al. 2023). The other object, PRIMERCOS-38203, is a newly identified photometric candidate source at $z = 13.8^{+1.1}_{-1.0}$ in the PRIMERCOSMOS field (Fig. 3). Despite the relatively shallow depth in the field, the source exhibits clean non-detection in F090W, F115W, and F150W and high-S/N detection in F200W (S/N=9.2) and in the IR-detection band (S/N=16.1). The observed UV magnitude ($M_{\text{UV}} = -20$ mag) and the derived stellar mass ($\log M_*/M_\odot = 8.0$) are both moderate and comparable to other galaxy candidates at these redshift (e.g., Morishita & Stiavelli 2023; Finkelstein et al. 2023; Bouwens et al. 2023b). While the F200W-dropout selection covers up to $z \sim 18.6$, none is identified at $z > 14$ in our selection. The number density estimates of the identified sources will be presented in a forthcoming paper. Another potentially interesting source is PRIMERUDS-121885 at $z = 10.9^{+0.3}_{-0.3}$, whose stellar mass is $\log M_*/M_\odot = 10.4^{+0.1}_{-0.1}$. This object has relatively red F356W–F444W color (0.76 mag), which implies the presence of old populations. However, we caution that the source is identified in PRIMERUDS, which is relatively shallow among the fields. In addition, at the redshift of the source the F444W flux could also be attributed to strong $\text{H}\beta + [\text{O III}]$ emissions, which would lead to a smaller stellar mass.

Lastly, we observe moderate concentration of sources at $z \approx 7$ –7.6. This is partially attributed to that strong $\text{H}\beta + [\text{O III}]$ emitters are more sensitive to our selection, due to the two medium band filters (F410M and F430M) by their making photometric redshift relatively more constrained. Besides, there is an overdensity of emitters identified in the same redshift range in one of the fields (Daikuhara, in prep.).

4.2. Size-Stellar Mass Distribution of Galaxies at $5 < z < 14$

In Fig. 4, we show the distribution of galaxies in the size-mass plane for the four redshift ranges. In each

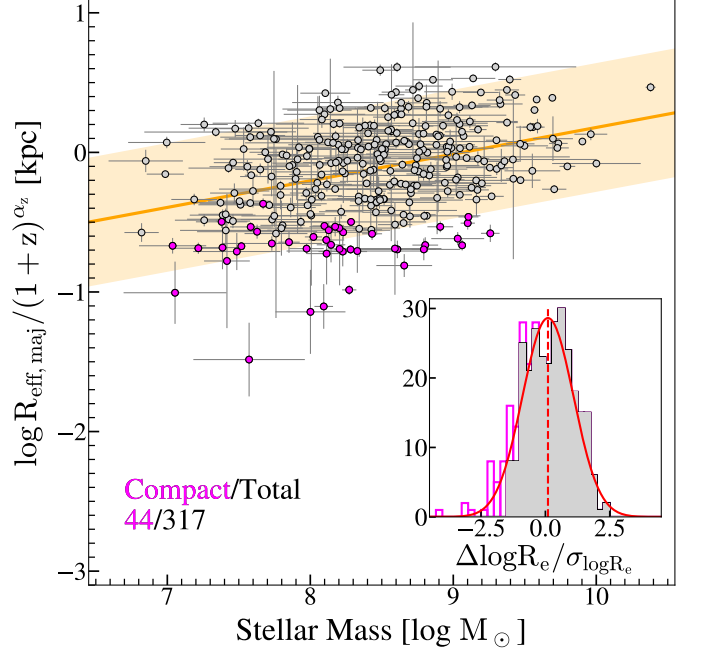


Figure 5. Same as in Fig. 4 but for redshift-corrected size ($= R_{\text{eff,maj}}/(1+z)^{\alpha_z}$) of all sources (gray dots) along the determined regression slope (orange solid line, with shades for the $\pm 1.5 \sigma_{\log R_e}$ range). In the inset, the distribution of the normalized size, $\Delta R_e / \sigma_{\log R_e}$ is shown, where ΔR_e is the distance from the regression for a given stellar mass. The distribution of the compact sources (open magenta) is shown separately from the remaining extended sources. The Gaussian fit to the extended sources (solid red line) highlights the excess.

redshift panel, we show the size measured in the filter that corresponds to rest-frame $\sim 1600 \text{ \AA}$ i.e. F115W for the F070W-dropout, F150W for the F090W-dropout, F200W for the F115W-dropout, and F277W for the F200W-dropout selection. We adopt the effective radius measured along the major axis, to mitigate the effect by inclination.

The measured size spans a broad range, $\log R_e / \text{kpc} \sim -2$ – -0.3 . Remarkably, at $\log M_*/M_\odot < 9$, many galaxies are characterized by $R_e < 0.3 \text{ kpc}$ ($< 0''.07$), which is below the resolution limit afforded by HST/WFC3-IR. Thus, the spatial resolution of NIRCcam, \sim

0.11–0.14 kpc, is essential to study typical star-forming galaxies at these redshift (see also Sec. 4.4).

We investigate their distribution on the size-mass plane by linear regression analyses. By following Shen et al. (2003, also Ferguson et al. 2004; van der Wel et al. 2014), we parameterize size by a log-normal distribution as a function of stellar mass and redshift:

$$\log R_e(M_*, z)/\text{kpc} = \alpha \log(M_*/M_0) + B(z), \quad (6)$$

where we describe the intercept as

$$B(z) = \beta_z + \alpha_z \log(1 + z). \quad (7)$$

We adopt a pivot mass $M_0 = 10^8 M_\odot$. The model distribution, $N(\log R_e(M_*), \sigma_{\log R_e})$, prescribes the probability distribution for observing $\log R_e$ for a galaxy with the stellar mass M_* with an intrinsic scatter of $\sigma_{\log R_e}$. By making the intercept $B(z)$ a function of redshift, we are able to evaluate the size distribution with a consistent slope determined by the entire sample. Although the redshift evolution of the slope is of interest, previous studies have reported little changes over a much broader cosmic time range than what is explored in this study (e.g., van der Wel et al. 2014; Shibuya et al. 2015). As we demonstrate below, our findings also reveal no significant evolution in slope from these studies, supporting our employing a single slope across the entire redshift range.

The regression is determined by using `emcee` (Foreman-Mackey et al. 2014), with the number of walker is set to $N = 50$ and the iteration to 10^4 . We only include those not flagged in structural fitting analysis in Sec 3.3. Measurements uncertainties in size, stellar mass, and redshift are used in the calculation of likelihood. The derived regression is shown in Fig. 4 along with the measured sizes in four redshift panels. In Fig. 5, we also show the redshift-corrected size, $R_e/(1+z)^{\alpha_z}$, as this represents the actual variants evaluated in the fitting. We report the determined parameters in Table 3.

The derived slope, $\sim 0.20 \pm 0.03$, is similar to what was found in Mosleh et al. (2011, ~ 0.3) for Lyman Break galaxies at $z \sim 3.5$ and van der Wel et al. (2014, 0.18–0.25) for late-type galaxies at $z \sim 0.3$ –3, despite the latter being observed in different rest-frame wavelengths (but see the following and Sec 5.3). The slope of the size-mass relation would reflect the interplay between the intrinsic compactness and concentrated dust attenuation in the core of massive star-forming galaxies at high redshift (Roper et al. 2022b). In fact, negative slopes of the size-mass and size-luminosity relations have been found in cosmological simulations, e.g. BlueTides (Marshall et al. 2022), IllustrisTNG (Popping

et al. 2022; Costantin et al. 2023), FLARES (Roper et al. 2022a), and THESAN (Shen et al. 2023, in prep.) simulations. Our finding of a positive slope is consistent with the idea that some massive galaxies in our sample may already possess a moderate amount of dust in its core.

We note that the derived intrinsic scatter, $\sigma_{\log R_e}$, is relatively large (~ 0.3) compared to those at lower redshift in the literature (~ 0.2). The scatter in size distribution is ought to reflect the initial condition of dark matter halos, such as the distribution of spin parameter (e.g., Bullock et al. 2001a). Thus, the observed larger scatter would imply the presence of galaxies that experienced non-linear behavior, such as merger and other dissipative processes, and deviate from the distribution predicted by a simple galactic disc formation model (e.g., Mo et al. 1998). In fact, we observed a number of galaxies that are barely resolved in the NIRCcam images, some of which are located far below ($> 1.5\sigma$) the derived regression (Sec. 4.4). We repeat the regression analysis by excluding these unresolved sources but with the slope fixed to the one derived above. The derived scatter from this regression is ~ 0.25 , moderately reduced from the analysis of the full sample (Table 3).

Our sample includes both spectroscopic and photometric sources. In particular, the majority ($\sim 90\%$) of the F070W-d sample are spectroscopic, due to the lack of F070W-filter coverage. To investigate the impact by the spectroscopic sources, we repeat the regression analysis by only using photometric sources. We find a consistent result ($\alpha = 0.23 \pm 0.04$, $\beta_z = -0.10 \pm 0.32$, and $\alpha_z = -0.56 \pm 0.33$), within the uncertainty range. The slight decrease in α_z ($+0.14$, stronger z -evolution) can be attributed to the fact that the spectroscopic sources are smaller in size than photometric sources and that they dominate the lowest redshift bin. These differences in the regression result do not change our conclusion.

4.3. Redshift Evolution of Galaxy Sizes

In Fig. 6, we show the redshift trend of the UV sizes derived through the regression analysis above. We note that the redshift evolution represent, by design, for the mass-corrected size, $R_e/(M_*/M_0)^\alpha$. We find that the derived redshift evolution, $\propto (1+z)^{\alpha_z}$ with $\alpha_z \sim -0.4 \pm 0.2$, is much less significant than the one derived for rest-frame UV ($\sim 2100 \text{ \AA}$) size of Lyman-break galaxies at $0 < z < 7$, with $\alpha_z = -1.2 \pm 0.1$ (Mosleh et al. 2012, also Oesch et al. 2010; Shibuya et al. 2015 who found a similar value).

The primary cause of the discrepancy can be attributed to the redshift range of the sample. The aforementioned studies derived the redshift evolution by in-

cluding lower-redshift galaxies ($z \lesssim 1$ in Mosleh et al. 2012; Shibuya et al. 2015 and $2 < z < 8$ in Oesch et al. 2010). Indeed, Curtis-Lake et al. (2016) found a much slower evolution, α_z , for the LBG sample at $4 < z < 8$, and argued that the discrepancy is partially attributed to a stronger evolution in UV sizes at $z < 5$ (see also Oesch et al. 2010, who found little size evolution from $z \sim 7$ to 6).

To investigate this, we derive the redshift evolution by combining the median sizes presented in Fig. 6 and in Mosleh et al. (2012, for $1 < z < 7$), and we do find a stronger evolution ($\alpha_z \sim -1.2$). This supports the idea that the redshift evolution of the average UV size is much slower at $z > 5$ than lower redshifts. However, we note that the outcomes is likely subject to a range of systematic factors, such as the weighting of each size measurement, the inclusion or exclusion of specific data points, and potential sample mismatches.

In Fig. 6, we also show the evolution of rest-frame optical sizes derived for low-mass ($\log M_*/M_\odot \sim 9$) late-type galaxies at $0 < z < 2$ (van der Wel et al. 2014). Interestingly, the extrapolated sizes from the fit to our redshift range exhibit a significant offset, even after accounting for the mass difference between the two samples. Although the offset might be attributed to differences in the bands used for size measurements (i.e. rest-frame 5000 Å in van der Wel et al. 2014), we find that our galaxies, on average, do not show a significant offset between the two bands. This reinforces our earlier interpretation that size evolution could be more pronounced at $z \lesssim 5$, primarily driven by the build-up of massive bulges and/or outskirts, which would enhance color gradients, as seen at lower redshifts. We discuss this in more detail in Sec. 5.3.

4.4. Identifying Blue Compact Sources

In our size analysis above, we have identified a number of compact sources that are near the resolution limit of NIRCcam. Previous studies using NIRCcam data also reported a few of such compact sources (Yang et al. 2022a; Castellano et al. 2022; Naidu et al. 2022; Ono et al. 2022). We define those that satisfy either of the following as *compact*:

- i) $R_e < \text{FWHM}/2$ in the measured band; or
- ii) $\Delta R_e < -1.5 \sigma_{\log R_e}$

where ΔR is the difference of the measured size from the inferred size by the linear regression for the stellar mass and redshift of the source. Note that R_e used here is apparent size.

With the criteria, we find 44 compact sources from our sample ($\sim 13\%$), including 15 that are spectroscopically

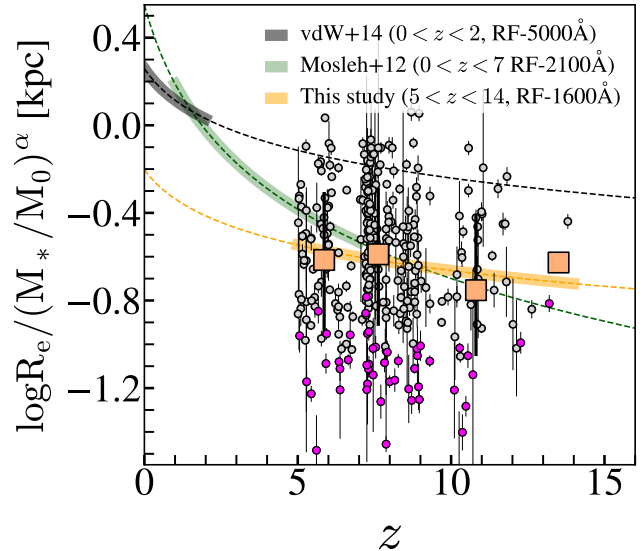


Figure 6. Redshift evolution of rest-frame UV size of our galaxies (gray circles). The size of individual galaxies shown here is corrected to the pivot mass (Sec. 4.2). The redshift evolution of the intercept, $\propto (1+z)^{\alpha_z}$, is shown (orange dashed line), along with those derived in two previous studies (green line for Mosleh et al. 2012 and black line for van der Wel et al. 2014). We note that the size trend of both previous studies is also scaled to the same pivot mass. Median sizes (large symbols) are derived in each redshift window. Those identified as compact (Sec. 4.4) are shown by magenta symbols.

confirmed. We then exclude five of the classified compact sources, whose SED is better fitted with a brown dwarf template over galaxy templates (Sec. 3.2). The classified compact sources are marked in Fig. 4. Individual cutout images are presented in Appendix 4.

In Fig. 5, we show the distribution of the normalized size, $\Delta R_e / \sigma_{\log R_e}$. The distribution clearly shows an excess at smaller size when compared to the distribution of the remaining non-compact sources. We note that the fraction of the identified compact sources is well above the number expected at 1.5σ for a normal distribution (i.e. 6.7%). The compact sources follow a similar distribution as other extended sources in physical properties, such as stellar mass, star formation rate (see also Fig. 2), β_{UV} , except for star formation surface density (Sec. 5.1). The ISM properties of the compact sources are further investigated in Sec. 5.2.

5. DISCUSSION

5.1. High Star Formation Efficiency Revealed by NIRCcam Imaging

Star formation (rate) surface density,

$$\Sigma_{\text{SFR}} / M_\odot \text{ yr}^{-1} \text{ kpc}^{-2} = 0.5 \text{ SFR} / \pi R_e^2, \quad (8)$$

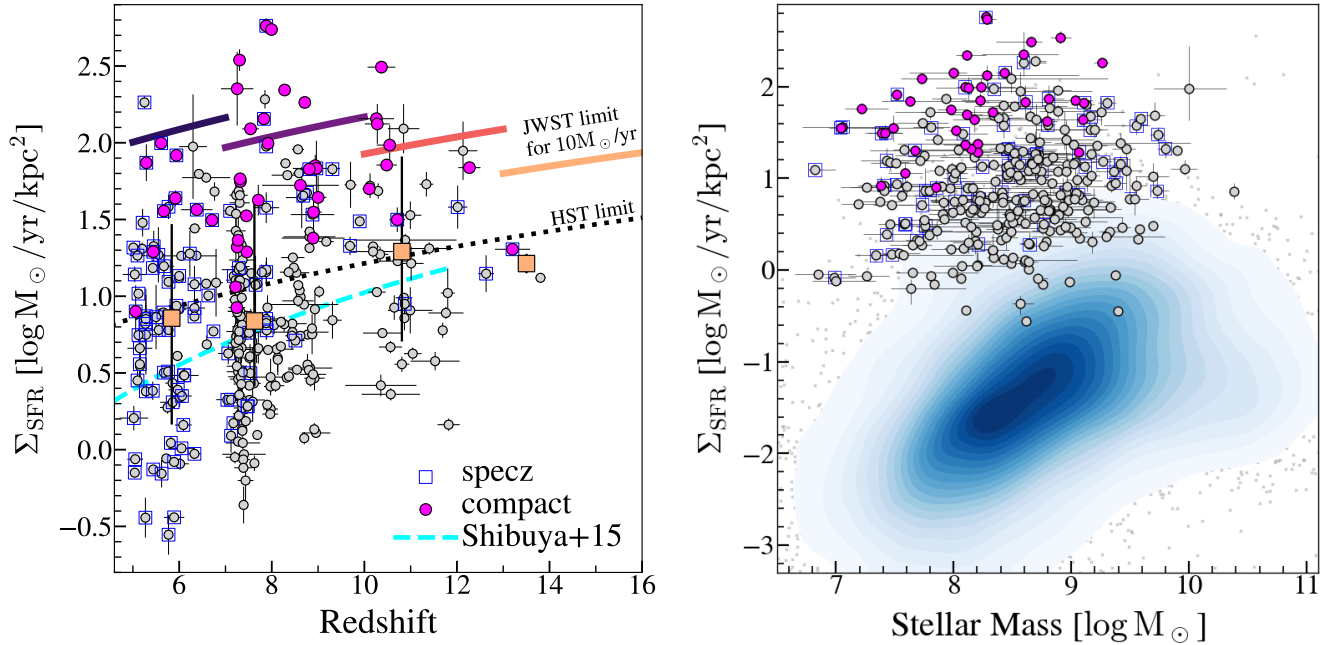


Figure 7. (*Left*): Star formation surface density (Σ_{SFR}) of our final sample (gray circles) as a function of redshift. The median values at each dropout redshift window are shown by larger symbols (squares). The upper limits for Σ_{SFR} by spatial resolution limit, when assuming SFR of $10 M_{\odot}/\text{yr}$, are shown for the corresponding JWST NIRCcam filters (solid curved lines) and the HST WFC3-IR F160W (black dotted line). The fit derived for LBGs in HST data (Shibuya et al. 2015, cyan dashed line) is shown. (*Right*): Σ_{SFR} as a function of stellar mass. In the background, we show the density contour for the distribution of galaxies at $0.3 < z < 3.5$, taken from the 3DHST catalog (Skelton et al. 2014; van der Wel et al. 2014). Those outside the lowest contour level are shown individually (crosses). Only $\sim 6\%$ of the 3DHST sample (and $< 0.01\%$ of the $z \sim 0$ Sloan sample) is found at $\Sigma_{\text{SFR}} > 1 M_{\odot}/\text{yr}/\text{kpc}^2$; the majority of our sample is located above the value.

is known as an excellent proxy for inferring the current mode of star formation. In Fig. 7, we show the distribution of Σ_{SFR} of our sample. Overall, the median values of our galaxies are consistent with previous studies with HST (Oesch et al. 2010; Shibuya et al. 2015).

However, we observe a large scatter along the vertical axis. In fact, we find a large fraction of galaxies of $\log \Sigma_{\text{SFR}} \gtrsim 1.5$, comparable to local ULIRG/starburst (Scoville et al. 2000; Dopita et al. 2002; Kennicutt & Evans 2012) and high- z sub-millimetre galaxies (e.g., Daddi et al. 2010). Such high- Σ_{SFR} galaxies were not reported in previous HST studies at similar redshift (Oesch et al. 2010; Ono et al. 2013; Holwerda et al. 2015), except for a few cases in cluster lensing fields (e.g., Kawamata et al. 2015; Bouwens et al. 2022). Obviously, Σ_{SFR} estimates are limited by imaging resolution, and thus the previous estimate for smaller galaxies identified in HST data often remained as lower limits (e.g., Morishita 2021; Fujimoto et al. 2022; Ishikawa et al. 2022).

The observations in Fig. 7 also demonstrate the potential for JWST NIRCcam observations to probe star formation activity at low stellar masses ($M \lesssim 10^8 M_{\odot}$). This had been so far limited to indirect probes, such as studies based on follow-up of Gamma Ray Burst after-

glows to quantify the fraction of detected host galaxies (e.g., Tanvir et al. 2012; Trenti et al. 2012a; McQuire et al. 2016). Those studies hinted the existence of the population of sources now directly probed by NIRCcam.

5.1.1. Implications for Star-formation Efficiency

The compact sources identified in Sec. 4.4 dominate the upper range, $\log \Sigma_{\text{SFR}} \gtrsim 1.5$. We note that this does not stem from their star formation rates, which are, on average, comparable to those of more extended sources. Instead, it is attributed to their compact nature. These compact sources' physical characteristics are particularly intriguing, as negative feedback is likely more effective within confined systems. The observed high values thus imply efficient gas fueling within these compact sources, potentially facilitated by processes such as the loss of angular momentum through mergers (see also Sec. 5.2).

In addition, the mass-dependence of Σ_{SFR} could hint at the efficiency of star formation, as the system's mass is tightly linked to the regulation of star formation. In the right panel of Fig. 7, we show the distribution of Σ_{SFR} as a function of stellar mass. Of particular interest is the high mass range, $\sim 10^9 M_{\odot}$. In this mass

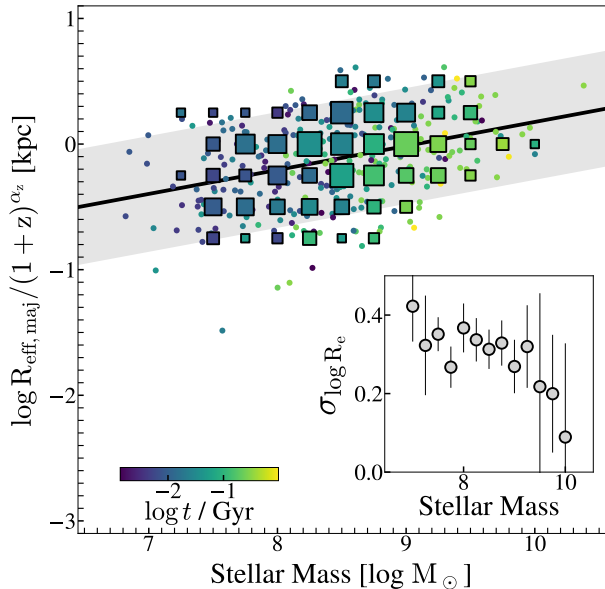


Figure 8. Same as in Fig. 5 but symbols are color-coded by age ($\log t$) derived in our SED analysis. The median age in each grid is shown by larger symbols (squares), with the symbol size scaled by the number of galaxies in the grid. In the inset, the scatters in size measured at each mass bin are shown. The error of each scatter measurement is estimated by bootstrapping. Clearly, the radius and age of the stellar population increase, while the scatter in sizes decreases, with increasing stellar mass.

range, the shocked gas remains hot (e.g., [Birnboim & Dekel 2003](#); [Dekel & Birnboim 2006](#); [Stern et al. 2021](#)), resulting in a reduced star formation efficiency, as seen at lower redshifts. The observed high values for our sample thus imply that our sources still hold a high efficiency within this mass regime. We calculate the median mass-doubling time by $t = M_*/\text{SFR}$ and find $\sim 15\text{--}90$ Myr for our sample. These considerably small mass-doubling times suggest that some galaxies in our sample could evolve to $\log M_*/M_\odot \sim 11$ by $z \sim 5$, provided that the efficiency remains similar in the following $\sim 0.5\text{--}1$ Gyr.

5.1.2. Implications for the Growth of Galaxies

At these early cosmic time, comparing the radius-mass relationship of galaxies as a function of the age of the stellar population can reveal how galaxies grow (Fig. 8). In hierarchical structure formation, galaxies grow through the merger of smaller mass galaxies. The merger process results in the infall of stars but also allows new star-formation to occur through shocking of the infalling gas. If galaxies grow predominantly by cold gas accretion (e.g. [Dekel & Birnboim 2006](#)), one would expect their size to evolve predominantly through secu-

lar evolution which would be driven by dynamical friction between the stars and the accreted gas i.e. galaxies would become smaller as they built up their stellar mass. We find two clear trends in our sample of high- z galaxies:

1. Both radius and age increase with stellar mass. High mass galaxies harbor older (\sim several 100 Myr) stellar populations compared to lower mass galaxies, which harbor populations of age $\sim 10\text{--}100$ Myr.
2. The scatter in radii at fixed mass is larger by 0.2 dex for low mass galaxies than for high mass galaxies.

Since there is no selection effect that prevents the selection of small, high mass galaxies, the implication of these two observational trends is that galaxies form inside out. Small, low-mass galaxies have a large scatter in their sizes likely due to a combination of gas accretion and merger events. As they form stars, the stars get scattered due to three-body interactions, resulting in a growth in size and stellar mass. That is consistent both with the size evolution with cosmic time and the radius and stellar age evolution with mass. Although the sensitivity of the data at the present time are not adequate to constrain minor merger rates at these redshifts, future deeper surveys will help develop this hypothesis further.

5.1.3. Comparison with Local Lyman-Break Analogs

It is illustrative to compare the luminosity surface density of these galaxies with similar objects in the local Universe ([Hoopes et al. 2007](#); [Overzier et al. 2009](#); [Shim & Chary 2013](#)). Although objects with such high surface densities of star-formation exist at $z \sim 0$, less than 0.01% of galaxies in the Sloan sample have $\Sigma_{\text{SFR}} > 1 M_\odot \text{ yr}^{-1} \text{ kpc}^{-2}$. Even at higher redshifts, the fraction remains small ($\sim 6\%$ at $0.3 < z < 3.5$; [Skelton et al. 2014](#)). In contrast, the fraction is $\sim 100\%$ in our sample. The $z \sim 0$ objects have a median mass of $10^{8.9} M_\odot$ and span the full range of metallicity from sub-solar to super-solar. They are not particularly biased towards young ages as determined from the strength of the Balmer break. Morphologically, we see some evidence of mergers in the high- z sample with $\sim 20\%$ of galaxies having nearby companions (besides the 24 galaxies flagged in the size analysis). Taken together, the implication therefore is that the high surface densities are gas-rich galaxies with the gas being relatively concentrated towards the nucleus of the galaxy indicating that the late stages of the merging process is driving the inflow of gas towards the nucleus of the galaxies.

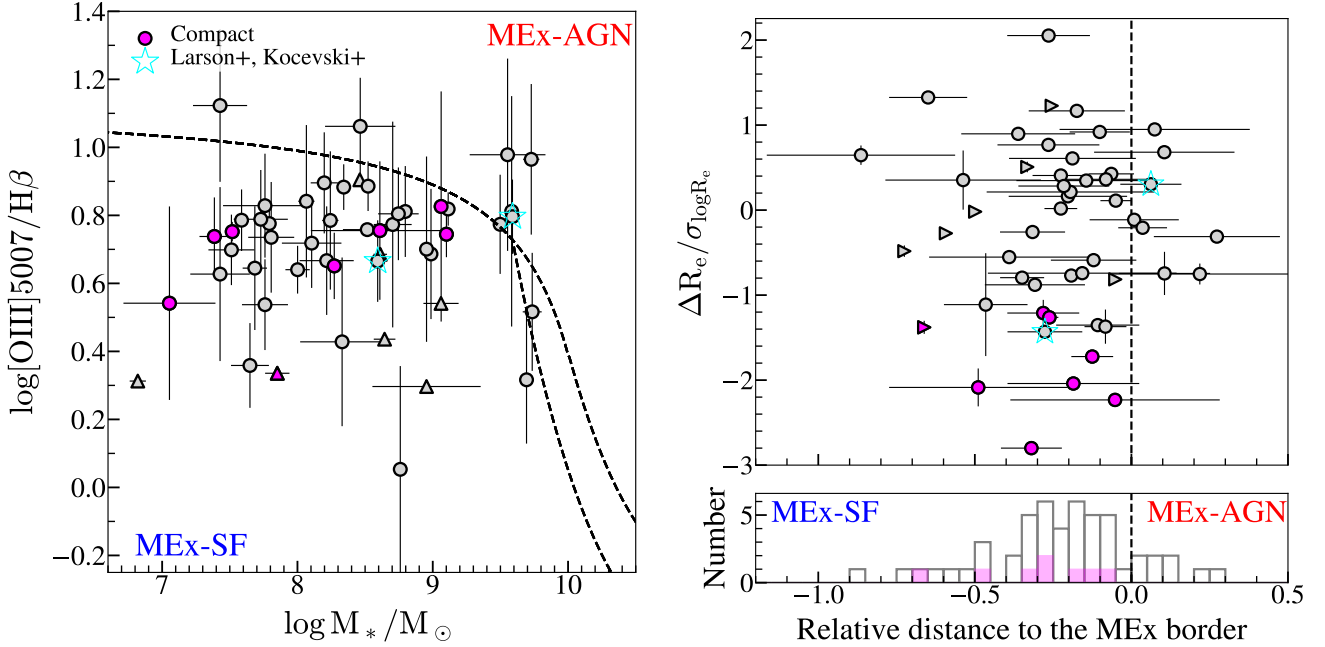


Figure 9. (Left): Distribution of 51 galaxies at $5 < z < 9.5$ that have robust $[\text{O III}]_{\lambda 5007}/\text{H}\beta$ measurements by NIRSpect MSA, in the mass-excitation (MEx) diagram (circles). For those with $\text{H}\beta$ detected at $S/N < 3$, lower limits for the ratio are shown (triangles). Compact galaxies (as defined in Sec. 4.4; magenta) and two sources from Larson et al. (2023); Kocevski et al. (2023, cyan stars) are marked separately. The solid lines are shown to indicate the regions dominated by star forming galaxies (left bottom) and AGN (right top) of $z \sim 2$ (Juneau et al. 2014). (Right): Distribution of the normalized size ($\Delta R_e/\sigma_{\log R_e}$, an indicator that is used to define compactness in Sec. 4.4) as a function of the distance to the MEx border separation line.

5.2. Nature of the Compact Sources — NIRSpect Spectroscopic Analysis

We here investigate the nature of the compact sources identified in Sec. 4.2, specifically aiming to observe if they exhibit any evidence of AGN. Traditionally, point-source-like morphologies of UV bright sources have been considered as evidence of AGN. However, it has been shown that the compactness does not always indicate the presence of AGN (e.g., Morishita et al. 2020), and vice versa (see, e.g., Matthee et al. 2023, for faint AGN with extended features). As such, a comprehensive approach is required to answer the question.

A subset of our sample galaxies have spectroscopic coverage by NIRSpect/MSA, taken as part of CEERS, GLASS-ERS, and JADES. Following Morishita et al. (2023), we reduce the MSA spectra, using `msaexp`⁴. For the extracted 1d spectrum of each source, we fit the line profiles of $\text{H}\beta$ and $[\text{O III}]$ -doublets with a Gaussian, after subtracting the underlying continuum spectrum inferred by `gsf` in Sec. 3.4. For each line, the total flux of each line is estimated by integrating the flux over the wavelength range of $2 \times \text{FWHM}$ derived from the gaussian fit. In the following analysis, we include sources with mea-

sured line S/Ns above 3 for the $[\text{O III}]_{\lambda 5007}$ line ($N=51$); when $\text{H}\beta$ is not detected above the same significance, we quote the 3σ flux limit measured at the wavelength of the line over the same line width derived for $[\text{O III}]_{\lambda 5007}$.

In Fig. 9, we show the sample in the mass-excitation (MEx) diagram, a conventional diagnostic for AGN and star-forming galaxies (Juneau et al. 2011). Among the 51 objects, we find eight sources located within the MEx AGN region defined by Juneau et al. (2014). One of the sources, CEERS7-18822, was previously reported to have a tentative ($\sim 2.5\sigma$) broad component in $\text{H}\beta$ (Larson et al. 2023), agreeing with the classification here. CEERS7-18822 exhibits extended structures in F115W, which confirms our classification of this source not to be compact.

None of our compact sources is classified as MEx-AGN. While JADESGDS-18784 is located near the MEx border, with $\log[\text{O III}]/\text{H}\beta = 0.83 \pm 0.34$ (classified as MEx-AGN within the uncertainty range), we do not confirm any features that immediately supports the presence of AGN (i.e. broad line features or high-ionization lines). None of the other compact sources show AGN signatures either, except for CEERS6-7832 which was

⁴ <https://github.com/gbrammer/msaexp>

reported to have a broad (~ 2000 km/s) component in its H α line (Kocevski et al. 2023, as CEERS.1670⁵).

However, this does not completely rule out the absence of AGN. Firstly, the discriminating power of the MEx diagram could be lower near the transition region. As shown by Juneau et al. (2014), for the range of $\log [\text{O III}]/\text{H}\beta$ line ratios probed here ($\gtrsim 0.4$) there could be 10–30% of AGN present even inside the MEx-SF region at $\log M_*/M_\odot \sim 10$. For example, the aforementioned CEERS.7832 is found in the MEx-SF region. The accuracy of the AGN classification at a lower mass range is not known due to the lack of data in the previous study. We also note that the observed ratio for our sample ($\log [\text{O III}]/\text{H}\beta \gtrsim 0.6$) is relatively high, compared to the star-forming galaxies of a comparable mass in Juneau et al. (2014, also Shapley et al. 2015). Such a high ratio can still be achieved by a stellar-only configuration, but requires, e.g., high electron density (Reddy et al. 2023).

We note that, given the evolving ISM properties at these redshifts, there is likely a shift of the MEx boundary toward a higher line ratio, as is the case for $z \sim 0$ to $z \sim 2$. As such, it is still possible that any of our MEx-SF sources near the border may host an AGN, if not a broad line AGN. Furthermore, as has been demonstrated in the local Universe (Ho et al. 1997), it is possible to bury a low-luminosity Seyfert or LINER-type nucleus in a galaxy without detecting a component of broad line emission. Vice versa, some lower-mass MEx-AGN sources here could turn to be MEx-SF due to the potential redshift evolution of the boundary.

Nonetheless, the absence of clear AGN evidence implies that the observed high ratios are driven by high surface density of star formation. When we fit high values of $[\text{O III}]/\text{H}\beta > 3$ with radiative shock models (e.g., MAPPING III; Allen et al. 2008), we find that shock velocities of a median of 500 km/s are required. Ratios of ~ 10 can only be achieved with high shock velocities which could be correlated with high surface density of star-formation (or strong AGN activity). Achieving the observed high star formation surface density ($> 100 M_\odot/\text{yr}/\text{kpc}^2$) is considered challenging, due to the presence of negative feedback. Such high density is expected only in an extreme environment, where an abundant of gas is available, and/or in (post-)merging systems where gas could rapidly fall in. By comparing with a numerical simulation, Ono et al. (2022) found that such a compact galaxy is in a temporary compact

star-forming phase triggered by recent major mergers. Roper et al. (2022a) found a large fraction of blue compact (~ 100 – 300 pc) galaxies *and* these galaxies to have little contribution by AGN in the FLARES simulations (also, Marshall et al. 2022, Shen, X., in prep.). Future work will compare derived physical parameters from the emission lines, with the measured star-formation rate density.

5.3. Comparison of sizes in rest-frame UV and optical

In this study, we have analyzed the sizes of galaxies at a rest-frame wavelength of ~ 1600 Å. In Sec. 4.2, we found that the average sizes of our galaxies are much smaller than those predicted from the extrapolation of van der Wel et al. (2014) at the corresponding redshift. A possible explanation for the discrepancy could be the rest-frame wavelengths where the size is measured in the previous study (i.e. ~ 5000 Å). We investigate this by repeating our size analysis but in a filter that corresponds to ~ 5000 Å, i.e. F356W for the F070W-dropouts, and F444W for the F090W-dropouts. For the other two ranges at higher redshift, we use the reddest filter available (F444W), which corresponds to ~ 4000 Å and ~ 3000 Å, respectively. In Fig. 10, we show the distribution of the size difference in these two wavelengths. We find that the difference of size in the two filters is negligible on average, and thus conclude that the wavelength difference cannot explain the offset seen in the extrapolated size of van der Wel et al. (2014) observed in Fig. 6. Instead, we speculate that the extrapolation of their relation may not persist in the redshift range far beyond their probed redshift range $z < 3$.

In fact, we have seen in Sec. 4.2 that the size evolution is much slower ($\alpha_z = -0.4$) than the one found in previous studies of rest-frame UV size (~ -1.2 ; Mosleh et al. 2012; Shibuya et al. 2015). While a comprehensive analysis covering a wide redshift range would be necessary, we attribute the observed conflict to the build-up of complicated structures in galaxies, such as a central massive bulge and young star forming disk. At lower redshifts, we observe a more pronounced difference in sizes between different wavelengths, driven by radial color gradients within the systems (e.g., Vulcani et al. 2014). Similarly, Shibuya et al. (2015) found that at $z = 1.2$ – 2.1 the average UV size is smaller than the optical size by $\sim 20\%$ in the low-mass regime ($\sim 10^9 M_\odot$), while the trend is reversed at the high-mass end ($\gtrsim 10^{11} M_\odot$; also see Szomoru et al. 2012; van der Wel et al. 2014).

On the other hand, the resemblance of galaxy UV and optical sizes of high-redshift galaxies is not unexpected given the rapid assembly of the stellar content (also see

⁵ The other object reported by Kocevski et al. (2023), CEERS.3210, does not pass our $S/N > 8$ selection criterion and is not included in our final sample.

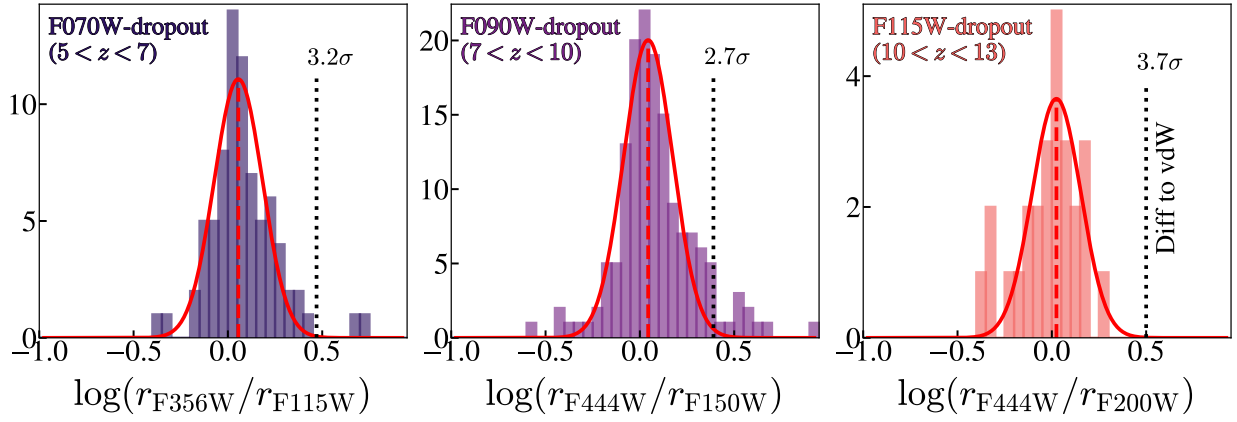


Figure 10. Distributions of rest-frame UV-to-optical size ratio for three redshift bins. The first two panels compares rest-frame UV to optical ($\sim 5000 \text{ \AA}$) sizes, whereas the last panel at a shorter wavelength ($\sim 3700 \text{ \AA}$) due to the filter availability. Only resolved galaxies in the two filters are included. The F150W-dropouts are not shown, as neither of their size is resolved in F444W. Each distribution is fit with Gaussian (red lines), with the mean position indicated by vertical dashed lines. The difference to the extrapolated size in rest-frame optical of *van der Wel et al. (2014)* (observed in Fig. 6) is shown in each panel (dotted vertical lines); the difference is measured to be 3.2 , 2.7 , and 3.7σ , respectively.

Yang et al. 2022b; Treu et al. 2023). For our galaxies, we have estimated the mass-doubling time to be $\lesssim 100 \text{ Myr}$ in Sec. 5.1. This time scale is comparable to or even smaller than the star formation time scale that the UV tracer is sensitive to (Murphy et al. 2011; Flores Velázquez et al. 2021). Consequently, the stellar content detected by the UV will predominate over the total content integrated over the full star formation history, which is probed by observations at optical wavelengths. The majority of our galaxies are actively building their structures inside-out, developing rapidly enough to maintain coherence.

Lastly, we investigate the rest-frame optical size of the compact sources identified in this work. Of 44, we find 13 ($\sim 29\%$) show resolved morphology in optical filters. This is opposite from the general trend discovered above, and implies that some fraction of these compact sources are likely experiencing a secondary burst, in a relatively small area, after the initial build-up of stellar structure. This is in particular relevant to the stochastic nature of star formation in early galaxies, which may have non-negligible effect of the observed UV magnitude measurements and consequently UV luminosity functions.

6. SUMMARY

In this study, we have identified 341 galaxies at $5 < z < 14$ in legacy fields of JWST and analysed their rest-frame UV and optical sizes through JWST NIRCam images. The imaging data used here were collected from several public programs in Cycle 1, resulting in a combined effective area of 358 arcmin^2 . With a robust (8σ) selection of 341 galaxies, made possible by the unprecedented area coverage provided by JWST, we have con-

ducted the first systematic exploration of the size-mass relation of galaxies in the first billion years. The key findings are as follows:

- The slope of the size-mass relation was derived via linear regression analyses and found to be $\alpha \sim 0.2$, similar to those of star forming galaxies at $z < 3$ but scaled down in size by 0.4 dex. The derived intercept was found to evolve with $\propto (1+z)^{-0.4}$, much slower evolution than those found in previous studies of rest-frame UV sizes of galaxies at lower redshifts.
- By using the results from our linear regression analysis, we identified 44 compact sources that are marginally resolved in NIRCam imaging. These compact sources account for $\sim 13\%$ of the full sample presented here.
- We found that our sources overall have high star formation surface density ($\gtrsim 1 M_{\odot} \text{ yr}^{-1} \text{ kpc}^{-2}$), with the newly identified compact sources being as high as $\sim 300 M_{\odot} \text{ yr}^{-1} \text{ kpc}^{-2}$. We demonstrated that the absence of a clear declining trend indicates that star formation efficiency may remain high even at the high mass range; if the observed high efficiency remains similar in the following $\sim 0.5\text{--}1 \text{ Gyr}$, some of our sources would evolve to $\sim 10^{11} M_{\odot}$ by $z \sim 5$.
- For 51 sources with available NIRSpec/MSA data, we investigated their ISM via the $[\text{O III}]\text{-to-}\text{H}\beta$ line ratio. None of the compact sources are confidently classified as AGN in the Mass-Excitation diagram;

however, the nature of the compact sources remains to be conclusively elucidated in a future study. A potential explanation for the observed high line ratios is high shock velocities, driven by intense star-formation characterized by high Σ_{SFR} .

- We found that the sizes in rest-frame and optical wavelengths are on average consistent. We attributed this to the short mass-doubling time (i.e. $1/\text{sSFR} < 100 \text{ Myr}$) of our sources, implying that they are actively building their structure coherently, and are thus dominated by young stars.

With the unprecedented resolution and sensitivity provided by JWST, this work demonstrated a comprehensive size analysis of galaxies in the first billion years. Of particular remarks are the newly discovered compact population. Specifically, the physical mechanisms that maintain the observed high star formation rate in such compact systems, which are likely under the strong influence by negative feedback, remains an open question. Recent JWST observations have identified a number of faint AGN (Onoue et al. 2023; Matthee et al. 2023) and a complex of dusty AGN + young stellar populations (Furtak et al. 2023; Labbe et al. 2023; Akins et al. 2023), suggesting a greater prevalence of AGN in high- z galaxies than previously thought. These emerging findings raise a caveat that the estimated *star formation* rate from our SED analysis may not accurately represent the intrinsic value, even though our spectroscopic analysis on the subsample did not find any immediate signatures of AGN. Future spectroscopic followups of the compact sources will provide further insight into their nature and their potential impact in a broad cosmological context.

ACKNOWLEDGEMENTS

We would like to thank the teams of the JWST observation programs #1063, 1180, 1210, 1345, 1837, 2079, and 2738, which a large part of this study is based on, for their countless efforts in carefully designing and planning their programs and their generous consideration of making their valuable data publicly available immediately after the observations or before the expiration of the original proprietary periods. Some/all of the data presented in this paper were obtained from the Mikulski Archive for Space Telescopes (MAST) at the Space Telescope Science Institute. The specific observations analyzed can be accessed via [10.17909/q8cd-2q22](https://doi.org/10.17909/q8cd-2q22). We thank Zhaoran Liu for kindly providing a spectroscopic catalog compiled from literature studies in the CEERS field. We acknowledge support for this work under NASA grant 80NSSC22K1294. The data presented

in this paper were obtained from the Mikulski Archive for Space Telescopes (MAST) at the Space Telescope Science Institute.

Software: Astropy (Astropy Collaboration et al. 2013, 2018, 2022), bbp (Morishita 2023), EAzY (Brammer et al. 2008), EMCEE (Foreman-Mackey et al. 2013), gsf (Morishita et al. 2019), numpy (Harris et al. 2020), python-fsps (Foreman-Mackey et al. 2014).

APPENDIX A: COMPARISON WITH THE M_{UV} -SIZE RELATION

In Fig. 11, we show the distribution of our sample galaxies in the absolute UV magnitude (M_{UV})-size plane. We follow the regression analysis in Sec. 4.2 using the following formulae:

$$\log R_e(M_{\text{UV}}, z) = \alpha(M_{\text{UV}} - M_{\text{UV},0}) + B(z), \quad (9)$$

$$B(z) = \beta_z + \alpha_z \log(1 + z). \quad (10)$$

We adopt the pivot magnitude $M_{\text{UV},0} = -20 \text{ mag}$. The regression analysis gives a similar slope ($\alpha = -0.09 \pm 0.02$) to those found in the literature at $z \sim 5$ (-0.1 ; Huang et al. 2013) and at similar redshift (-0.11 – -0.15 ; Shibuya et al. 2015; Kawamata et al. 2018). The intercept is very similar to Yang et al. (2022b), who derived the intercept for $7 < z < 12$ galaxies using a fixed slope of the Huang et al. (2013)’s value. The consistent intercept supports that our size measurement is comparable to the literature studies (see also Ono et al. 2022, who compare their sizes with Yang et al. 2022b). The derived parameters are reported in Table 4.

In Fig. 12, we show the distribution of our final sample in the $M_{\text{UV}}\text{-log } M_*$ plane. The distribution shows a weak trend with β_{UV} but not with redshift. We thus characterize the distribution by:

$$\log M_*(M_{\text{UV}}, \beta_{\text{UV}}) = \alpha(M_{\text{UV}} - M_{\text{UV},0}) + B(\beta_{\text{UV}}), \quad (11)$$

$$B(\beta_{\text{UV}}) = \beta_c + \alpha_c(\beta_{\text{UV}} - \beta_{\text{UV},0}) \quad (12)$$

with the same pivot magnitude $M_{\text{UV},0} = -20 \text{ mag}$ as above, and $\beta_{\text{UV},0} = -2$. The regression slope is determined but with a relatively large scatter ($\sigma \sim 0.47$) By using this conversion and the size-stellar mass relation in the main text, we can predict the size- M_{UV} relation (and vice versa). In Fig. 11, along with the regression derived above, we show the predicted size- M_{UV} relation for the sample, by using the median β_{UV} value, in each redshift window. The predicted slope is shallower but overall in agreement with the one derived above within the uncertainty. We provide the determined parameters in Table 4.

Table 4. Linear Regression Best-Fit Coefficients

M_{UV} -Size relation					M_{UV} -Stellar mass relation				
N	α	β_z	α_z	$\sigma_{\log R_e}$	N	α	β_c	α_c	$\sigma_{\log M_*}$
317	$-0.09^{+0.02}_{-0.02}$	$0.08^{+0.21}_{-0.21}$	$-0.60^{+0.23}_{-0.22}$	$0.31^{+0.01}_{-0.01}$	317	$-0.28^{+0.03}_{-0.03}$	$8.83^{+0.04}_{-0.04}$	$0.76^{+0.08}_{-0.08}$	$0.47^{+0.02}_{-0.02}$

NOTE— Coefficients determined in the linear regression analysis in Appendix A.

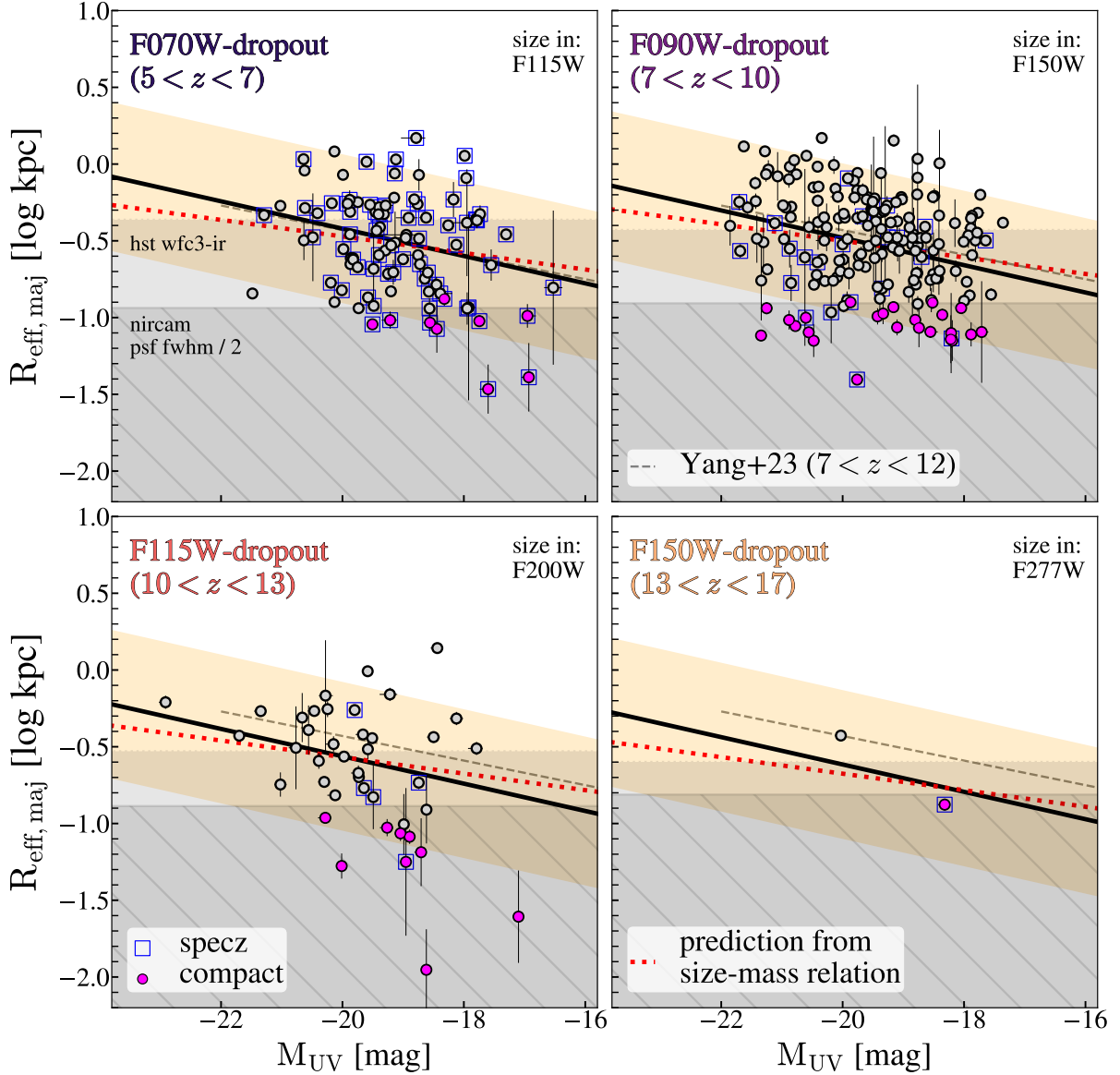


Figure 11. Same as Fig. 4 but the distribution in the absolute UV magnitude (M_{UV})-size plane. For comparison, the slope fit to LBGs at $7 < z < 12$ (Yang et al. 2022b, black dashed lines) is shown. The predicted slope from our size-stellar mass relation (Eq. 6) by using the M_{UV} -stellar mass conversion (Eq. 11) is shown (red dashed lines).

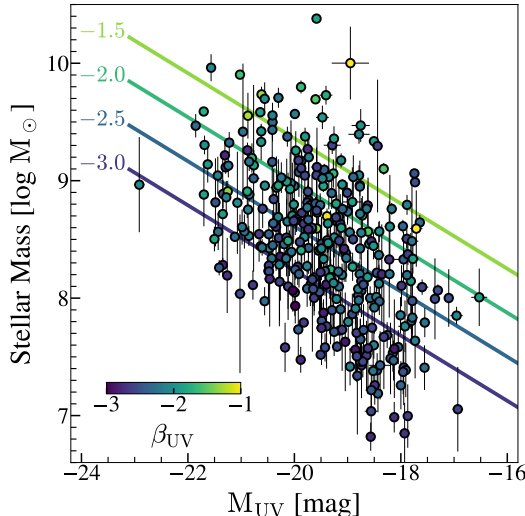


Figure 12. Distribution of our sample in the absolute UV magnitude–stellar mass plane (circles). Symbols are color-coded by the value of β_{UV} . The regression slopes at various β_{UV} values, determined using Eqs. 11 and 12, are shown (solid lines).

APPENDIX B: PHYSICAL PROPERTIES OF THE FINAL SAMPLE

We report the physical properties of the final 341 sources at $z > 5$ in Table 5. The table contains coordinates, apparent magnitudes (Sec. 3.1), spectroscopic or photometric redshifts (Sec. 3.2.2), size measurements and flags (Sec. 3.3 and 4.4), and SED parameters (Sec. 3.4).

APPENDIX C: ON THE SAMPLE COMPLETENESS AND THE ROBUSTNESS OF OUR SIZE MEASUREMENTS

We investigate the selection completeness of sources with various input sizes and SNRs. We follow a similar procedure presented in Morishita et al. (2018) and make mock images by burying artificial sources (of Sérsic index set to 1) in random, relatively source-free positions in the processed mosaic images. We then repeat our detection and selection analyses as presented in Sec. 3 and check their completeness at each SNR and input radius.

As shown in Fig. 13, the selection completeness is $> 50\%$ above our SN cut ($\text{SNR}_{UV} = 8$) for those with small sizes (5.4 pixel and smaller). The completeness decreases to as low as $\sim 20\%$ at a larger size. The observed trend is expected, as the source flux is more likely affected by neighbouring sources and affected by background local subtraction and thus cannot be reproduced very accurately. It is also noted that lowering the limiting SNR would not only decrease the completeness

but also introduce a larger fraction of low- z interlopers, as reported in Morishita & Stiavelli (2023).

In the middle and bottom panels of Fig. 13, we show the recovered magnitude and size for the same mock galaxies by our size measurement analysis in the F150W band. Above our limiting SNR, magnitudes are overall recovered well, within 10% accuracy. The input size is also recovered well, down to ~ 0.9 pixel, which corresponds to about half of the FWHM size in F150W. This validates our selection criterion used for unresolved sources (Sec. 4.4). The exception is those with a very large size (10.8 pixel, or ~ 1.8 kpc at $z = 7$), where the output size turns to be 30% smaller than the input value on average. The trend seen here is overall consistent with the one reported by Ono et al. (2023).

While our sample construction has been conducted with an extreme care by maintaining high source completeness, accurate size measurement, and high source purity, the test above implies that our selection may not be as complete at large size, $\gtrsim 2$ kpc. Improving the completeness in the regime is not impossible but challenging, as detection completeness becomes flattened at a certain SNR and does not linearly improve for large-sized sources. However, we note that 2 kpc characterizes $\sim 3\sigma$ above the median size at $\log M_*/M_\odot \sim 8.5$, the median stellar mass of our sample galaxies. The distribution of the measured size of our galaxies does not show any evidence of a skewed feature at large radius. As such, if there are any large-sized sources missing in our sample, we speculate that those are still small in number and hardly affect the results of our regression analysis.

APPENDIX D: IMAGE CUTOUTS OF COMPACT SOURCES

Cutout images of the compact sources identified in Sec. 4.4 are shown in Fig. 14. The only F150W-dropout that is classified as compact is shown in the main text (Fig. 3). We note that completeness for compact sources varies field to field, due to the differences in depth. Indeed, we observe that compact sources are more prevalent in two of the fields, JADESGDS and A2744. This can be explained by depth and magnification, which enhance the identification of low-mass and small-sized sources. We also note that while NGDEEP has a comparable depth as in JADESGDS, it has a relatively small area (single NIRCcam pointing). In addition, the NGDEEP field does not allow photometric selections at $z < 9.7$, the redshift range where the majority of the compact sources are identified.

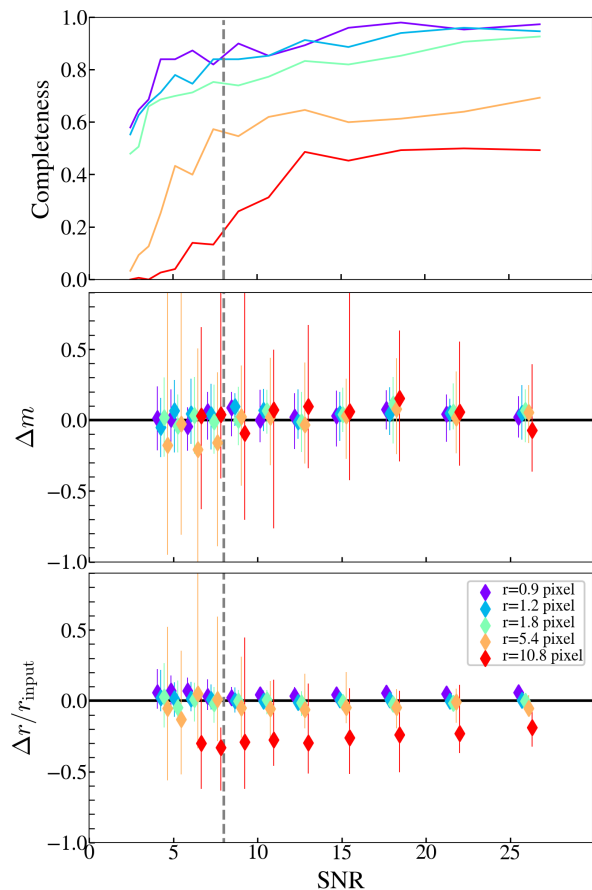


Figure 13. (Top): Source completeness as a function of rest-UV SNR, obtained for mock sources of different sizes (solid colored lines). Our conservative SNR cut ($= 8$; vertical dashed line) secures high completeness, $> 50\%$, except for large-sized sources. (Middle): Comparison of magnitudes, $\Delta m = m_{\text{output}} - m_{\text{input}}$, for sources of different sizes, measured in F150W. Median values (diamonds) and the 16th and 84th percentiles (error bars) are shown. (Bottom): Same as the middle panel but for normalized sizes, $\Delta r / r_{\text{input}}$.

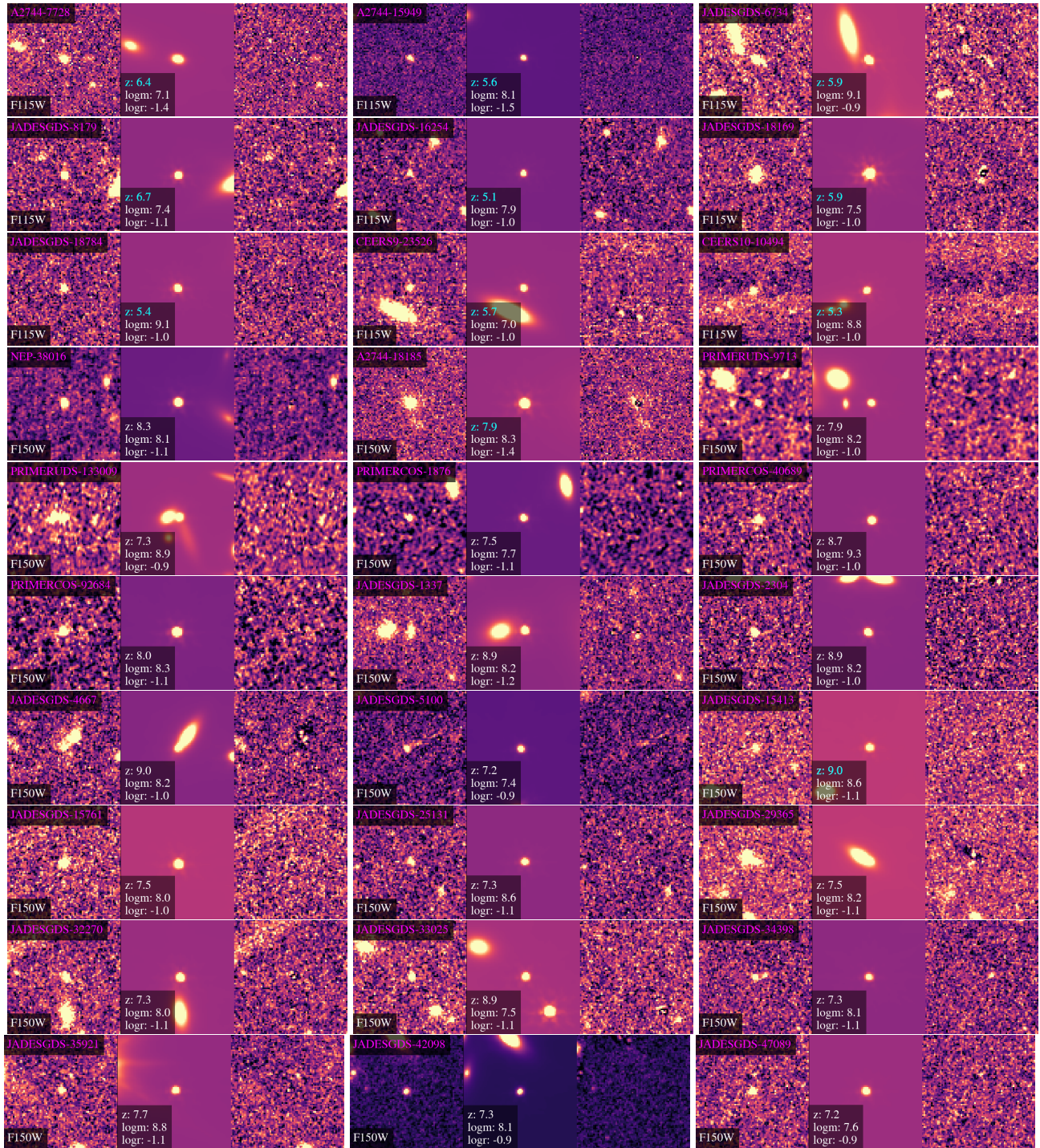


Figure 14. Sources that are classified as compact. (*left*): original image, in the UV band where the size is measured. (*middle*): *galfit* single Sérsic model image (with Sérsic index fixed to 1). (*right*): residual image. Those with spectroscopic redshift measurements are color-coded its redshift label in cyan.

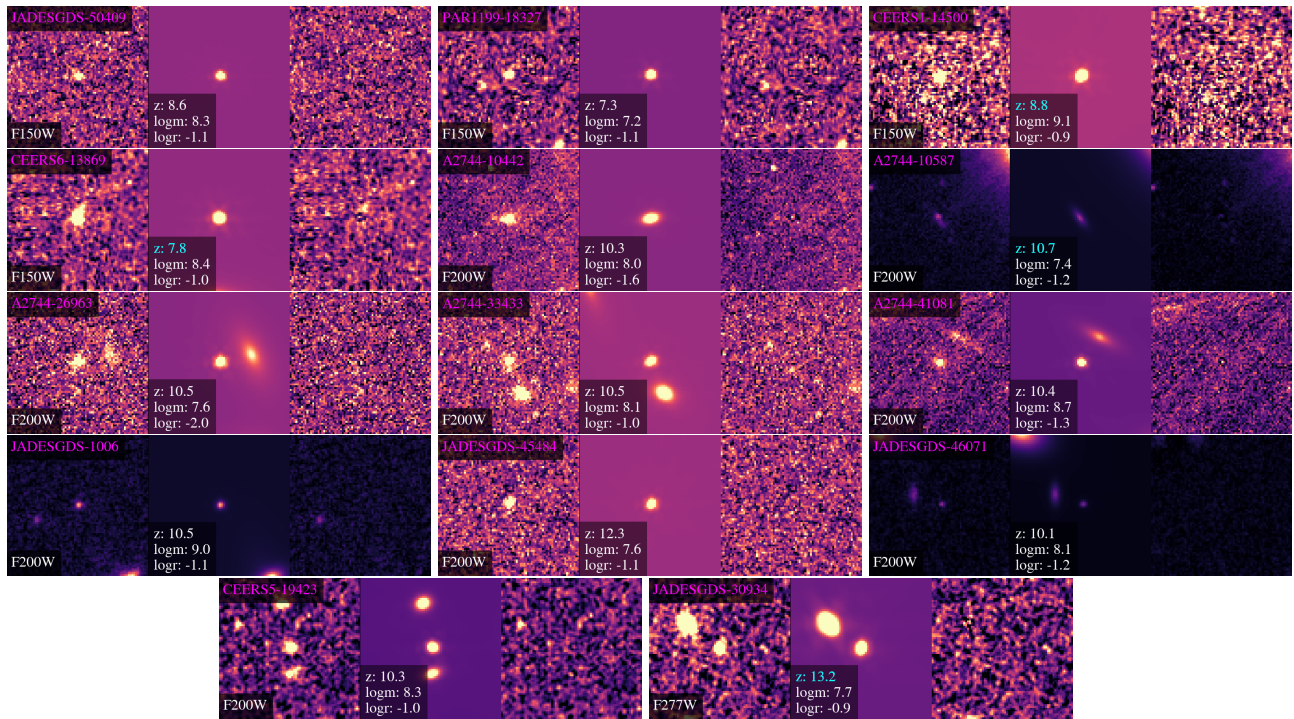


Figure 15. Continued.

Table 5. Physical properties of the final candidates.

ID	R.A.	Decl.	m_{UV}	z^\dagger	M_{UV}	M_*	SFR	β_{UV}	$R_{e,maj}$	[O III]/H β	f_{gal}^*	f_{com}^*
	deg.	deg.	mag		mag	$\log M_\odot$	$\log M_\odot/\text{yr}$		log kpc	log		
F070W-dropout												
J1235-2632	188.92749	4.8717985	26.7	$6.0^{+0.1}_{-0.2}$	$-19.9^{+0.1}_{-0.1}$	$8.7^{+0.8}_{-0.8}$	$0.8^{+0.1}_{-0.1}$	$-2.7^{+0.1}_{-0.1}$	$-0.61^{+0.01}_{-0.01}$	–	0	0
J1235-2875	188.94112	4.868082	27.0	$6.4^{+0.1}_{-0.2}$	$-19.9^{+0.1}_{-0.1}$	$9.2^{+0.1}_{-0.1}$	$0.8^{+0.1}_{-0.1}$	$-2.4^{+0.2}_{-0.1}$	$-0.65^{+0.01}_{-0.01}$	–	0	0
J1235-3021	188.93146	4.8745794	27.3	$6.0^{+0.2}_{-0.2}$	$-19.3^{+0.1}_{-0.1}$	$7.9^{+0.1}_{-0.1}$	$0.6^{+0.1}_{-0.1}$	$-2.5^{+0.1}_{-0.1}$	$-0.56^{+0.02}_{-0.02}$	–	0	0
J1235-3236	188.95332	4.8656316	27.2	$6.8^{+0.2}_{-0.2}$	$-20.1^{+0.1}_{-0.1}$	$8.7^{+0.1}_{-0.1}$	$0.7^{+0.1}_{-0.1}$	$-2.2^{+0.1}_{-0.1}$	$-0.90^{+0.02}_{-0.02}$	–	0	0
J1235-4628	188.96568	4.8757343	25.7	$5.2^{+0.1}_{-0.1}$	$-21.0^{+0.1}_{-0.1}$	$9.9^{+0.1}_{-0.1}$	$1.6^{+0.1}_{-0.1}$	$-1.6^{+0.1}_{-0.1}$	$-0.27^{+0.02}_{-0.02}$	–	0	0
J1235-4644	188.9286	4.8941765	27.0	$6.3^{+0.2}_{-0.2}$	$-18.9^{+0.3}_{-0.4}$	$10.0^{+0.3}_{-0.3}$	$1.9^{+0.3}_{-0.3}$	$-0.6^{+0.5}_{-0.2}$	$-0.46^{+0.03}_{-0.03}$	–	0	0
J1235-5704	188.94789	4.8993416	26.7	$6.6^{+0.1}_{-0.1}$	$-21.5^{+0.1}_{-0.1}$	$8.8^{+0.5}_{-0.5}$	$0.9^{+0.1}_{-0.1}$	$-2.5^{+0.2}_{-0.2}$	$-0.84^{+0.01}_{-0.01}$	–	0	0
J1235-7600	188.94092	4.915246	26.5	$5.7^{+0.2}_{-0.2}$	$-20.1^{+0.1}_{-0.1}$	$9.4^{+0.1}_{-0.1}$	$0.9^{+0.1}_{-0.1}$	$-2.4^{+0.1}_{-0.1}$	$0.08^{+0.02}_{-0.02}$	–	0	0
J1235-8122	188.96327	4.9074202	27.6	$5.2^{+0.1}_{-0.1}$	$-19.0^{+0.1}_{-0.1}$	$8.6^{+0.1}_{-0.1}$	$0.4^{+0.1}_{-0.1}$	$-2.2^{+0.3}_{-0.1}$	$-0.48^{+0.04}_{-0.04}$	–	0	0
J1235-9040	188.95932	4.9153123	26.4	$6.0^{+0.1}_{-0.1}$	$-20.6^{+0.1}_{-0.1}$	$8.4^{+0.1}_{-0.1}$	$0.9^{+0.1}_{-0.1}$	$-2.3^{+0.1}_{-0.1}$	$-0.50^{+0.13}_{-0.13}$	–	0	0
J1235-9171	188.95187	4.9199114	26.4	$6.0^{+0.1}_{-0.1}$	$-20.0^{+0.1}_{-0.1}$	$9.6^{+0.1}_{-0.1}$	$1.0^{+0.1}_{-0.1}$	$-2.2^{+0.1}_{-0.1}$	$-0.07^{+0.01}_{-0.01}$	–	0	0
J1235-10716	188.9635	4.9250326	27.7	$6.0^{+0.1}_{-0.2}$	$-19.1^{+0.1}_{-0.1}$	$7.9^{+0.1}_{-0.1}$	$0.4^{+0.1}_{-0.1}$	$-2.3^{+0.1}_{-0.1}$	$-0.51^{+0.20}_{-0.20}$	–	0	0
J1235-14339	188.97955	4.9459105	27.3	$6.0^{+0.3}_{-0.2}$	$-18.7^{+0.1}_{-0.1}$	$8.1^{+0.2}_{-0.2}$	$0.6^{+0.1}_{-0.1}$	$-2.4^{+0.1}_{-0.1}$	$-0.07^{+0.10}_{-0.10}$	–	0	0
J1235-15130	188.97173	4.9549723	27.3	$6.3^{+0.1}_{-0.1}$	$-19.2^{+0.1}_{-0.1}$	$8.7^{+0.1}_{-0.1}$	$0.6^{+0.1}_{-0.1}$	$-2.7^{+0.1}_{-0.1}$	$-0.83^{+0.02}_{-0.02}$	–	0	0
J1235-15534	188.97287	4.9570713	26.9	$5.9^{+0.1}_{-0.2}$	$-19.7^{+0.1}_{-0.1}$	$8.9^{+0.2}_{-0.2}$	$0.7^{+0.1}_{-0.1}$	$-2.5^{+0.1}_{-0.1}$	$-0.25^{+0.02}_{-0.02}$	–	0	0
J1235-16374	189.00362	4.9468131	27.0	$5.8^{+0.2}_{-0.2}$	$-19.1^{+0.1}_{-0.1}$	$7.7^{+0.2}_{-0.2}$	$0.6^{+0.1}_{-0.1}$	$-2.6^{+0.1}_{-0.1}$	$-0.22^{+0.02}_{-0.02}$	–	0	0
J1235-17410	189.00334	4.9532456	26.0	$6.6^{+0.1}_{-0.1}$	$-20.6^{+0.1}_{-0.1}$	$9.3^{+0.1}_{-0.1}$	$1.4^{+0.1}_{-0.1}$	$-1.9^{+0.1}_{-0.1}$	$-0.04^{+0.02}_{-0.02}$	–	0	0
J1235-17888	188.97598	4.9694805	27.2	$6.6^{+0.1}_{-0.1}$	$-19.8^{+0.1}_{-0.1}$	$8.6^{+0.3}_{-0.3}$	$0.7^{+0.1}_{-0.1}$	$-2.7^{+0.2}_{-0.1}$	$-0.61^{+0.03}_{-0.03}$	–	0	0
J1235-18627	188.97969	4.9720902	27.0	$6.4^{+0.1}_{-0.1}$	$-19.7^{+0.1}_{-0.1}$	$8.4^{+0.1}_{-0.1}$	$0.7^{+0.1}_{-0.1}$	$-2.4^{+0.1}_{-0.1}$	$-0.94^{+0.03}_{-0.03}$	–	0	0
J1235-20019	188.99167	4.9734235	27.4	$6.8^{+0.1}_{-0.2}$	$-18.8^{+0.1}_{-0.2}$	$9.5^{+0.1}_{-0.1}$	$0.7^{+0.2}_{-0.2}$	$-1.9^{+0.2}_{-0.2}$	$-0.59^{+0.02}_{-0.02}$	–	0	0
A2744-5240	3.6025238	-30.419222	27.6	6.23	$-19.2^{+0.1}_{-0.1}$	$8.5^{+0.2}_{-0.2}$	$0.6^{+0.1}_{-0.1}$	$-2.0^{+0.1}_{-0.1}$	$-0.71^{+0.05}_{-0.05}$	0.8 ± 0.1	0	0
A2744-6031	3.5769939	-30.415525	27.1	5.13	$-18.8^{+0.1}_{-0.1}$	$8.7^{+0.1}_{-0.1}$	$0.5^{+0.1}_{-0.1}$	$-1.9^{+0.1}_{-0.1}$	$0.05^{+0.06}_{-0.06}$	–	1	–
A2744-6323	3.5706301	-30.414635	26.7	5.76	$-19.8^{+0.1}_{-0.1}$	$8.9^{+0.2}_{-0.2}$	$1.0^{+0.1}_{-0.1}$	$-1.8^{+0.1}_{-0.1}$	$-0.05^{+0.27}_{-0.27}$	–	1	–
A2744-7284	3.5879247	-30.411587	29.4	5.28	$-17.9^{+0.1}_{-0.1}$	$7.8^{+0.2}_{-0.2}$	$-0.2^{+0.2}_{-0.2}$	$-2.0^{+0.3}_{-0.2}$	$-0.93^{+0.60}_{-0.60}$	0.5 ± 0.1	0	0
A2744-7728	3.6006	-30.410273	29.9	6.38	$-16.9^{+0.1}_{-0.1}$	$7.1^{+0.3}_{-0.3}$	$-0.4^{+0.1}_{-0.1}$	$-2.6^{+0.2}_{-0.2}$	$-1.39^{+0.22}_{-0.22}$	0.5 ± 0.3	0	1
A2744-7965	3.5965643	-30.40897	29.2	5.28	$-16.5^{+0.1}_{-0.1}$	$8.0^{+0.2}_{-0.2}$	$-0.1^{+0.3}_{-0.3}$	$-1.9^{+0.2}_{-0.3}$	$-0.81^{+0.50}_{-0.50}$	–	0	0
A2744-9029	3.550838	-30.405872	27.1	5.04	$-19.5^{+0.1}_{-0.1}$	$8.5^{+0.3}_{-0.3}$	$0.6^{+0.1}_{-0.1}$	$-2.6^{+0.3}_{-0.2}$	$-0.68^{+0.25}_{-0.25}$	1.1 ± 0.1	0	0
A2744-9421	3.6000569	-30.404362	28.8	5.28	$-17.6^{+0.1}_{-0.1}$	$7.8^{+0.1}_{-0.1}$	$-0.1^{+0.1}_{-0.1}$	$-2.2^{+0.1}_{-0.1}$	$-0.66^{+0.10}_{-0.10}$	–	0	0
A2744-9436	3.5761104	-30.404465	27.4	5.66	$-19.4^{+0.1}_{-0.1}$	$8.1^{+0.2}_{-0.2}$	$0.5^{+0.1}_{-0.1}$	$-2.8^{+0.1}_{-0.1}$	$-0.59^{+0.05}_{-0.05}$	–	0	0
A2744-9642	3.6010537	-30.403976	29.2	6.33	$-17.9^{+0.1}_{-0.1}$	$7.4^{+0.2}_{-0.2}$	$-0.2^{+0.1}_{-0.1}$	$-2.6^{+0.2}_{-0.2}$	$-0.94^{+0.10}_{-0.10}$	–	0	0
A2744-9694	3.5700579	-30.403687	27.8	5.55	$-18.7^{+0.1}_{-0.1}$	$8.7^{+0.1}_{-0.1}$	$0.8^{+0.2}_{-0.2}$	$-1.6^{+0.2}_{-0.2}$	$-0.65^{+0.05}_{-0.05}$	0.8 ± 0.3	0	0
A2744-9701	3.5529106	-30.403868	27.9	5.02	$-17.9^{+0.2}_{-0.2}$	$8.3^{+0.3}_{-0.3}$	$0.2^{+0.1}_{-0.1}$	$-2.4^{+0.4}_{-0.4}$	$-0.38^{+0.35}_{-0.35}$	0.4 ± 0.2	0	0
A2744-11854	3.6054316	-30.396582	28.7	5.77	$-18.6^{+0.1}_{-0.1}$	$6.8^{+0.1}_{-0.1}$	$0.0^{+0.1}_{-0.1}$	$-2.8^{+0.1}_{-0.1}$	$-0.94^{+0.07}_{-0.07}$	> 0.8	0	0
A2744-11960	3.5907068	-30.395544	27.3	5.66	$-19.9^{+0.1}_{-0.1}$	$8.4^{+0.1}_{-0.1}$	$0.7^{+0.1}_{-0.1}$	$-2.8^{+0.1}_{-0.1}$	$-1.07^{+0.09}_{-0.09}$	–	1	–
A2744-12496	3.5651999	-30.394262	27.4	5.77	$-20.0^{+0.1}_{-0.1}$	$8.8^{+0.1}_{-0.1}$	$0.7^{+0.1}_{-0.1}$	$-1.9^{+0.1}_{-0.1}$	$-0.82^{+0.04}_{-0.04}$	0.8 ± 0.1	0	0
A2744-14994	3.5957074	-30.386774	27.7	5.05	$-18.4^{+0.1}_{-0.1}$	$8.5^{+0.1}_{-0.1}$	$0.1^{+0.1}_{-0.1}$	$-2.5^{+0.2}_{-0.1}$	$-0.46^{+0.43}_{-0.43}$	–	1	–
A2744-15060	3.5954387	-30.386791	26.9	5.05	$-19.6^{+0.1}_{-0.1}$	$8.9^{+0.1}_{-0.1}$	$0.8^{+0.1}_{-0.1}$	$-1.9^{+0.1}_{-0.1}$	$-0.29^{+0.03}_{-0.03}$	–	1	–
A2744-15949	3.5947585	-30.384432	29.1	5.61	$-17.6^{+0.1}_{-0.1}$	$8.1^{+0.1}_{-0.1}$	$-0.1^{+0.1}_{-0.1}$	$-2.6^{+0.3}_{-0.1}$	$-1.47^{+0.16}_{-0.16}$	–	0	1
A2744-37546	3.4833336	-30.332148	25.8	5.07	$-20.9^{+0.1}_{-0.1}$	$9.3^{+0.1}_{-0.1}$	$1.3^{+0.1}_{-0.1}$	$-2.0^{+0.1}_{-0.1}$	$-0.06^{+0.01}_{-0.01}$	–	1	–
PRIMERCOS-9711	150.14299	2.2567828	25.2	5.12	$-21.3^{+0.1}_{-0.1}$	$9.3^{+0.4}_{-0.4}$	$1.5^{+0.1}_{-0.1}$	$-1.9^{+0.1}_{-0.1}$	$0.10^{+0.01}_{-0.01}$	–	1	–

Table 5 continued

Table 5 (continued)

ID	R.A.	Decl.	m_{UV}	z^\dagger	M_{UV}	M_*	SFR	β_{UV}	$R_{e,maj}$	[O III]/H β	f_{gal}^*	f_{com}^*
	deg.	deg.	mag		mag	$\log M_\odot$	$\log M_\odot/\text{yr}$		log kpc	log		
PRIMERCOS-10934	150.13754	2.2596548	26.5	5.67	-20.2 ^{+0.1} _{-0.1}	7.6 ^{+0.1} _{-0.1}	0.8 ^{+0.1} _{-0.1}	-2.7 ^{+0.1} _{-0.1}	-0.26 ^{+0.03} _{-0.03}	-	0	0
NGDEEP-31979	53.225365	-27.821129	26.0	5.16	-21.1 ^{+0.1} _{-0.1}	10.5 ^{+0.1} _{-0.1}	1.6 ^{+0.1} _{-0.1}	-1.7 ^{+0.1} _{-0.1}	0.09 ^{+0.01} _{-0.01}	-	1	-
JADESGDS-6734	53.126537	-27.81809	27.9	5.92	-18.3 ^{+0.1} _{-0.1}	9.1 ^{+0.1} _{-0.1}	0.7 ^{+0.1} _{-0.1}	-1.6 ^{+0.1} _{-0.1}	-0.88 ^{+0.05} _{-0.05}	0.7 ± 0.1	0	1
JADESGDS-7592	53.145054	-27.816431	28.2	5.77	-18.0 ^{+0.1} _{-0.1}	8.6 ^{+0.1} _{-0.1}	0.1 ^{+0.1} _{-0.1}	-2.3 ^{+0.1} _{-0.1}	-0.09 ^{+0.02} _{-0.02}	> 0.2	0	0
JADESGDS-8179	53.155796	-27.815203	28.5	6.71	-18.4 ^{+0.1} _{-0.1}	7.4 ^{+0.1} _{-0.1}	0.1 ^{+0.1} _{-0.1}	-2.4 ^{+0.1} _{-0.1}	-1.07 ^{+0.15} _{-0.15}	0.7 ± 0.1	0	1
JADESGDS-8408	53.115379	-27.814774	27.4	5.76	-19.2 ^{+0.1} _{-0.1}	7.6 ^{+0.1} _{-0.1}	0.2 ^{+0.1} _{-0.1}	-2.5 ^{+0.1} _{-0.1}	-0.53 ^{+0.01} _{-0.01}	0.8 ± 0.1	0	0
JADESGDS-9326	53.118526	-27.812975	27.2	5.12	-19.3 ^{+0.1} _{-0.1}	8.2 ^{+0.1} _{-0.1}	0.9 ^{+0.1} _{-0.1}	-1.7 ^{+0.1} _{-0.1}	-0.33 ^{+0.01} _{-0.01}	0.8 ± 0.2	0	0
JADESGDS-10902	53.14946	-27.809797	28.4	5.05	-17.8 ^{+0.1} _{-0.1}	7.8 ^{+0.2} _{-0.2}	0.0 ^{+0.1} _{-0.1}	-2.3 ^{+0.1} _{-0.1}	-0.36 ^{+0.01} _{-0.01}	0.7 ± 0.2	0	0
JADESGDS-11449	53.11042	-27.808928	28.1	5.94	-18.6 ^{+0.1} _{-0.1}	7.5 ^{+0.2} _{-0.2}	0.2 ^{+0.1} _{-0.1}	-2.6 ^{+0.1} _{-0.1}	-0.75 ^{+0.02} _{-0.02}	0.7 ± 0.1	0	0
JADESGDS-11841	53.129726	-27.80818	28.6	5.56	-18.5 ^{+0.1} _{-0.1}	8.2 ^{+0.2} _{-0.2}	0.0 ^{+0.1} _{-0.1}	-2.5 ^{+0.1} _{-0.1}	-0.79 ^{+0.05} _{-0.05}	0.7 ± 0.2	0	0
JADESGDS-12147	53.130581	-27.807722	28.3	5.62	-18.2 ^{+0.1} _{-0.1}	8.8 ^{+0.1} _{-0.1}	0.2 ^{+0.1} _{-0.1}	-2.2 ^{+0.1} _{-0.1}	-0.23 ^{+0.11} _{-0.11}	0.1 ± 0.3	0	0
JADESGDS-14986	53.167301	-27.802874	28.8	5.82	-17.3 ^{+0.1} _{-0.1}	8.1 ^{+0.1} _{-0.1}	-0.1 ^{+0.1} _{-0.1}	-2.5 ^{+0.2} _{-0.2}	-0.46 ^{+0.04} _{-0.04}	0.8 ± 0.2	0	0
JADESGDS-16254	53.156235	-27.800737	29.4	5.06	-17.0 ^{+0.1} _{-0.1}	7.9 ^{+0.1} _{-0.1}	-0.3 ^{+0.2} _{-0.2}	-2.1 ^{+0.1} _{-0.2}	-0.99 ^{+0.08} _{-0.08}	> 0.7	0	1
JADESGDS-17941	53.128735	-27.797876	28.6	5.44	-17.7 ^{+0.1} _{-0.1}	9.0 ^{+0.1} _{-0.1}	0.0 ^{+0.1} _{-0.1}	-2.5 ^{+0.1} _{-0.1}	-0.33 ^{+0.06} _{-0.06}	0.7 ± 0.2	0	0
JADESGDS-18169	53.121758	-27.797638	27.0	5.94	-19.5 ^{+0.1} _{-0.1}	7.5 ^{+0.1} _{-0.1}	0.6 ^{+0.1} _{-0.1}	-2.6 ^{+0.1} _{-0.1}	-1.04 ^{+0.03} _{-0.03}	0.8 ± 0.1	0	1
JADESGDS-18204	53.115837	-27.797552	27.9	5.12	-18.6 ^{+0.1} _{-0.1}	8.5 ^{+0.1} _{-0.1}	0.4 ^{+0.1} _{-0.1}	-2.0 ^{+0.1} _{-0.1}	-0.71 ^{+0.01} _{-0.01}	> 0.1	0	0
JADESGDS-18784	53.123005	-27.796614	28.5	5.44	-17.7 ^{+0.1} _{-0.1}	9.1 ^{+0.1} _{-0.1}	0.0 ^{+0.1} _{-0.1}	-2.5 ^{+0.1} _{-0.1}	-1.02 ^{+0.04} _{-0.04}	0.8 ± 0.3	0	1
JADESGDS-29538	53.169044	-27.778835	28.4	6.63	-18.6 ^{+0.1} _{-0.1}	8.0 ^{+0.1} _{-0.1}	0.1 ^{+0.1} _{-0.1}	-2.2 ^{+0.1} _{-0.1}	-0.83 ^{+0.02} _{-0.02}	0.6 ± 0.1	0	0
JADESGDS-29878	53.130047	-27.778389	26.1	5.57	-20.0 ^{+0.1} _{-0.1}	8.1 ^{+0.1} _{-0.1}	0.8 ^{+0.1} _{-0.1}	-2.4 ^{+0.1} _{-0.2}	0.47 ^{+0.16} _{-0.16}	-	1	-
JADESGDS-30683	53.127663	-27.776951	28.8	5.04	-17.8 ^{+0.1} _{-0.1}	7.8 ^{+0.1} _{-0.1}	-0.1 ^{+0.1} _{-0.1}	-2.3 ^{+0.1} _{-0.1}	-0.37 ^{+0.05} _{-0.05}	-	0	0
JADESGDS-31651	53.156101	-27.775881	26.8	6.10	-19.6 ^{+0.1} _{-0.1}	9.7 ^{+0.1} _{-0.1}	1.3 ^{+0.1} _{-0.1}	-1.5 ^{+0.1} _{-0.1}	0.01 ^{+0.02} _{-0.02}	0.3 ± 0.2	0	0
JADESGDS-32171	53.175819	-27.774473	27.7	6.33	-19.0 ^{+0.1} _{-0.1}	8.7 ^{+0.1} _{-0.1}	0.6 ^{+0.1} _{-0.1}	-2.0 ^{+0.1} _{-0.1}	-0.62 ^{+0.02} _{-0.02}	0.8 ± 0.1	0	0
JADESGDS-33170	53.134914	-27.772709	26.9	6.33	-19.8 ^{+0.1} _{-0.1}	7.8 ^{+0.1} _{-0.1}	0.4 ^{+0.1} _{-0.1}	-2.6 ^{+0.1} _{-0.1}	-0.62 ^{+0.01} _{-0.01}	0.8 ± 0.1	0	0
JADESGDS-33350	53.166595	-27.772406	28.1	6.33	-18.8 ^{+0.1} _{-0.1}	7.6 ^{+0.1} _{-0.1}	0.2 ^{+0.1} _{-0.1}	-2.2 ^{+0.1} _{-0.1}	-0.26 ^{+0.02} _{-0.02}	0.4 ± 0.1	0	0
JADESGDS-33803	53.160625	-27.771608	28.2	5.97	-18.7 ^{+0.1} _{-0.1}	7.4 ^{+0.2} _{-0.2}	0.2 ^{+0.1} _{-0.1}	-2.6 ^{+0.1} _{-0.1}	-0.48 ^{+0.03} _{-0.03}	1.1 ± 0.2	0	0
JADESGDS-34065	53.176529	-27.771109	28.5	5.89	-18.1 ^{+0.1} _{-0.1}	7.0 ^{+0.1} _{-0.1}	-0.3 ^{+0.1} _{-0.1}	-2.7 ^{+0.1} _{-0.1}	-0.53 ^{+0.02} _{-0.02}	-	0	0
JADESGDS-34138	53.176556	-27.771128	27.6	5.89	-18.0 ^{+0.1} _{-0.1}	8.1 ^{+0.2} _{-0.2}	0.5 ^{+0.1} _{-0.1}	-2.7 ^{+0.1} _{-0.1}	0.05 ^{+0.01} _{-0.01}	0.7 ± 0.1	0	0
JADESGDS-35365	53.134232	-27.768915	28.1	7.04	-18.3 ^{+0.1} _{-0.1}	7.7 ^{+0.1} _{-0.1}	0.3 ^{+0.1} _{-0.1}	-2.5 ^{+0.1} _{-0.1}	-0.40 ^{+0.01} _{-0.01}	0.6 ± 0.2	0	0
CEERS1-21407	215.00113	53.011265	27.5	7.10	-19.5 ^{+0.1} _{-0.1}	7.8 ^{+0.1} _{-0.1}	0.5 ^{+0.1} _{-0.1}	-2.4 ^{+0.1} _{-0.1}	-0.92 ^{+0.03} _{-0.03}	-	0	0
CEERS1-23089	215.01086	53.013317	25.9	5.10	-20.6 ^{+0.1} _{-0.1}	9.6 ^{+0.1} _{-0.1}	1.3 ^{+0.1} _{-0.1}	-1.9 ^{+0.1} _{-0.1}	0.03 ^{+0.01} _{-0.01}	0.8 ± 0.3	0	0
CEERS2-1767	214.87251	52.875961	27.7	5.67	-18.4 ^{+0.2} _{-0.2}	7.4 ^{+0.2} _{-0.2}	0.3 ^{+0.1} _{-0.1}	-2.4 ^{+0.2} _{-0.3}	-0.84 ^{+0.03} _{-0.03}	0.6 ± 0.3	0	0
CEERS2-7005	214.88797	52.888271	26.9	5.27	-19.5 ^{+0.1} _{-0.1}	9.0 ^{+0.1} _{-0.1}	1.0 ^{+0.1} _{-0.1}	-1.8 ^{+0.1} _{-0.1}	-0.31 ^{+0.01} _{-0.01}	0.7 ± 0.3	0	0
CEERS3-9221	214.81299	52.83424	26.9	7.18	-20.0 ^{+0.1} _{-0.1}	8.2 ^{+0.1} _{-0.1}	0.8 ^{+0.1} _{-0.1}	-2.4 ^{+0.1} _{-0.1}	-0.55 ^{+0.02} _{-0.02}	-	0	0
CEERS3-9625	214.81163	52.837231	26.8	5.28	-19.9 ^{+0.1} _{-0.1}	8.4 ^{+0.1} _{-0.1}	1.0 ^{+0.1} _{-0.1}	-1.8 ^{+0.1} _{-0.1}	-0.31 ^{+0.02} _{-0.02}	-	0	0
CEERS3-15767	214.80647	52.878826	27.0	6.11	-19.4 ^{+0.1} _{-0.1}	7.8 ^{+0.3} _{-0.3}	0.7 ^{+0.1} _{-0.1}	-2.6 ^{+0.4} _{-0.4}	-0.28 ^{+0.02} _{-0.02}	0.8 ± 0.1	0	0
CEERS3-18419	214.82896	52.875694	26.5	5.77	-20.4 ^{+0.1} _{-0.2}	9.5 ^{+0.1} _{-0.1}	0.9 ^{+0.1} _{-0.1}	-2.3 ^{+0.6} _{-0.1}	-0.32 ^{+0.03} _{-0.03}	0.8 ± 0.1	0	0
CEERS3-20932	214.83617	52.882668	25.6	6.00	-21.3 ^{+0.1} _{-0.1}	9.1 ^{+0.1} _{-0.1}	1.3 ^{+0.1} _{-0.1}	-2.6 ^{+0.1} _{-0.1}	-0.33 ^{+0.01} _{-0.01}	0.8 ± 0.1	0	0
CEERS3-21899	214.86159	52.876141	27.5	7.17	-19.9 ^{+0.1} _{-0.1}	7.5 ^{+0.1} _{-0.1}	0.5 ^{+0.1} _{-0.1}	-2.7 ^{+0.1} _{-0.1}	-0.23 ^{+0.06} _{-0.06}	-	0	0
CEERS4-2257	214.75339	52.74099	26.6	5.45	-19.9 ^{+0.1} _{-0.1}	9.8 ^{+0.1} _{-0.1}	1.2 ^{+0.1} _{-0.1}	-1.6 ^{+0.1} _{-0.1}	-0.46 ^{+0.02} _{-0.02}	-	0	0
CEERS4-9402	214.74466	52.750313	25.9	5.21	-20.6 ^{+0.1} _{-0.1}	9.7 ^{+0.1} _{-0.1}	1.7 ^{+0.1} _{-0.1}	-1.3 ^{+0.1} _{-0.1}	-0.29 ^{+0.01} _{-0.01}	0.5 ± 0.2	0	0
CEERS4-12992	214.77391	52.780613	27.1	5.43	-19.8 ^{+0.1} _{-0.1}	9.3 ^{+0.1} _{-0.1}	0.6 ^{+0.1} _{-0.1}	-2.7 ^{+0.2} _{-0.1}	-0.67 ^{+0.02} _{-0.02}	-	0	0
CEERS5-20468	214.89146	52.867447	27.3	5.15	-19.4 ^{+0.1} _{-0.1}	8.5 ^{+0.1} _{-0.1}	0.5 ^{+0.1} _{-0.1}	-2.2 ^{+0.2} _{-0.1}	-0.41 ^{+0.02} _{-0.02}	-	0	0
CEERS6-7832	214.82341	52.830288	26.7	5.25	-19.6 ^{+0.1} _{-0.1}	8.6 ^{+0.1} _{-0.1}	1.3 ^{+0.1} _{-0.1}	-1.4 ^{+0.1} _{-0.1}	-0.87 ^{+0.02} _{-0.02}	0.7 ± 0.1	0	0
CEERS6-8960	214.83157	52.831512	27.8	7.06	-20.5 ^{+0.1} _{-0.1}	8.2 ^{+0.2} _{-0.2}	0.5 ^{+0.1} _{-0.1}	-2.2 ^{+0.2} _{-0.2}	-0.48 ^{+0.29} _{-0.29}	-	0	0
CEERS6-10587	214.8672	52.83675	27.2	6.06	-19.9 ^{+0.1} _{-0.1}	9.1 ^{+0.2} _{-0.2}	0.6 ^{+0.1} _{-0.1}	-2.5 ^{+0.4} _{-0.1}	-0.26 ^{+0.02} _{-0.02}	-	0	0

Table 5 continued

Table 5 (continued)

ID	R.A.	Decl.	m_{UV}	z^\dagger	M_{UV}	M_*	SFR	β_{UV}	$R_{e,maj}$	[O III]/H β	f_{gal}^*	f_{com}^*
	deg.	deg.	mag		mag	$\log M_\odot$	$\log M_\odot/\text{yr}$		log kpc	log		
CEERS6-12682	214.87643	52.839428	27.1	6.05	$-19.1^{+0.1}_{-0.1}$	$8.6^{+0.3}_{-0.3}$	$0.7^{+0.1}_{-0.1}$	$-2.7^{+0.2}_{-0.1}$	$-0.06^{+0.03}_{-0.03}$	–	0	0
CEERS6-14083	214.85913	52.8536	27.5	7.12	$-19.5^{+0.1}_{-0.1}$	$8.4^{+0.3}_{-0.3}$	$0.6^{+0.1}_{-0.1}$	$-2.3^{+0.1}_{-0.2}$	$-0.27^{+0.03}_{-0.03}$	–	0	0
CEERS6-14120	214.85907	52.853653	27.4	7.12	$-19.1^{+0.1}_{-0.1}$	$8.6^{+0.1}_{-0.1}$	$0.9^{+0.1}_{-0.1}$	$-1.9^{+0.1}_{-0.1}$	$0.03^{+0.03}_{-0.03}$	–	0	0
CEERS6-15136	214.86436	52.853672	25.7	5.67	$-20.9^{+0.1}_{-0.1}$	$9.5^{+0.1}_{-0.1}$	$1.2^{+0.1}_{-0.1}$	$-2.4^{+0.1}_{-0.1}$	$0.17^{+0.06}_{-0.06}$	–	1	–
CEERS6-15334	214.89635	52.838524	27.0	5.27	$-18.8^{+0.1}_{-0.2}$	$9.4^{+0.1}_{-0.1}$	$0.7^{+0.1}_{-0.1}$	$-2.1^{+0.4}_{-0.1}$	$0.17^{+0.03}_{-0.03}$	–	0	0
CEERS6-22118	214.89142	52.86747	27.2	5.15	$-18.9^{+0.1}_{-0.2}$	$8.8^{+0.3}_{-0.3}$	$0.8^{+0.2}_{-0.2}$	$-1.9^{+0.3}_{-0.2}$	$-0.35^{+0.02}_{-0.02}$	–	0	0
CEERS7-3779	215.03642	52.94175	26.8	5.10	$-19.2^{+0.1}_{-0.1}$	$8.7^{+0.2}_{-0.2}$	$0.7^{+0.1}_{-0.1}$	$-2.2^{+0.3}_{-0.1}$	$-0.70^{+0.08}_{-0.08}$	–	0	0
CEERS7-18822	215.09093	52.951546	26.9	5.50	$-19.4^{+0.1}_{-0.1}$	$9.7^{+0.1}_{-0.1}$	$1.0^{+0.2}_{-0.2}$	$-1.8^{+0.2}_{-0.2}$	$-0.32^{+0.02}_{-0.02}$	1.0 ± 0.2	0	0
CEERS7-19909	215.091	52.954319	25.3	6.99	$-19.6^{+0.1}_{-0.1}$	$8.6^{+0.1}_{-0.1}$	$0.6^{+0.1}_{-0.1}$	$-2.2^{+0.2}_{-0.1}$	$0.97^{+0.53}_{-0.53}$	–	1	–
CEERS8-18483	215.03053	52.902603	27.0	5.01	$-20.2^{+0.1}_{-0.1}$	$8.5^{+0.1}_{-0.1}$	$0.6^{+0.1}_{-0.1}$	$-2.2^{+0.1}_{-0.1}$	$-0.77^{+0.02}_{-0.02}$	–	0	0
CEERS9-23526	214.89163	52.815952	27.9	5.67	$-18.6^{+0.1}_{-0.1}$	$7.0^{+0.1}_{-0.1}$	$0.3^{+0.1}_{-0.1}$	$-2.6^{+0.1}_{-0.1}$	$-1.03^{+0.06}_{-0.06}$	–	0	1
CEERS10-4066	214.7991	52.725136	27.6	6.09	$-18.8^{+0.1}_{-0.1}$	$7.3^{+0.2}_{-0.2}$	$0.5^{+0.1}_{-0.1}$	$-2.5^{+0.1}_{-0.1}$	$-0.23^{+0.03}_{-0.03}$	–	0	0
CEERS10-8944	214.78981	52.730808	27.1	6.74	$-19.4^{+0.1}_{-0.1}$	$9.1^{+0.1}_{-0.1}$	$0.7^{+0.1}_{-0.1}$	$-2.4^{+0.1}_{-0.1}$	$-0.43^{+0.02}_{-0.02}$	–	0	0
CEERS10-10494	214.78569	52.731571	27.6	5.29	$-19.2^{+0.1}_{-0.1}$	$8.8^{+0.1}_{-0.1}$	$0.6^{+0.1}_{-0.1}$	$-1.9^{+0.1}_{-0.1}$	$-1.02^{+0.06}_{-0.06}$	–	0	1
CEERS10-11869	214.81262	52.75486	27.1	5.43	$-19.3^{+0.1}_{-0.2}$	$9.3^{+0.1}_{-0.1}$	$0.6^{+0.1}_{-0.1}$	$-2.6^{+0.4}_{-0.2}$	$-0.27^{+0.02}_{-0.02}$	–	0	0
CEERS10-13801	214.80548	52.754742	27.6	5.86	$-18.6^{+0.1}_{-0.1}$	$8.8^{+0.3}_{-0.3}$	$0.4^{+0.1}_{-0.1}$	$-2.6^{+0.1}_{-0.1}$	$-0.35^{+0.04}_{-0.04}$	–	0	0
F090W-dropout												
J1235-15721	188.96646	4.9614086	27.4	$7.4^{+0.3}_{-0.2}$	$-19.6^{+0.1}_{-0.1}$	$8.2^{+0.3}_{-0.3}$	$0.7^{+0.1}_{-0.1}$	$-2.5^{+0.2}_{-0.2}$	$-0.67^{+0.02}_{-0.02}$	–	0	0
NEP-2312	260.68854	65.714592	26.1	$7.3^{+0.1}_{-0.1}$	$-20.8^{+0.1}_{-0.1}$	$8.9^{+0.1}_{-0.1}$	$1.3^{+0.1}_{-0.1}$	$-2.0^{+0.1}_{-0.1}$	$-0.28^{+0.01}_{-0.01}$	–	0	0
NEP-4843	260.6767	65.720131	27.5	$7.3^{+0.4}_{-0.2}$	$-19.4^{+0.1}_{-0.1}$	$8.5^{+0.2}_{-0.2}$	$0.7^{+0.1}_{-0.1}$	$-2.1^{+0.2}_{-0.2}$	$-0.32^{+0.04}_{-0.04}$	–	0	0
NEP-15634	260.70917	65.740883	27.2	$7.3^{+0.1}_{-0.1}$	$-19.5^{+0.1}_{-0.1}$	$8.3^{+0.1}_{-0.1}$	$0.9^{+0.1}_{-0.1}$	$-2.0^{+0.1}_{-0.1}$	$-0.37^{+0.02}_{-0.02}$	–	0	0
NEP-24767	260.69934	65.760391	27.5	$8.2^{+0.3}_{-0.3}$	$-19.8^{+0.1}_{-0.1}$	$8.6^{+0.2}_{-0.2}$	$0.8^{+0.1}_{-0.1}$	$-2.1^{+0.1}_{-0.1}$	$-0.21^{+0.01}_{-0.01}$	–	1	–
NEP-38016	260.69568	65.785934	26.6	$8.3^{+0.2}_{-0.2}$	$-20.8^{+0.1}_{-0.1}$	$8.1^{+0.1}_{-0.1}$	$1.0^{+0.1}_{-0.1}$	$-2.6^{+0.1}_{-0.1}$	$-1.05^{+0.03}_{-0.03}$	–	0	1
NEP-41263	260.70978	65.790955	27.9	$7.2^{+0.5}_{-0.3}$	$-19.0^{+0.1}_{-0.1}$	$8.7^{+0.1}_{-0.1}$	$0.5^{+0.1}_{-0.1}$	$-2.3^{+0.2}_{-0.2}$	$-0.50^{+0.04}_{-0.04}$	–	0	0
NEP-44420	260.7374	65.795807	27.0	$7.3^{+0.1}_{-0.1}$	$-20.9^{+0.1}_{-0.1}$	$8.5^{+0.1}_{-0.1}$	$0.9^{+0.1}_{-0.1}$	$-2.1^{+0.1}_{-0.1}$	$-0.35^{+0.02}_{-0.02}$	–	0	0
NEP-48900	260.72177	65.805756	25.9	$8.5^{+0.2}_{-0.2}$	$-20.8^{+0.1}_{-0.1}$	$9.4^{+0.1}_{-0.1}$	$1.1^{+0.1}_{-0.1}$	$-2.6^{+0.1}_{-0.1}$	$0.07^{+0.05}_{-0.05}$	–	1	–
NEP-55180	260.75189	65.820541	27.4	$7.2^{+0.1}_{-0.1}$	$-20.5^{+0.1}_{-0.1}$	$8.4^{+0.1}_{-0.1}$	$0.9^{+0.1}_{-0.1}$	$-1.9^{+0.1}_{-0.1}$	$-0.79^{+0.02}_{-0.02}$	–	0	0
NEP-55261	260.73605	65.819099	27.3	$8.4^{+0.2}_{-0.3}$	$-19.6^{+0.1}_{-0.1}$	$9.0^{+0.3}_{-0.3}$	$0.8^{+0.1}_{-0.1}$	$-2.5^{+0.1}_{-0.1}$	$-0.40^{+0.03}_{-0.03}$	–	0	0
NEP-57629	260.724	65.821655	26.8	$8.5^{+0.2}_{-0.3}$	$-20.1^{+0.1}_{-0.1}$	$8.1^{+0.2}_{-0.2}$	$1.0^{+0.1}_{-0.1}$	$-2.6^{+0.1}_{-0.1}$	$-0.16^{+0.03}_{-0.03}$	–	0	0
A2744-3796	3.6171718	-30.425545	26.2	9.31	$-21.7^{+0.1}_{-0.1}$	$9.3^{+0.1}_{-0.1}$	$1.5^{+0.1}_{-0.1}$	$-2.0^{+0.1}_{-0.1}$	$-0.57^{+0.04}_{-0.04}$	–	0	0
A2744-5260	3.6085184	-30.418537	26.0	7.29	$-21.1^{+0.1}_{-0.1}$	$8.5^{+0.1}_{-0.1}$	$1.2^{+0.1}_{-0.1}$	$-2.3^{+0.1}_{-0.1}$	$-0.39^{+0.02}_{-0.02}$	0.9 ± 0.1	0	0
A2744-15395	3.5960913	-30.385817	27.6	7.89	$-19.1^{+0.1}_{-0.1}$	$8.2^{+0.1}_{-0.1}$	$0.6^{+0.1}_{-0.1}$	$-2.2^{+0.1}_{-0.1}$	$-0.48^{+0.09}_{-0.09}$	0.9 ± 0.1	0	0
A2744-16933	3.6033962	-30.382244	27.7	7.88	$-20.6^{+0.1}_{-0.1}$	$9.4^{+0.1}_{-0.1}$	$0.7^{+0.1}_{-0.1}$	$-2.0^{+0.1}_{-0.1}$	$-0.61^{+0.58}_{-0.58}$	–	0	0
A2744-16993	3.6038527	-30.382246	27.8	7.88	$-20.9^{+0.1}_{-0.1}$	$9.6^{+0.3}_{-0.3}$	$1.3^{+0.1}_{-0.1}$	$-1.2^{+0.1}_{-0.1}$	$-0.55^{+0.12}_{-0.12}$	1.0 ± 0.3	0	0
A2744-17308	3.6064591	-30.380976	27.6	7.88	$-20.0^{+0.1}_{-0.1}$	$9.0^{+0.4}_{-0.4}$	$0.6^{+0.1}_{-0.1}$	$-2.2^{+0.1}_{-0.1}$	$-0.52^{+0.03}_{-0.03}$	> 0.8	0	0
A2744-17424	3.6065702	-30.380907	27.5	7.88	$-19.3^{+0.1}_{-0.1}$	$9.1^{+0.1}_{-0.1}$	$1.1^{+0.1}_{-0.1}$	$-1.7^{+0.1}_{-0.1}$	$-0.27^{+0.06}_{-0.06}$	> 0.8	0	0
A2744-17751	3.6045153	-30.380447	27.0	7.88	$-20.2^{+0.1}_{-0.1}$	$8.3^{+0.1}_{-0.1}$	$0.8^{+0.1}_{-0.1}$	$-2.1^{+0.1}_{-0.1}$	$-0.97^{+0.20}_{-0.20}$	0.9 ± 0.1	0	0
A2744-18185	3.6013498	-30.379196	27.4	7.88	$-19.8^{+0.1}_{-0.1}$	$8.3^{+0.1}_{-0.1}$	$0.8^{+0.1}_{-0.1}$	$-2.1^{+0.1}_{-0.1}$	$-1.40^{+0.04}_{-0.04}$	0.7 ± 0.1	0	1
A2744-26748	3.4905653	-30.360378	27.9	$8.7^{+0.2}_{-0.2}$	$-19.7^{+0.1}_{-0.1}$	$8.8^{+0.7}_{-0.7}$	$0.5^{+0.1}_{-0.1}$	$-2.5^{+0.1}_{-0.1}$	$-0.60^{+0.06}_{-0.06}$	–	0	0
A2744-29120	3.4907956	-30.354845	27.2	$7.3^{+0.1}_{-0.1}$	$-19.8^{+0.1}_{-0.1}$	$8.1^{+0.2}_{-0.2}$	$0.7^{+0.1}_{-0.1}$	$-2.4^{+0.1}_{-0.1}$	$-0.17^{+0.06}_{-0.06}$	–	0	0
A2744-32915	3.511811	-30.346846	28.2	$7.8^{+0.2}_{-0.3}$	$-19.4^{+0.1}_{-0.1}$	$8.7^{+0.1}_{-0.1}$	$1.3^{+0.1}_{-0.1}$	$-1.1^{+0.1}_{-0.1}$	$-0.88^{+0.08}_{-0.08}$	–	0	0
A2744-32950	3.5119343	-30.346668	27.9	$7.7^{+0.3}_{-0.5}$	$-19.1^{+0.1}_{-0.1}$	$9.0^{+0.1}_{-0.1}$	$0.7^{+0.1}_{-0.1}$	$-1.9^{+0.1}_{-0.1}$	$-0.37^{+0.05}_{-0.05}$	–	0	0
A2744-39390	3.4519746	-30.326588	27.9	$8.3^{+0.3}_{-0.3}$	$-19.1^{+0.1}_{-0.1}$	$8.8^{+0.2}_{-0.2}$	$0.5^{+0.1}_{-0.1}$	$-2.4^{+0.1}_{-0.1}$	$-0.56^{+0.07}_{-0.07}$	–	0	0

Table 5 continued

Table 5 (continued)

ID	R.A.	Decl.	m_{UV}	z^\dagger	M_{UV}	M_*	SFR	β_{UV}	$R_{e,maj}$	[O III]/H β	f_{gal}^*	f_{com}^*
	deg.	deg.	mag		mag	log M_\odot	log M_\odot/yr		log kpc	log		
A2744-40364	3.4806123	-30.323521	27.9	$8.5^{+0.2}_{-0.2}$	$-18.8^{+0.1}_{-0.1}$	$9.0^{+0.3}_{-0.3}$	$0.5^{+0.1}_{-0.1}$	$-2.2^{+0.1}_{-0.1}$	$-0.71^{+0.04}_{-0.04}$	–	0	0
PRIMERUDS-200	34.245823	-5.325891	26.3	$10.2^{+0.4}_{-0.9}$	$-21.9^{+0.1}_{-0.1}$	$9.5^{+0.1}_{-0.1}$	$1.3^{+0.1}_{-0.1}$	$-2.3^{+0.1}_{-0.1}$	$-0.40^{+0.13}_{-0.13}$	–	0	0
PRIMERUDS-1090	34.346313	-5.3226662	26.3	$7.6^{+0.3}_{-0.3}$	$-19.8^{+0.1}_{-0.1}$	$8.8^{+0.1}_{-0.1}$	$1.1^{+0.1}_{-0.1}$	$-2.5^{+0.1}_{-0.1}$	$-0.06^{+0.03}_{-0.03}$	–	0	0
PRIMERUDS-1498	34.317928	-5.3223157	26.7	$8.1^{+0.3}_{-0.3}$	$-19.8^{+0.1}_{-0.1}$	$8.5^{+0.1}_{-0.1}$	$1.2^{+0.1}_{-0.1}$	$-2.0^{+0.1}_{-0.1}$	$-0.11^{+0.04}_{-0.04}$	–	0	0
PRIMERUDS-4972	34.380459	-5.3183036	26.2	$8.6^{+0.3}_{-0.2}$	$-20.9^{+0.1}_{-0.1}$	$8.6^{+0.1}_{-0.1}$	$1.2^{+0.1}_{-0.1}$	$-2.2^{+0.1}_{-0.1}$	$-0.28^{+0.03}_{-0.03}$	–	0	0
PRIMERUDS-9713	34.319019	-5.3156524	27.3	$7.9^{+0.4}_{-0.5}$	$-19.4^{+0.1}_{-0.1}$	$8.2^{+0.1}_{-0.1}$	$0.8^{+0.1}_{-0.1}$	$-2.3^{+0.1}_{-0.1}$	$-0.99^{+0.05}_{-0.05}$	–	0	1
PRIMERUDS-10989	34.484421	-5.3133621	26.3	$8.0^{+0.3}_{-0.3}$	$-20.6^{+0.1}_{-0.1}$	$8.8^{+0.2}_{-0.2}$	$1.2^{+0.1}_{-0.1}$	$-2.6^{+0.1}_{-0.2}$	$0.05^{+0.04}_{-0.04}$	–	0	0
PRIMERUDS-11193	34.49094	-5.3132	26.0	$7.2^{+0.1}_{-0.1}$	$-20.5^{+0.1}_{-0.1}$	$8.5^{+0.1}_{-0.1}$	$1.1^{+0.1}_{-0.1}$	$-2.3^{+0.1}_{-0.1}$	$-0.15^{+0.02}_{-0.02}$	–	0	0
PRIMERUDS-12222	34.361069	-5.3136678	26.4	$7.3^{+0.1}_{-0.1}$	$-20.4^{+0.1}_{-0.1}$	$8.3^{+0.1}_{-0.1}$	$1.0^{+0.1}_{-0.1}$	$-2.3^{+0.1}_{-0.1}$	$-0.72^{+0.03}_{-0.03}$	–	0	0
PRIMERUDS-13469	34.483696	-5.3117156	27.2	$8.0^{+0.5}_{-0.7}$	$-19.8^{+0.1}_{-0.1}$	$9.0^{+0.1}_{-0.1}$	$0.8^{+0.1}_{-0.1}$	$-2.6^{+0.2}_{-0.1}$	$-0.22^{+0.05}_{-0.05}$	–	0	0
PRIMERUDS-16114	34.521278	-5.3095951	25.8	$8.9^{+0.1}_{-0.2}$	$-20.9^{+0.1}_{-0.1}$	$9.1^{+0.6}_{-0.6}$	$1.1^{+0.1}_{-0.1}$	$-2.7^{+0.2}_{-0.1}$	$0.07^{+0.02}_{-0.02}$	–	1	–
PRIMERUDS-21862	34.451874	-5.3065	27.0	$8.8^{+0.4}_{-0.3}$	$-19.6^{+0.1}_{-0.1}$	$9.1^{+0.5}_{-0.5}$	$0.9^{+0.1}_{-0.1}$	$-2.6^{+0.1}_{-0.1}$	$-0.22^{+0.05}_{-0.05}$	–	0	0
PRIMERUDS-23042	34.301533	-5.3071699	26.3	$7.9^{+0.2}_{-0.4}$	$-20.4^{+0.1}_{-0.1}$	$9.6^{+0.1}_{-0.1}$	$1.2^{+0.1}_{-0.1}$	$-2.1^{+0.1}_{-0.1}$	$-0.24^{+0.02}_{-0.02}$	–	0	0
PRIMERUDS-30574	34.483742	-5.300765	27.1	$8.1^{+0.3}_{-0.3}$	$-19.3^{+0.1}_{-0.1}$	$8.2^{+0.4}_{-0.4}$	$0.8^{+0.1}_{-0.1}$	$-2.8^{+0.1}_{-0.1}$	$-0.31^{+0.04}_{-0.04}$	–	0	0
PRIMERUDS-31216	34.419689	-5.30094	27.2	$7.3^{+0.1}_{-0.1}$	$-19.4^{+0.1}_{-0.1}$	$9.0^{+0.4}_{-0.4}$	$0.8^{+0.1}_{-0.1}$	$-2.1^{+0.1}_{-0.1}$	$-0.59^{+0.05}_{-0.05}$	–	0	0
PRIMERUDS-31414	34.364422	-5.3012862	27.2	$8.5^{+0.3}_{-0.4}$	$-19.7^{+0.1}_{-0.1}$	$8.8^{+0.1}_{-0.1}$	$0.8^{+0.1}_{-0.1}$	$-2.6^{+0.2}_{-0.1}$	$-0.59^{+0.05}_{-0.05}$	–	0	0
PRIMERUDS-33464	34.293663	-5.3005662	26.2	$8.6^{+0.1}_{-0.2}$	$-21.3^{+0.1}_{-0.1}$	$8.9^{+0.1}_{-0.1}$	$1.2^{+0.1}_{-0.1}$	$-2.5^{+0.1}_{-0.1}$	$-0.76^{+0.26}_{-0.26}$	–	0	0
PRIMERUDS-35245	34.529091	-5.2968173	27.4	$7.3^{+0.1}_{-0.1}$	$-19.9^{+0.1}_{-0.1}$	$7.7^{+0.2}_{-0.2}$	$0.6^{+0.1}_{-0.1}$	$-2.4^{+0.1}_{-0.1}$	$-0.89^{+0.06}_{-0.06}$	–	0	0
PRIMERUDS-38781	34.415279	-5.2941837	26.3	$7.3^{+0.2}_{-0.2}$	$-21.1^{+0.1}_{-0.1}$	$8.8^{+0.3}_{-0.3}$	$1.3^{+0.1}_{-0.1}$	$-2.0^{+0.1}_{-0.1}$	$-0.08^{+0.16}_{-0.16}$	–	0	0
PRIMERUDS-41711	34.260204	-5.2925024	26.0	$7.3^{+0.1}_{-0.1}$	$-20.9^{+0.1}_{-0.1}$	$8.8^{+0.2}_{-0.2}$	$1.2^{+0.1}_{-0.1}$	$-2.2^{+0.1}_{-0.1}$	$-0.02^{+0.02}_{-0.02}$	–	0	0
PRIMERUDS-42221	34.33025	-5.2913198	26.8	$7.2^{+0.3}_{-0.2}$	$-20.3^{+0.1}_{-0.1}$	$8.9^{+0.2}_{-0.2}$	$1.1^{+0.2}_{-0.2}$	$-1.9^{+0.2}_{-0.2}$	$-0.62^{+0.03}_{-0.03}$	–	0	0
PRIMERUDS-42290	34.330235	-5.2912478	26.7	$7.2^{+0.2}_{-0.2}$	$-20.3^{+0.1}_{-0.1}$	$9.0^{+0.2}_{-0.2}$	$1.2^{+0.2}_{-0.2}$	$-1.8^{+0.2}_{-0.2}$	$-0.50^{+0.02}_{-0.02}$	–	0	0
PRIMERUDS-43150	34.323875	-5.2904172	26.2	$7.5^{+0.5}_{-0.3}$	$-21.2^{+0.1}_{-0.1}$	$9.3^{+0.1}_{-0.1}$	$1.1^{+0.1}_{-0.1}$	$-2.3^{+0.2}_{-0.1}$	$-0.04^{+0.06}_{-0.06}$	–	0	0
PRIMERUDS-43160	34.263737	-5.2909522	26.6	$7.3^{+0.1}_{-0.1}$	$-20.1^{+0.1}_{-0.1}$	$8.4^{+0.2}_{-0.2}$	$1.0^{+0.1}_{-0.1}$	$-2.3^{+0.1}_{-0.1}$	$-0.74^{+0.03}_{-0.03}$	–	0	0
PRIMERUDS-43179	34.323917	-5.2903838	27.0	$7.4^{+0.5}_{-0.2}$	$-21.0^{+0.1}_{-0.1}$	$8.6^{+0.1}_{-0.1}$	$0.8^{+0.1}_{-0.1}$	$-2.2^{+0.1}_{-0.1}$	$-0.27^{+0.03}_{-0.03}$	–	0	0
PRIMERUDS-49663	34.399944	-5.2839613	25.9	$7.3^{+0.1}_{-0.1}$	$-21.4^{+0.1}_{-0.1}$	$8.6^{+0.2}_{-0.2}$	$1.3^{+0.1}_{-0.1}$	$-2.3^{+0.1}_{-0.1}$	$-0.24^{+0.05}_{-0.05}$	–	0	0
PRIMERUDS-66080	34.280521	-5.2683573	26.7	$7.3^{+0.1}_{-0.1}$	$-20.3^{+0.1}_{-0.1}$	$8.0^{+0.2}_{-0.2}$	$0.9^{+0.1}_{-0.1}$	$-2.5^{+0.1}_{-0.1}$	$-0.34^{+0.03}_{-0.03}$	–	1	–
PRIMERUDS-69092	34.275448	-5.26442	26.1	$8.3^{+0.3}_{-0.3}$	$-20.4^{+0.1}_{-0.1}$	$9.4^{+0.1}_{-0.1}$	$1.2^{+0.1}_{-0.1}$	$-2.3^{+0.1}_{-0.1}$	$-0.09^{+0.02}_{-0.02}$	–	0	0
PRIMERUDS-69462	34.30558	-5.2638092	26.0	$7.2^{+0.1}_{-0.1}$	$-20.8^{+0.1}_{-0.1}$	$9.2^{+0.1}_{-0.1}$	$1.6^{+0.2}_{-0.2}$	$-1.7^{+0.2}_{-0.2}$	$0.03^{+0.02}_{-0.02}$	–	0	0
PRIMERUDS-70520	34.47213	-5.2609186	27.1	$7.5^{+0.5}_{-0.4}$	$-19.3^{+0.1}_{-0.1}$	$8.9^{+0.2}_{-0.2}$	$0.8^{+0.1}_{-0.1}$	$-2.3^{+0.2}_{-0.2}$	$-0.30^{+0.54}_{-0.54}$	–	0	0
PRIMERUDS-72310	34.422253	-5.2592807	25.7	$7.2^{+0.1}_{-0.1}$	$-20.8^{+0.1}_{-0.1}$	$9.1^{+0.1}_{-0.1}$	$1.6^{+0.1}_{-0.1}$	$-1.9^{+0.1}_{-0.1}$	$-0.07^{+0.03}_{-0.03}$	–	0	0
PRIMERUDS-84176	34.298401	-5.2426572	27.2	$8.7^{+0.3}_{-0.3}$	$-20.0^{+0.1}_{-0.1}$	$8.7^{+0.3}_{-0.3}$	$1.0^{+0.2}_{-0.2}$	$-2.0^{+0.2}_{-0.2}$	$-0.70^{+0.04}_{-0.04}$	–	0	0
PRIMERUDS-84698	34.384274	-5.2413874	26.5	$9.2^{+0.3}_{-0.2}$	$-21.3^{+0.1}_{-0.1}$	$9.2^{+0.2}_{-0.2}$	$1.1^{+0.1}_{-0.1}$	$-2.8^{+0.1}_{-0.1}$	$-0.51^{+0.18}_{-0.18}$	–	0	0
PRIMERUDS-92176	34.407547	-5.2356758	26.7	$7.9^{+0.3}_{-0.3}$	$-19.6^{+0.1}_{-0.1}$	$8.8^{+0.1}_{-0.1}$	$1.0^{+0.1}_{-0.1}$	$-2.5^{+0.1}_{-0.1}$	$-0.23^{+0.04}_{-0.04}$	–	0	0
PRIMERUDS-96524	34.264969	-5.2341166	26.4	$7.5^{+0.3}_{-0.4}$	$-20.9^{+0.1}_{-0.1}$	$8.9^{+0.2}_{-0.2}$	$1.4^{+0.1}_{-0.1}$	$-1.8^{+0.1}_{-0.1}$	$-0.10^{+0.06}_{-0.06}$	–	0	0
PRIMERUDS-97368	34.459652	-5.2315211	27.6	$8.1^{+0.4}_{-0.4}$	$-18.9^{+0.1}_{-0.1}$	$7.6^{+0.1}_{-0.1}$	$0.6^{+0.1}_{-0.1}$	$-2.9^{+0.1}_{-0.1}$	$-0.53^{+0.05}_{-0.05}$	–	0	0
PRIMERUDS-110960	34.3675	-5.2190299	26.3	$8.8^{+0.1}_{-0.1}$	$-21.0^{+0.1}_{-0.1}$	$9.4^{+0.6}_{-0.6}$	$1.2^{+0.1}_{-0.1}$	$-2.2^{+0.1}_{-0.1}$	$-0.49^{+0.02}_{-0.02}$	–	0	0
PRIMERUDS-118212	34.367577	-5.2153816	26.4	$8.7^{+0.3}_{-0.4}$	$-19.2^{+0.1}_{-0.1}$	$8.5^{+0.1}_{-0.1}$	$1.2^{+0.1}_{-0.1}$	$-2.6^{+0.1}_{-0.1}$	$0.15^{+0.04}_{-0.04}$	–	0	0
PRIMERUDS-121593	34.323589	-5.21416	26.9	$8.4^{+0.3}_{-0.3}$	$-20.1^{+0.1}_{-0.1}$	$9.0^{+0.8}_{-0.8}$	$0.9^{+0.1}_{-0.1}$	$-2.2^{+0.1}_{-0.1}$	$-0.35^{+0.09}_{-0.09}$	–	0	0
PRIMERUDS-123434	34.491253	-5.2122388	27.3	$7.2^{+0.2}_{-0.1}$	$-20.0^{+0.1}_{-0.1}$	$8.0^{+0.2}_{-0.2}$	$0.7^{+0.1}_{-0.1}$	$-2.3^{+0.1}_{-0.1}$	$-0.62^{+0.06}_{-0.06}$	–	0	0
PRIMERUDS-132885	34.233913	-5.2100353	26.1	$7.6^{+0.3}_{-0.4}$	$-21.6^{+0.1}_{-0.1}$	$10.0^{+0.1}_{-0.1}$	$1.3^{+0.1}_{-0.1}$	$-2.1^{+0.1}_{-0.1}$	$-0.28^{+0.04}_{-0.04}$	–	0	0
PRIMERUDS-133009	34.233852	-5.2100344	27.0	$7.3^{+0.5}_{-0.3}$	$-21.3^{+0.1}_{-0.1}$	$8.9^{+0.1}_{-0.1}$	$1.5^{+0.1}_{-0.1}$	$-1.4^{+0.1}_{-0.1}$	$-0.94^{+0.04}_{-0.04}$	–	0	1
PRIMERUDS-137776	34.317993	-5.206953	26.8	$7.3^{+0.1}_{-0.1}$	$-19.6^{+0.1}_{-0.1}$	$8.7^{+0.1}_{-0.1}$	$1.1^{+0.1}_{-0.1}$	$-1.8^{+0.1}_{-0.1}$	$-0.53^{+0.03}_{-0.03}$	–	0	0
PRIMERUDS-143983	34.495827	-5.2023988	27.0	$7.4^{+0.1}_{-0.1}$	$-19.5^{+0.1}_{-0.1}$	$7.9^{+0.1}_{-0.1}$	$0.9^{+0.1}_{-0.1}$	$-2.8^{+0.1}_{-0.1}$	$-0.50^{+0.31}_{-0.31}$	–	0	0
PRIMERUDS-146539	34.367455	-5.2022929	26.3	$9.0^{+0.3}_{-0.3}$	$-20.3^{+0.1}_{-0.1}$	$8.6^{+0.3}_{-0.3}$	$1.2^{+0.1}_{-0.1}$	$-2.7^{+0.1}_{-0.2}$	$0.17^{+0.04}_{-0.04}$	–	0	0

Table 5 continued

Table 5 (continued)

ID	R.A.	Decl.	m_{UV}	z^\dagger	M_{UV}	M_*	SFR	β_{UV}	$R_{e,maj}$	[O III]/H β	f_{gal}^*	f_{com}^*
	deg.	deg.	mag		mag	$\log M_\odot$	$\log M_\odot/\text{yr}$		log kpc	log		
PRIMERCOS-1876	150.17801	2.2393584	27.0	$7.5^{+0.1}_{-0.1}$	$-19.1^{+0.1}_{-0.1}$	$7.7^{+0.2}_{-0.2}$	$0.8^{+0.1}_{-0.1}$	$-2.6^{+0.1}_{-0.1}$	$-1.06^{+0.05}_{-0.05}$	–	0	1
PRIMERCOS-4537	150.15474	2.2460606	26.6	$8.1^{+0.3}_{-0.2}$	$-21.3^{+0.1}_{-0.1}$	$8.2^{+0.2}_{-0.2}$	$1.1^{+0.1}_{-0.1}$	$-2.7^{+0.2}_{-0.1}$	$-0.07^{+0.05}_{-0.05}$	–	0	0
PRIMERCOS-5617	150.18694	2.2494292	26.9	$7.3^{+0.1}_{-0.1}$	$-19.5^{+0.1}_{-0.1}$	$8.1^{+0.3}_{-0.3}$	$0.9^{+0.1}_{-0.1}$	$-2.5^{+0.1}_{-0.1}$	$-0.29^{+0.29}_{-0.29}$	–	0	0
PRIMERCOS-8110	150.1423	2.2542021	26.8	$8.8^{+0.3}_{-0.4}$	$-19.5^{+0.1}_{-0.1}$	$8.8^{+0.1}_{-0.1}$	$0.9^{+0.1}_{-0.1}$	$-2.3^{+0.1}_{-0.1}$	$-0.30^{+0.03}_{-0.03}$	–	0	0
PRIMERCOS-10530	150.14932	2.2591827	27.2	$9.0^{+0.3}_{-0.3}$	$-19.9^{+0.1}_{-0.1}$	$9.2^{+0.1}_{-0.1}$	$0.9^{+0.1}_{-0.1}$	$-2.6^{+0.1}_{-0.1}$	$-0.49^{+0.05}_{-0.05}$	–	0	0
PRIMERCOS-12668	150.11729	2.2635334	26.9	$8.2^{+0.3}_{-0.2}$	$-20.0^{+0.1}_{-0.1}$	$8.7^{+0.1}_{-0.1}$	$0.9^{+0.1}_{-0.1}$	$-2.3^{+0.1}_{-0.1}$	$-0.35^{+0.04}_{-0.04}$	–	0	0
PRIMERCOS-21719	150.17093	2.2768395	25.8	$8.8^{+0.4}_{-0.2}$	$-21.3^{+0.1}_{-0.1}$	$8.9^{+0.1}_{-0.1}$	$1.5^{+0.1}_{-0.1}$	$-2.1^{+0.1}_{-0.1}$	$0.08^{+0.03}_{-0.03}$	–	0	0
PRIMERCOS-22886	150.10645	2.2780333	26.6	$7.3^{+0.2}_{-0.2}$	$-19.5^{+0.1}_{-0.1}$	$9.5^{+0.1}_{-0.1}$	$1.1^{+0.2}_{-0.2}$	$-1.9^{+0.1}_{-0.2}$	$-0.22^{+0.03}_{-0.03}$	–	0	0
PRIMERCOS-40689	150.20164	2.3149087	26.7	$8.7^{+0.2}_{-0.2}$	$-20.9^{+0.1}_{-0.1}$	$9.3^{+0.1}_{-0.1}$	$1.0^{+0.1}_{-0.1}$	$-2.7^{+0.1}_{-0.1}$	$-1.02^{+0.06}_{-0.06}$	–	0	1
PRIMERCOS-50439	150.10057	2.3322499	27.0	$7.2^{+0.1}_{-0.1}$	$-19.5^{+0.1}_{-0.1}$	$7.7^{+0.2}_{-0.2}$	$0.7^{+0.1}_{-0.1}$	$-2.7^{+0.2}_{-0.1}$	$-0.31^{+0.49}_{-0.49}$	–	0	0
PRIMERCOS-59070	150.09526	2.3492894	26.5	$8.9^{+0.2}_{-0.3}$	$-19.7^{+0.1}_{-0.1}$	$8.6^{+0.1}_{-0.1}$	$1.2^{+0.1}_{-0.1}$	$-2.1^{+0.1}_{-0.3}$	$-0.17^{+0.04}_{-0.04}$	–	0	0
PRIMERCOS-76099	150.11259	2.3792171	26.9	$7.5^{+0.3}_{-0.2}$	$-19.8^{+0.1}_{-0.1}$	$8.8^{+0.1}_{-0.1}$	$0.9^{+0.1}_{-0.1}$	$-2.2^{+0.1}_{-0.1}$	$-0.35^{+0.04}_{-0.04}$	–	0	0
PRIMERCOS-92684	150.09816	2.412853	25.9	$8.0^{+0.1}_{-0.1}$	$-21.3^{+0.1}_{-0.1}$	$8.3^{+0.1}_{-0.1}$	$1.3^{+0.1}_{-0.1}$	$-2.8^{+0.1}_{-0.1}$	$-1.12^{+0.03}_{-0.03}$	–	0	1
PRIMERCOS-95321	150.17979	2.4195976	26.6	$8.3^{+0.2}_{-0.3}$	$-20.3^{+0.1}_{-0.1}$	$8.5^{+0.3}_{-0.3}$	$1.1^{+0.1}_{-0.1}$	$-2.6^{+0.1}_{-0.1}$	$-0.76^{+0.02}_{-0.02}$	–	0	0
PRIMERCOS-101351	150.11674	2.4329758	27.2	$8.3^{+0.3}_{-0.4}$	$-20.0^{+0.1}_{-0.1}$	$7.9^{+0.1}_{-0.1}$	$0.8^{+0.1}_{-0.1}$	$-3.0^{+0.2}_{-0.1}$	$-0.93^{+0.04}_{-0.04}$	–	0	0
PRIMERCOS-102047	150.2037	2.4356833	26.8	$8.6^{+0.3}_{-0.4}$	$-20.3^{+0.1}_{-0.1}$	$8.4^{+0.3}_{-0.3}$	$0.9^{+0.1}_{-0.1}$	$-2.9^{+0.1}_{-0.1}$	$-0.41^{+0.15}_{-0.15}$	–	0	0
PRIMERCOS-102710	150.14003	2.4360871	26.2	$8.6^{+0.2}_{-0.2}$	$-21.2^{+0.1}_{-0.1}$	$9.1^{+0.1}_{-0.1}$	$1.2^{+0.1}_{-0.1}$	$-2.2^{+0.1}_{-0.1}$	$-0.69^{+0.02}_{-0.02}$	–	0	0
PRIMERCOS-103947	150.10559	2.437932	26.6	$8.6^{+0.5}_{-0.3}$	$-20.4^{+0.1}_{-0.1}$	$8.4^{+0.1}_{-0.1}$	$1.1^{+0.1}_{-0.1}$	$-2.3^{+0.1}_{-0.1}$	$-0.38^{+0.18}_{-0.18}$	–	0	0
PRIMERCOS-111899	150.10913	2.4536574	26.1	$9.3^{+0.1}_{-0.1}$	$-21.4^{+0.1}_{-0.1}$	$9.0^{+0.2}_{-0.2}$	$1.4^{+0.1}_{-0.1}$	$-2.1^{+0.1}_{-0.1}$	$-0.12^{+0.04}_{-0.04}$	–	0	0
PRIMERCOS-113554	150.19943	2.4583545	26.3	$7.3^{+0.1}_{-0.1}$	$-20.3^{+0.1}_{-0.1}$	$8.7^{+0.1}_{-0.1}$	$1.2^{+0.1}_{-0.1}$	$-2.1^{+0.1}_{-0.1}$	$-0.35^{+0.02}_{-0.02}$	–	0	0
PRIMERCOS-119614	150.13	2.4686878	26.6	$8.9^{+0.3}_{-0.2}$	$-19.5^{+0.1}_{-0.1}$	$8.4^{+0.1}_{-0.1}$	$1.1^{+0.1}_{-0.1}$	$-2.5^{+0.1}_{-0.1}$	$-0.24^{+0.03}_{-0.03}$	–	0	0
PRIMERCOS-122002	150.13895	2.4743896	26.9	$7.3^{+2.5}_{-0.2}$	$-19.0^{+0.1}_{-0.1}$	$8.4^{+0.3}_{-0.3}$	$0.8^{+0.2}_{-0.2}$	$-2.0^{+0.2}_{-0.2}$	$-0.21^{+0.03}_{-0.03}$	–	0	0
PRIMERCOS-122961	150.16527	2.4770103	26.8	$7.2^{+0.1}_{-0.1}$	$-20.1^{+0.1}_{-0.1}$	$8.9^{+0.2}_{-0.2}$	$1.1^{+0.2}_{-0.2}$	$-1.9^{+0.3}_{-0.2}$	$-0.21^{+0.04}_{-0.04}$	–	0	0
PRIMERCOS-124364	150.13078	2.4806907	25.6	$7.7^{+0.3}_{-0.6}$	$-21.6^{+0.1}_{-0.1}$	$9.1^{+0.1}_{-0.1}$	$1.7^{+0.1}_{-0.1}$	$-1.9^{+0.1}_{-0.1}$	$0.12^{+0.03}_{-0.03}$	–	0	0
JADESGDS-788	53.157093	-27.837086	26.9	$8.0^{+0.2}_{-0.2}$	$-20.1^{+0.1}_{-0.1}$	$9.5^{+0.1}_{-0.1}$	$0.8^{+0.1}_{-0.1}$	$-2.4^{+0.1}_{-0.1}$	$0.09^{+0.03}_{-0.03}$	–	1	–
JADESGDS-1337	53.158615	-27.834078	27.9	$8.9^{+0.1}_{-0.1}$	$-20.5^{+0.1}_{-0.1}$	$8.2^{+0.2}_{-0.2}$	$0.3^{+0.1}_{-0.1}$	$-2.5^{+0.1}_{-0.1}$	$-1.15^{+0.11}_{-0.11}$	–	0	1
JADESGDS-2304	53.182175	-27.829906	28.8	$8.9^{+0.2}_{-0.2}$	$-18.4^{+0.1}_{-0.1}$	$8.2^{+0.7}_{-0.7}$	$0.2^{+0.1}_{-0.1}$	$-2.8^{+0.1}_{-0.1}$	$-0.98^{+0.04}_{-0.04}$	–	0	1
JADESGDS-3078	53.183949	-27.827396	29.0	$7.4^{+0.2}_{-0.2}$	$-18.8^{+0.1}_{-0.1}$	$7.7^{+0.2}_{-0.2}$	$0.0^{+0.1}_{-0.1}$	$-2.4^{+0.1}_{-0.1}$	$-0.53^{+0.04}_{-0.04}$	–	0	0
JADESGDS-4153	53.177311	-27.824068	29.0	$8.9^{+0.3}_{-0.4}$	$-17.9^{+0.1}_{-0.1}$	$8.5^{+0.1}_{-0.1}$	$0.1^{+0.1}_{-0.1}$	$-2.6^{+0.1}_{-0.1}$	$-0.42^{+0.04}_{-0.04}$	–	0	0
JADESGDS-4667	53.145905	-27.822794	29.0	$9.0^{+0.2}_{-0.2}$	$-19.3^{+0.1}_{-0.1}$	$8.2^{+0.2}_{-0.2}$	$0.5^{+0.1}_{-0.1}$	$-1.8^{+0.1}_{-0.1}$	$-0.97^{+0.07}_{-0.07}$	–	0	1
JADESGDS-4854	53.145844	-27.822742	26.7	$8.2^{+0.1}_{-0.1}$	$-20.1^{+0.1}_{-0.1}$	$9.0^{+0.2}_{-0.2}$	$1.3^{+0.1}_{-0.1}$	$-1.9^{+0.1}_{-0.1}$	$-0.01^{+0.06}_{-0.06}$	–	0	0
JADESGDS-5100	53.165787	-27.821783	29.1	$7.2^{+0.1}_{-0.1}$	$-18.5^{+0.1}_{-0.1}$	$7.4^{+0.2}_{-0.2}$	$-0.1^{+0.1}_{-0.1}$	$-2.3^{+0.1}_{-0.1}$	$-0.90^{+0.04}_{-0.04}$	–	0	1
JADESGDS-5123	53.186321	-27.821741	28.5	$7.5^{+0.1}_{-0.2}$	$-18.8^{+0.1}_{-0.1}$	$7.7^{+0.3}_{-0.3}$	$0.2^{+0.1}_{-0.1}$	$-2.6^{+0.1}_{-0.1}$	$-0.46^{+0.17}_{-0.17}$	–	0	0
JADESGDS-6492	53.187363	-27.818476	29.0	$8.8^{+0.2}_{-0.3}$	$-17.9^{+0.1}_{-0.1}$	$8.4^{+0.1}_{-0.1}$	$0.1^{+0.1}_{-0.1}$	$-2.6^{+0.1}_{-0.1}$	$-0.59^{+0.04}_{-0.04}$	–	0	0
JADESGDS-6834	53.1768	-27.817759	28.1	$8.8^{+0.1}_{-0.1}$	$-18.9^{+0.1}_{-0.1}$	$8.5^{+0.1}_{-0.1}$	$0.5^{+0.1}_{-0.1}$	$-2.5^{+0.1}_{-0.1}$	$-0.41^{+0.02}_{-0.02}$	–	0	0
JADESGDS-7015	53.176029	-27.817396	28.7	$10.7^{+0.3}_{-1.4}$	$-18.5^{+0.1}_{-0.1}$	$9.3^{+0.1}_{-0.1}$	$0.6^{+0.1}_{-0.1}$	$-1.9^{+0.1}_{-0.1}$	$-0.56^{+0.12}_{-0.12}$	–	0	0
JADESGDS-9528	53.167141	-27.812428	27.9	$7.4^{+0.1}_{-0.1}$	$-19.0^{+0.1}_{-0.1}$	$8.3^{+0.1}_{-0.1}$	$0.5^{+0.1}_{-0.1}$	$-2.2^{+0.1}_{-0.1}$	$-0.23^{+0.02}_{-0.02}$	–	0	0
JADESGDS-12274	53.167358	-27.807507	28.1	9.69	$-19.4^{+0.1}_{-0.1}$	$8.5^{+0.1}_{-0.1}$	$0.5^{+0.1}_{-0.1}$	$-2.3^{+0.1}_{-0.1}$	$-0.81^{+0.02}_{-0.02}$	–	0	0
JADESGDS-14022	53.144043	-27.804459	28.7	$8.9^{+0.2}_{-0.2}$	$-18.5^{+0.1}_{-0.1}$	$7.6^{+0.1}_{-0.1}$	$0.3^{+0.1}_{-0.1}$	$-2.1^{+0.1}_{-0.1}$	$-0.72^{+0.12}_{-0.12}$	–	0	0
JADESGDS-15413	53.164467	-27.802185	28.6	8.47	$-18.2^{+0.1}_{-0.1}$	$8.6^{+0.5}_{-0.5}$	$0.4^{+0.2}_{-0.2}$	$-2.0^{+0.2}_{-0.2}$	$-1.14^{+0.06}_{-0.06}$	0.8 ± 0.2	0	1
JADESGDS-15571	53.152836	-27.801945	28.8	7.26	$-17.6^{+0.1}_{-0.1}$	$8.6^{+0.1}_{-0.1}$	$0.1^{+0.1}_{-0.1}$	$-2.3^{+0.2}_{-0.2}$	$-0.50^{+0.03}_{-0.03}$	–	0	0
JADESGDS-15668	53.155083	-27.801775	27.9	7.30	$-18.6^{+0.1}_{-0.1}$	$8.8^{+0.1}_{-0.1}$	$0.5^{+0.1}_{-0.1}$	$-2.2^{+0.1}_{-0.1}$	$-0.41^{+0.02}_{-0.02}$	–	0	0
JADESGDS-15761	53.193794	-27.801634	28.4	$7.5^{+0.2}_{-0.2}$	$-18.8^{+0.1}_{-0.1}$	$8.0^{+0.1}_{-0.1}$	$0.3^{+0.1}_{-0.1}$	$-2.5^{+0.1}_{-0.1}$	$-1.01^{+0.03}_{-0.03}$	–	0	1
JADESGDS-16719	53.183937	-27.799994	27.7	$7.4^{+0.1}_{-0.1}$	$-19.2^{+0.1}_{-0.1}$	$8.2^{+0.1}_{-0.1}$	$0.5^{+0.1}_{-0.1}$	$-2.3^{+0.1}_{-0.1}$	$-0.54^{+0.02}_{-0.02}$	–	0	0
JADESGDS-17976	53.184048	-27.797829	29.0	$7.3^{+0.1}_{-0.1}$	$-17.9^{+0.1}_{-0.1}$	$7.4^{+0.3}_{-0.3}$	$0.0^{+0.1}_{-0.1}$	$-2.3^{+0.1}_{-0.1}$	$-0.86^{+0.04}_{-0.04}$	–	0	0

Table 5 continued

Table 5 (continued)

ID	R.A.	Decl.	m_{UV}	z^\dagger	M_{UV}	M_*	SFR	β_{UV}	$R_{e,maj}$	[O III]/H β	f_{gal}^*	f_{com}^*
	deg.	deg.	mag		mag	log M_\odot	log M_\odot/yr		log kpc	log		
JADESGDS-18265	53.187874	-27.797451	28.5	$8.4^{+0.1}_{-0.1}$	$-18.8^{+0.1}_{-0.1}$	$8.9^{+0.1}_{-0.1}$	$0.3^{+0.1}_{-0.1}$	$-2.2^{+0.1}_{-0.1}$	$-0.48^{+0.03}_{-0.03}$	–	0	0
JADESGDS-18325	53.190781	-27.797283	29.0	$7.4^{+0.1}_{-0.3}$	$-17.4^{+0.1}_{-0.1}$	$8.0^{+0.5}_{-0.5}$	$0.0^{+0.1}_{-0.1}$	$-2.5^{+0.2}_{-0.1}$	$-0.38^{+0.03}_{-0.03}$	–	0	0
JADESGDS-18428	53.191059	-27.797318	27.7	$7.3^{+0.1}_{-0.1}$	$-18.9^{+0.1}_{-0.1}$	$8.3^{+0.1}_{-0.1}$	$0.8^{+0.1}_{-0.1}$	$-1.8^{+0.1}_{-0.1}$	$-0.35^{+0.01}_{-0.01}$	–	0	0
JADESGDS-18917	53.127213	-27.796421	28.3	$8.6^{+0.1}_{-0.1}$	$-19.1^{+0.1}_{-0.1}$	$8.4^{+0.3}_{-0.3}$	$0.4^{+0.1}_{-0.1}$	$-2.7^{+0.1}_{-0.1}$	$-0.56^{+0.15}_{-0.15}$	–	0	0
JADESGDS-19434	53.186314	-27.795614	28.3	$7.3^{+0.2}_{-0.2}$	$-18.8^{+0.1}_{-0.1}$	$9.0^{+0.1}_{-0.1}$	$0.4^{+0.1}_{-0.1}$	$-2.1^{+0.1}_{-0.1}$	$-0.71^{+0.02}_{-0.02}$	–	0	0
JADESGDS-20632	53.183746	-27.793705	29.0	$7.3^{+0.1}_{-0.1}$	$-18.0^{+0.1}_{-0.1}$	$7.3^{+0.2}_{-0.2}$	$-0.1^{+0.1}_{-0.1}$	$-2.4^{+0.1}_{-0.1}$	$-0.89^{+0.04}_{-0.04}$	–	0	0
JADESGDS-20758	53.183754	-27.793894	27.0	$7.2^{+0.1}_{-0.1}$	$-19.0^{+0.1}_{-0.1}$	$8.3^{+0.1}_{-0.1}$	$0.9^{+0.1}_{-0.1}$	$-1.6^{+0.1}_{-0.1}$	$0.31^{+0.02}_{-0.02}$	–	1	–
JADESGDS-21126	53.149609	-27.792845	26.0	$8.1^{+0.2}_{-0.4}$	$-19.2^{+0.1}_{-0.1}$	$9.1^{+0.1}_{-0.1}$	$0.5^{+0.1}_{-0.1}$	$-2.2^{+0.1}_{-0.1}$	$0.88^{+0.22}_{-0.22}$	–	1	–
JADESGDS-21192	53.115772	-27.792681	29.2	$7.9^{+0.3}_{-0.3}$	$-18.8^{+0.1}_{-0.1}$	$7.5^{+0.1}_{-0.1}$	$0.1^{+0.1}_{-0.1}$	$-2.1^{+0.1}_{-0.1}$	$-0.91^{+0.05}_{-0.05}$	–	0	0
JADESGDS-23180	53.187042	-27.789448	27.2	$7.9^{+0.2}_{-0.2}$	$-20.4^{+0.1}_{-0.1}$	$8.6^{+0.1}_{-0.1}$	$0.8^{+0.1}_{-0.1}$	$-2.4^{+0.1}_{-0.1}$	$-0.15^{+0.02}_{-0.02}$	–	0	0
JADESGDS-23858	53.149384	-27.788181	28.6	$7.3^{+0.1}_{-0.1}$	$-18.5^{+0.1}_{-0.1}$	$7.5^{+0.2}_{-0.2}$	$0.2^{+0.1}_{-0.1}$	$-2.4^{+0.1}_{-0.1}$	$-1.10^{+0.36}_{-0.36}$	–	1	–
JADESGDS-23946	53.164822	-27.788261	27.1	$7.4^{+0.1}_{-0.1}$	$-19.7^{+0.1}_{-0.1}$	$8.0^{+0.1}_{-0.1}$	$0.8^{+0.1}_{-0.1}$	$-2.1^{+0.1}_{-0.1}$	$-0.08^{+0.03}_{-0.03}$	–	1	–
JADESGDS-23970	53.164684	-27.788233	27.7	$7.3^{+0.1}_{-0.1}$	$-19.3^{+0.1}_{-0.1}$	$9.3^{+0.1}_{-0.1}$	$1.1^{+0.1}_{-0.1}$	$-1.6^{+0.1}_{-0.1}$	$0.11^{+0.01}_{-0.01}$	–	1	–
JADESGDS-25131	53.126896	-27.78615	28.9	$7.2^{+0.1}_{-0.1}$	$-17.7^{+0.1}_{-0.1}$	$8.6^{+0.3}_{-0.3}$	$1.0^{+0.2}_{-0.2}$	$-1.0^{+0.3}_{-0.2}$	$-1.09^{+0.33}_{-0.33}$	–	0	1
JADESGDS-25734	53.161705	-27.785393	26.8	$7.4^{+0.1}_{-0.1}$	$-20.0^{+0.1}_{-0.1}$	$8.7^{+0.1}_{-0.1}$	$1.3^{+0.1}_{-0.1}$	$-1.7^{+0.1}_{-0.1}$	$-0.32^{+0.01}_{-0.01}$	–	0	0
JADESGDS-26008	53.164146	-27.784525	29.1	$8.0^{+0.3}_{-0.3}$	$-17.8^{+0.1}_{-0.1}$	$8.1^{+0.5}_{-0.5}$	$0.3^{+0.1}_{-0.1}$	$-2.0^{+0.2}_{-0.1}$	$-0.50^{+0.14}_{-0.14}$	–	0	0
JADESGDS-27630	53.13805	-27.781866	28.4	$7.4^{+0.1}_{-0.1}$	$-18.1^{+0.1}_{-0.1}$	$7.5^{+0.1}_{-0.1}$	$0.2^{+0.1}_{-0.1}$	$-2.4^{+0.1}_{-0.1}$	$-0.39^{+0.15}_{-0.15}$	–	0	0
JADESGDS-27714	53.200645	-27.781652	29.2	$7.2^{+0.2}_{-0.1}$	$-17.9^{+0.1}_{-0.1}$	$6.8^{+0.2}_{-0.2}$	$-0.2^{+0.1}_{-0.1}$	$-2.7^{+0.2}_{-0.1}$	$-0.47^{+0.08}_{-0.08}$	–	0	0
JADESGDS-29310	53.209885	-27.779276	27.7	$8.4^{+0.1}_{-0.1}$	$-19.7^{+0.1}_{-0.1}$	$8.7^{+0.2}_{-0.2}$	$0.6^{+0.1}_{-0.1}$	$-2.4^{+0.1}_{-0.1}$	$-0.66^{+0.02}_{-0.02}$	–	0	0
JADESGDS-29365	53.186237	-27.779055	29.5	$7.5^{+0.2}_{-0.2}$	$-18.2^{+0.1}_{-0.1}$	$8.2^{+0.1}_{-0.1}$	$-0.1^{+0.1}_{-0.1}$	$-2.2^{+0.1}_{-0.1}$	$-1.10^{+0.26}_{-0.26}$	–	0	1
JADESGDS-29377	53.186291	-27.779028	27.2	$7.4^{+0.1}_{-0.1}$	$-18.8^{+0.1}_{-0.1}$	$8.4^{+0.1}_{-0.1}$	$0.7^{+0.1}_{-0.1}$	$-2.2^{+0.1}_{-0.1}$	$-0.09^{+0.01}_{-0.01}$	–	0	0
JADESGDS-31104	53.17868	-27.77632	28.2	$7.5^{+0.2}_{-0.3}$	$-19.4^{+0.1}_{-0.1}$	$8.5^{+0.1}_{-0.1}$	$0.6^{+0.1}_{-0.1}$	$-2.0^{+0.1}_{-0.1}$	$-0.42^{+0.37}_{-0.37}$	–	0	0
JADESGDS-31373	53.207279	-27.775711	28.6	$8.5^{+0.1}_{-0.2}$	$-18.5^{+0.1}_{-0.1}$	$7.7^{+0.2}_{-0.2}$	$0.3^{+0.1}_{-0.1}$	$-2.6^{+0.1}_{-0.1}$	$-0.89^{+0.08}_{-0.08}$	–	0	0
JADESGDS-32140	53.17976	-27.774647	27.6	$7.3^{+0.1}_{-0.1}$	$-19.2^{+0.1}_{-0.1}$	$8.0^{+0.1}_{-0.1}$	$0.7^{+0.1}_{-0.1}$	$-2.1^{+0.1}_{-0.1}$	$-0.38^{+0.01}_{-0.01}$	–	0	0
JADESGDS-32166	53.179539	-27.774437	28.6	$7.3^{+0.2}_{-0.1}$	$-17.8^{+0.1}_{-0.1}$	$8.3^{+0.1}_{-0.1}$	$0.4^{+0.1}_{-0.1}$	$-1.9^{+0.2}_{-0.1}$	$-0.32^{+0.04}_{-0.04}$	–	0	0
JADESGDS-32270	53.130047	-27.774494	28.2	$7.3^{+0.1}_{-0.1}$	$-20.6^{+0.1}_{-0.1}$	$8.0^{+0.1}_{-0.1}$	$0.4^{+0.1}_{-0.1}$	$-2.3^{+0.1}_{-0.1}$	$-1.10^{+0.04}_{-0.04}$	–	0	1
JADESGDS-32432	53.179539	-27.773949	29.0	$7.3^{+0.1}_{-0.1}$	$-18.4^{+0.1}_{-0.1}$	$7.2^{+0.1}_{-0.1}$	$0.0^{+0.1}_{-0.1}$	$-2.4^{+0.1}_{-0.1}$	$-0.74^{+0.04}_{-0.04}$	–	0	0
JADESGDS-32832	53.185356	-27.773184	28.2	$7.4^{+0.1}_{-0.1}$	$-18.7^{+0.1}_{-0.1}$	$7.5^{+0.1}_{-0.1}$	$0.3^{+0.1}_{-0.1}$	$-2.5^{+0.1}_{-0.1}$	$-0.48^{+0.02}_{-0.02}$	–	0	0
JADESGDS-33025	53.140919	-27.772795	28.8	$8.9^{+0.1}_{-0.1}$	$-18.2^{+0.1}_{-0.1}$	$7.5^{+0.2}_{-0.2}$	$0.0^{+0.1}_{-0.1}$	$-2.4^{+0.1}_{-0.1}$	$-1.15^{+0.13}_{-0.13}$	–	0	1
JADESGDS-33585	53.195766	-27.772051	27.7	$7.3^{+0.2}_{-0.1}$	$-18.8^{+0.1}_{-0.1}$	$8.2^{+0.1}_{-0.1}$	$0.5^{+0.1}_{-0.1}$	$-2.2^{+0.1}_{-0.1}$	$-0.20^{+0.03}_{-0.03}$	–	0	0
JADESGDS-33635	53.18224	-27.771826	28.9	$7.3^{+0.1}_{-0.1}$	$-17.6^{+0.1}_{-0.1}$	$7.4^{+0.2}_{-0.2}$	$0.0^{+0.1}_{-0.1}$	$-2.3^{+0.1}_{-0.1}$	$-0.85^{+0.04}_{-0.04}$	–	0	0
JADESGDS-33892	53.180119	-27.771437	28.2	$7.3^{+0.1}_{-0.1}$	$-18.8^{+0.1}_{-0.1}$	$8.0^{+0.1}_{-0.1}$	$0.3^{+0.1}_{-0.1}$	$-2.2^{+0.1}_{-0.1}$	$-0.79^{+0.02}_{-0.02}$	–	0	0
JADESGDS-34398	53.1768	-27.770538	29.1	$7.2^{+0.3}_{-0.2}$	$-18.7^{+0.1}_{-0.1}$	$8.1^{+0.1}_{-0.1}$	$0.0^{+0.1}_{-0.1}$	$-2.6^{+0.2}_{-0.2}$	$-1.07^{+0.13}_{-0.13}$	–	0	1
JADESGDS-34439	53.211437	-27.770441	28.6	$8.1^{+0.2}_{-0.3}$	$-18.6^{+0.1}_{-0.1}$	$8.5^{+0.1}_{-0.1}$	$-0.1^{+0.1}_{-0.1}$	$-2.7^{+0.1}_{-0.1}$	$-0.76^{+0.07}_{-0.07}$	–	0	0
JADESGDS-34608	53.183548	-27.770182	28.0	$8.8^{+0.1}_{-0.1}$	$-18.9^{+0.1}_{-0.1}$	$7.9^{+0.1}_{-0.1}$	$0.6^{+0.1}_{-0.1}$	$-2.6^{+0.1}_{-0.1}$	$-0.83^{+0.07}_{-0.07}$	–	0	0
JADESGDS-34694	53.193115	-27.770044	28.5	$7.3^{+0.2}_{-0.1}$	$-18.0^{+0.1}_{-0.1}$	$7.9^{+0.2}_{-0.2}$	$0.2^{+0.1}_{-0.1}$	$-2.1^{+0.1}_{-0.1}$	$-0.51^{+0.02}_{-0.02}$	–	0	0
JADESGDS-35079	53.181484	-27.769501	28.2	$7.4^{+0.1}_{-0.1}$	$-18.5^{+0.1}_{-0.1}$	$7.3^{+0.1}_{-0.1}$	$0.3^{+0.1}_{-0.1}$	$-2.7^{+0.1}_{-0.1}$	$-0.21^{+0.05}_{-0.05}$	–	0	0
JADESGDS-35654	53.194141	-27.768377	28.9	$7.4^{+0.1}_{-0.1}$	$-17.9^{+0.1}_{-0.1}$	$7.0^{+0.2}_{-0.2}$	$0.0^{+0.1}_{-0.1}$	$-2.6^{+0.1}_{-0.1}$	$-0.34^{+0.04}_{-0.04}$	–	0	0
JADESGDS-35828	53.206631	-27.7682	28.1	$7.6^{+0.3}_{-0.3}$	$-19.1^{+0.1}_{-0.1}$	$9.2^{+0.1}_{-0.1}$	$0.6^{+0.1}_{-0.1}$	$-2.0^{+0.1}_{-0.1}$	$-0.25^{+0.03}_{-0.03}$	–	0	0
JADESGDS-35921	53.190769	-27.767883	28.8	$7.7^{+0.2}_{-0.4}$	$-17.9^{+0.1}_{-0.1}$	$8.8^{+0.1}_{-0.1}$	$0.2^{+0.1}_{-0.1}$	$-2.1^{+0.1}_{-0.1}$	$-1.11^{+0.08}_{-0.08}$	–	0	1
JADESGDS-36297	53.156826	-27.76716	28.3	7.98	$-18.7^{+0.1}_{-0.1}$	$7.7^{+0.2}_{-0.2}$	$0.3^{+0.1}_{-0.1}$	$-2.4^{+0.1}_{-0.1}$	$-0.60^{+0.14}_{-0.14}$	0.8 ± 0.1	0	0
JADESGDS-36509	53.157509	-27.766775	28.1	$8.4^{+0.1}_{-0.2}$	$-18.9^{+0.1}_{-0.1}$	$7.9^{+0.1}_{-0.1}$	$0.6^{+0.1}_{-0.1}$	$-2.1^{+0.1}_{-0.1}$	$-0.48^{+0.53}_{-0.53}$	–	0	0
JADESGDS-36697	53.192078	-27.766617	27.6	$7.7^{+0.2}_{-0.2}$	$-19.4^{+0.1}_{-0.1}$	$8.6^{+0.1}_{-0.1}$	$0.8^{+0.1}_{-0.1}$	$-2.0^{+0.1}_{-0.1}$	$-0.06^{+0.02}_{-0.02}$	–	0	0
JADESGDS-36968	53.1968	-27.765921	28.7	$8.0^{+0.3}_{-0.3}$	$-17.8^{+0.1}_{-0.1}$	$8.0^{+0.2}_{-0.2}$	$0.1^{+0.1}_{-0.1}$	$-2.5^{+0.1}_{-0.2}$	$-0.43^{+0.03}_{-0.03}$	–	0	0
JADESGDS-37559	53.158909	-27.765074	28.2	$8.8^{+0.1}_{-0.1}$	$-19.4^{+0.1}_{-0.1}$	$7.6^{+0.1}_{-0.1}$	$0.5^{+0.1}_{-0.1}$	$-2.5^{+0.1}_{-0.1}$	$-0.80^{+0.02}_{-0.02}$	–	0	0

Table 5 continued

Table 5 (continued)

ID	R.A.	Decl.	m_{UV}	z^\dagger	M_{UV}	M_*	SFR	β_{UV}	$R_{e,maj}$	[O III]/H β	f_{gal}^*	f_{com}^*
	deg.	deg.	mag		mag	$\log M_\odot$	$\log M_\odot/\text{yr}$		log kpc	log		
JADESGDS-38799	53.198296	-27.762787	27.6	$7.8^{+0.2}_{-0.3}$	$-19.5^{+0.1}_{-0.1}$	$9.0^{+0.1}_{-0.1}$	$0.7^{+0.1}_{-0.1}$	$-2.1^{+0.1}_{-0.1}$	$-0.61^{+0.02}_{-0.02}$	–	0	0
JADESGDS-42098	53.168079	-27.75688	28.3	$7.3^{+0.1}_{-0.1}$	$-19.2^{+0.1}_{-0.1}$	$8.1^{+0.1}_{-0.1}$	$0.3^{+0.1}_{-0.1}$	$-2.2^{+0.1}_{-0.1}$	$-0.93^{+0.02}_{-0.02}$	–	0	1
JADESGDS-42974	53.150093	-27.755131	28.1	$8.6^{+0.1}_{-0.2}$	$-19.9^{+0.1}_{-0.1}$	$8.5^{+0.1}_{-0.1}$	$0.4^{+0.1}_{-0.1}$	$-2.5^{+0.1}_{-0.1}$	$-0.71^{+0.10}_{-0.10}$	–	0	0
JADESGDS-43409	53.168652	-27.754108	28.6	$7.4^{+0.4}_{-0.3}$	$-17.7^{+0.1}_{-0.1}$	$7.6^{+0.2}_{-0.2}$	$0.2^{+0.2}_{-0.2}$	$-2.1^{+0.1}_{-0.2}$	$-0.20^{+0.03}_{-0.03}$	–	0	0
JADESGDS-43422	53.156612	-27.754284	28.3	$7.4^{+0.3}_{-0.3}$	$-18.4^{+0.1}_{-0.1}$	$8.6^{+0.1}_{-0.1}$	$0.4^{+0.1}_{-0.1}$	$-2.0^{+0.1}_{-0.1}$	$0.01^{+0.22}_{-0.22}$	–	0	0
JADESGDS-44487	53.188103	-27.751987	28.2	$7.3^{+0.1}_{-0.1}$	$-18.5^{+0.1}_{-0.1}$	$8.0^{+0.1}_{-0.1}$	$0.4^{+0.1}_{-0.1}$	$-2.1^{+0.1}_{-0.1}$	$-0.74^{+0.02}_{-0.02}$	–	0	0
JADESGDS-44871	53.178692	-27.751266	26.9	$7.7^{+0.2}_{-0.3}$	$-20.6^{+0.1}_{-0.1}$	$9.0^{+0.1}_{-0.1}$	$1.1^{+0.1}_{-0.1}$	$-2.0^{+0.1}_{-0.1}$	$-0.41^{+0.07}_{-0.07}$	–	0	0
JADESGDS-45155	53.149796	-27.750534	29.0	$7.3^{+0.1}_{-0.1}$	$-18.0^{+0.1}_{-0.1}$	$7.4^{+0.2}_{-0.2}$	$0.0^{+0.1}_{-0.1}$	$-2.5^{+0.1}_{-0.1}$	$-0.77^{+0.03}_{-0.03}$	–	0	0
JADESGDS-47089	53.18932	-27.745836	28.9	$7.2^{+0.1}_{-0.1}$	$-18.0^{+0.1}_{-0.1}$	$7.6^{+0.1}_{-0.1}$	$0.0^{+0.1}_{-0.1}$	$-2.3^{+0.1}_{-0.1}$	$-0.94^{+0.04}_{-0.04}$	–	0	1
JADESGDS-47285	53.179623	-27.745205	28.6	$7.4^{+0.2}_{-0.2}$	$-17.9^{+0.1}_{-0.1}$	$8.2^{+0.4}_{-0.4}$	$0.1^{+0.1}_{-0.1}$	$-2.2^{+0.2}_{-0.2}$	$-0.35^{+0.04}_{-0.04}$	–	0	0
JADESGDS-47520	53.17057	-27.744678	29.3	$7.4^{+0.4}_{-0.4}$	$-18.6^{+0.1}_{-0.1}$	$8.2^{+0.2}_{-0.2}$	$0.2^{+0.1}_{-0.1}$	$-1.9^{+0.2}_{-0.2}$	$-0.48^{+0.10}_{-0.10}$	–	0	0
JADESGDS-47564	53.178589	-27.74456	28.6	$7.3^{+0.1}_{-0.1}$	$-18.1^{+0.1}_{-0.1}$	$7.5^{+0.1}_{-0.1}$	$0.1^{+0.1}_{-0.1}$	$-2.4^{+0.1}_{-0.1}$	$-0.70^{+0.07}_{-0.07}$	–	0	0
JADESGDS-47602	53.177204	-27.744425	28.1	$7.3^{+0.2}_{-0.2}$	$-18.4^{+0.1}_{-0.1}$	$8.1^{+0.1}_{-0.1}$	$0.4^{+0.1}_{-0.1}$	$-2.1^{+0.1}_{-0.1}$	$-0.34^{+0.02}_{-0.02}$	–	0	0
JADESGDS-48793	53.171856	-27.7407	28.3	$7.2^{+0.2}_{-0.1}$	$-18.4^{+0.1}_{-0.1}$	$8.0^{+0.1}_{-0.1}$	$0.3^{+0.1}_{-0.1}$	$-2.4^{+0.1}_{-0.1}$	$-0.70^{+0.04}_{-0.04}$	–	0	0
JADESGDS-48873	53.178612	-27.740423	28.8	$8.9^{+0.2}_{-0.2}$	$-18.4^{+0.1}_{-0.1}$	$8.4^{+0.3}_{-0.3}$	$0.2^{+0.1}_{-0.1}$	$-2.2^{+0.2}_{-0.1}$	$-0.52^{+0.33}_{-0.33}$	–	0	0
JADESGDS-49208	53.17572	-27.739233	27.3	$7.6^{+0.3}_{-0.3}$	$-18.8^{+0.1}_{-0.1}$	$8.7^{+0.1}_{-0.1}$	$0.8^{+0.1}_{-0.1}$	$-2.1^{+0.1}_{-0.1}$	$0.03^{+0.48}_{-0.48}$	–	0	0
JADESGDS-49452	53.169575	-27.73806	26.8	$7.3^{+0.1}_{-0.1}$	$-20.1^{+0.1}_{-0.1}$	$8.4^{+0.1}_{-0.1}$	$0.9^{+0.1}_{-0.1}$	$-2.3^{+0.1}_{-0.1}$	$-0.63^{+0.01}_{-0.01}$	–	0	0
JADESGDS-49900	53.167809	-27.736139	27.5	$7.3^{+0.1}_{-0.1}$	$-19.3^{+0.1}_{-0.1}$	$8.5^{+0.1}_{-0.1}$	$0.8^{+0.1}_{-0.1}$	$-1.9^{+0.1}_{-0.1}$	$-0.17^{+0.01}_{-0.01}$	–	1	–
JADESGDS-49932	53.167774	-27.736191	28.1	$7.6^{+0.3}_{-0.3}$	$-20.2^{+0.1}_{-0.1}$	$8.3^{+0.1}_{-0.1}$	$0.4^{+0.1}_{-0.1}$	$-2.2^{+0.1}_{-0.1}$	$-0.76^{+0.02}_{-0.02}$	–	0	0
JADESGDS-50409	53.163158	-27.733881	28.8	$8.6^{+0.2}_{-0.3}$	$-18.2^{+0.1}_{-0.1}$	$8.3^{+0.8}_{-0.8}$	$0.2^{+0.1}_{-0.1}$	$-2.7^{+0.1}_{-0.1}$	$-1.14^{+0.16}_{-0.16}$	–	0	1
PAR1199-5945	177.44745	22.505428	27.9	$7.4^{+0.1}_{-0.1}$	$-18.8^{+0.1}_{-0.1}$	$7.5^{+0.2}_{-0.2}$	$0.5^{+0.1}_{-0.1}$	$-2.6^{+0.1}_{-0.1}$	$-0.76^{+0.03}_{-0.03}$	–	0	0
PAR1199-8789	177.46202	22.520525	26.0	$7.3^{+0.1}_{-0.1}$	$-20.7^{+0.1}_{-0.1}$	$8.6^{+0.1}_{-0.1}$	$1.3^{+0.1}_{-0.1}$	$-2.0^{+0.1}_{-0.1}$	$0.31^{+0.01}_{-0.01}$	–	1	–
PAR1199-9402	177.46661	22.524611	28.0	$7.3^{+0.1}_{-0.1}$	$-19.3^{+0.1}_{-0.1}$	$7.7^{+0.2}_{-0.2}$	$0.4^{+0.1}_{-0.1}$	$-2.5^{+0.1}_{-0.1}$	$-0.78^{+0.03}_{-0.03}$	–	0	0
PAR1199-12617	177.44411	22.474209	28.0	$7.3^{+0.1}_{-0.1}$	$-18.8^{+0.1}_{-0.1}$	$8.1^{+0.3}_{-0.3}$	$0.4^{+0.1}_{-0.1}$	$-2.1^{+0.2}_{-0.1}$	$-0.56^{+0.03}_{-0.03}$	–	0	0
PAR1199-16706	177.4827	22.519428	27.7	$7.3^{+0.2}_{-0.1}$	$-18.5^{+0.1}_{-0.1}$	$8.4^{+0.1}_{-0.1}$	$0.7^{+0.1}_{-0.1}$	$-1.9^{+0.2}_{-0.1}$	$-0.21^{+0.03}_{-0.03}$	–	0	0
PAR1199-18327	177.45447	22.472237	27.9	$7.3^{+0.1}_{-0.1}$	$-18.6^{+0.1}_{-0.1}$	$7.2^{+0.1}_{-0.1}$	$0.4^{+0.1}_{-0.1}$	$-2.4^{+0.1}_{-0.1}$	$-1.09^{+0.04}_{-0.04}$	–	0	1
PAR1199-18617	177.47357	22.50325	28.0	$8.2^{+0.2}_{-0.2}$	$-21.4^{+0.1}_{-0.1}$	$8.3^{+0.1}_{-0.1}$	$0.5^{+0.1}_{-0.1}$	$-2.4^{+0.1}_{-0.1}$	$-0.49^{+0.16}_{-0.16}$	–	0	0
CEERS1-14500	214.99438	52.989376	27.2	8.81	$-19.9^{+0.1}_{-0.1}$	$9.1^{+0.1}_{-0.1}$	$0.8^{+0.1}_{-0.1}$	$-2.6^{+0.2}_{-0.1}$	$-0.90^{+0.02}_{-0.02}$	–	0	1
CEERS1-16530	215.01169	52.988289	26.7	8.88	$-20.4^{+0.1}_{-0.1}$	$9.2^{+0.5}_{-0.5}$	$1.1^{+0.1}_{-0.1}$	$-2.4^{+0.1}_{-0.1}$	$-0.64^{+0.01}_{-0.01}$	–	0	0
CEERS5-25569	214.93858	52.911755	27.0	8.76	$-20.8^{+0.1}_{-0.1}$	$9.2^{+0.1}_{-0.1}$	$0.9^{+0.1}_{-0.1}$	$-2.2^{+0.1}_{-0.1}$	$-0.78^{+0.12}_{-0.12}$	–	0	0
CEERS6-13869	214.88295	52.840424	26.7	7.83	$-20.6^{+0.1}_{-0.1}$	$8.4^{+0.1}_{-0.1}$	$1.0^{+0.1}_{-0.1}$	$-2.3^{+0.1}_{-0.1}$	$-1.00^{+0.04}_{-0.04}$	–	0	1
CEERS8-9615	215.03539	52.890678	25.3	8.68	$-21.7^{+0.1}_{-0.1}$	$9.6^{+0.1}_{-0.1}$	$2.0^{+0.1}_{-0.1}$	$-1.8^{+0.1}_{-0.1}$	$-0.25^{+0.05}_{-0.05}$	0.8 ± 0.1	0	0
CEERS10-764	214.84309	52.747894	26.9	7.51	$-19.7^{+0.1}_{-0.1}$	$8.6^{+0.2}_{-0.2}$	$0.9^{+0.1}_{-0.1}$	$-2.5^{+0.1}_{-0.1}$	$-0.34^{+0.04}_{-0.04}$	–	0	0
CEERS10-9035	214.81206	52.746761	26.8	7.48	$-19.9^{+0.1}_{-0.1}$	$8.2^{+0.1}_{-0.1}$	$0.9^{+0.1}_{-0.1}$	$-2.4^{+0.1}_{-0.1}$	$-0.09^{+0.02}_{-0.02}$	–	0	0
CEERS10-12158	214.80606	52.750881	27.6	7.65	$-19.3^{+0.1}_{-0.1}$	$9.4^{+0.1}_{-0.1}$	$0.9^{+0.2}_{-0.2}$	$-1.9^{+0.2}_{-0.2}$	$-0.48^{+0.04}_{-0.04}$	–	0	0
F115W-dropout												
A2744-415	3.6375601	-30.449146	26.9	$10.3^{+0.6}_{-0.7}$	$-20.1^{+0.1}_{-0.1}$	$8.5^{+0.2}_{-0.2}$	$1.1^{+0.1}_{-0.1}$	$-2.5^{+0.2}_{-0.2}$	$-0.48^{+0.05}_{-0.05}$	–	0	0
A2744-10442	3.5925007	-30.401461	30.2	$10.3^{+0.4}_{-0.6}$	$-17.1^{+0.1}_{-0.1}$	$8.0^{+0.4}_{-0.4}$	$-0.3^{+0.1}_{-0.1}$	$-2.5^{+0.1}_{-0.1}$	$-1.61^{+0.30}_{-0.30}$	–	0	1
A2744-10587	3.595001	-30.400736	30.1	9.79	$-19.0^{+0.1}_{-0.1}$	$7.4^{+0.2}_{-0.2}$	$-0.2^{+0.1}_{-0.1}$	$-2.1^{+0.1}_{-0.1}$	$-1.25^{+0.48}_{-0.48}$	–	0	1
A2744-17600	3.5407965	-30.380466	28.8	$12.1^{+0.4}_{-0.3}$	$-18.6^{+0.1}_{-0.1}$	$8.6^{+0.3}_{-0.3}$	$0.9^{+0.2}_{-0.2}$	$-1.6^{+0.2}_{-0.2}$	$-0.91^{+0.22}_{-0.22}$	–	0	0
A2744-18782	3.5670605	-30.377871	28.6	$10.1^{+0.4}_{-0.5}$	$-19.0^{+0.1}_{-0.1}$	$7.8^{+0.1}_{-0.1}$	$0.5^{+0.1}_{-0.1}$	$-2.0^{+0.1}_{-0.1}$	$-1.00^{+0.20}_{-0.20}$	–	0	0
A2744-21342	3.5119276	-30.371861	27.5	$11.0^{+0.2}_{-0.2}$	$-19.7^{+0.1}_{-0.1}$	$9.2^{+0.2}_{-0.2}$	$0.9^{+0.1}_{-0.1}$	$-2.1^{+0.1}_{-0.1}$	$-0.70^{+0.02}_{-0.02}$	–	0	0
A2744-26963	3.5901072	-30.359735	29.2	$10.5^{+0.3}_{-0.4}$	$-18.6^{+0.1}_{-0.1}$	$7.6^{+0.3}_{-0.3}$	$0.2^{+0.1}_{-0.1}$	$-2.7^{+0.1}_{-0.1}$	$-1.95^{+0.26}_{-0.26}$	–	0	1

Table 5 continued

Table 5 (continued)

ID	R.A.	Decl.	m_{UV}	z^\dagger	M_{UV}	M_*	SFR	β_{UV}	$R_{e,maj}$	[O III]/H β	f_{gal}^*	f_{com}^*
	deg.	deg.	mag		mag	$\log M_\odot$	$\log M_\odot/\text{yr}$		log kpc	log		
A2744-33433	3.4787576	-30.345522	28.0	$10.6^{+0.5}_{-0.6}$	$-19.3^{+0.1}_{-0.1}$	$8.1^{+0.3}_{-0.3}$	$0.7^{+0.1}_{-0.1}$	$-2.1^{+0.1}_{-0.1}$	$-1.03^{+0.06}_{-0.06}$	–	0	1
A2744-40815	3.4514265	-30.3218	27.5	$10.7^{+0.4}_{-0.5}$	$-20.4^{+0.1}_{-0.1}$	$8.8^{+0.4}_{-0.4}$	$0.8^{+0.1}_{-0.1}$	$-2.5^{+0.1}_{-0.1}$	$-0.59^{+0.05}_{-0.05}$	–	0	0
A2744-41081	3.4513645	-30.320717	27.8	$10.4^{+0.5}_{-0.7}$	$-20.0^{+0.1}_{-0.1}$	$8.7^{+0.3}_{-0.3}$	$0.7^{+0.1}_{-0.1}$	$-2.6^{+0.1}_{-0.1}$	$-1.28^{+0.08}_{-0.08}$	–	0	1
PRIMERUDS-205	34.245892	-5.3258433	26.7	$10.9^{+0.2}_{-0.2}$	$-20.8^{+0.1}_{-0.1}$	$9.0^{+1.1}_{-1.1}$	$1.1^{+0.1}_{-0.1}$	$-2.4^{+0.1}_{-0.1}$	$-0.51^{+0.27}_{-0.27}$	–	0	0
PRIMERUDS-1590	34.342319	-5.3219562	27.1	$11.7^{+0.6}_{-0.5}$	$-20.2^{+0.1}_{-0.1}$	$9.0^{+0.1}_{-0.1}$	$1.1^{+0.1}_{-0.1}$	$-2.2^{+0.2}_{-0.2}$	$-0.26^{+0.05}_{-0.05}$	–	0	0
PRIMERUDS-7273	34.495377	-5.3158555	26.5	$11.0^{+0.3}_{-0.8}$	$-21.3^{+0.1}_{-0.1}$	$8.7^{+0.3}_{-0.3}$	$1.5^{+0.1}_{-0.1}$	$-1.9^{+0.1}_{-0.1}$	$-0.27^{+0.03}_{-0.03}$	–	0	0
PRIMERUDS-30091	34.291264	-5.3028331	27.1	$11.5^{+0.7}_{-0.8}$	$-19.2^{+0.1}_{-0.2}$	$8.7^{+0.5}_{-0.5}$	$1.1^{+0.1}_{-0.1}$	$-2.6^{+0.3}_{-0.2}$	$-0.16^{+0.04}_{-0.04}$	–	0	0
PRIMERUDS-39300	34.520939	-5.2926512	27.1	$10.3^{+0.8}_{-0.8}$	$-20.3^{+0.1}_{-0.1}$	$9.7^{+0.1}_{-0.1}$	$1.0^{+0.1}_{-0.1}$	$-2.2^{+0.1}_{-0.1}$	$-0.73^{+0.03}_{-0.03}$	–	0	0
PRIMERUDS-63112	34.434963	-5.2711263	26.7	$9.7^{+0.8}_{-0.3}$	$-20.0^{+0.1}_{-0.1}$	$9.3^{+0.1}_{-0.1}$	$1.4^{+0.1}_{-0.1}$	$-1.9^{+0.1}_{-0.1}$	$-0.56^{+0.02}_{-0.02}$	–	0	0
PRIMERUDS-86045	34.324715	-5.2407479	25.9	$10.6^{+0.7}_{-1.4}$	$-18.4^{+0.1}_{-0.1}$	$9.3^{+0.6}_{-0.6}$	$1.4^{+0.1}_{-0.1}$	$-2.6^{+0.2}_{-0.1}$	$0.14^{+0.03}_{-0.03}$	–	0	0
PRIMERUDS-111456	34.465179	-5.2177382	26.5	$10.3^{+0.5}_{-0.7}$	$-20.7^{+0.1}_{-0.1}$	$8.5^{+0.2}_{-0.2}$	$1.2^{+0.1}_{-0.1}$	$-2.6^{+0.1}_{-0.2}$	$-0.31^{+0.16}_{-0.16}$	–	0	0
PRIMERUDS-121885	34.322758	-5.2139339	26.3	$10.9^{+0.3}_{-0.3}$	$-19.6^{+0.1}_{-0.1}$	$10.4^{+0.1}_{-0.1}$	$1.6^{+0.1}_{-0.1}$	$-1.9^{+0.1}_{-0.1}$	$-0.01^{+0.03}_{-0.03}$	–	0	0
PRIMERUDS-129096	34.293144	-5.2113194	26.8	$11.0^{+0.3}_{-0.3}$	$-22.9^{+0.1}_{-0.1}$	$9.0^{+0.5}_{-0.5}$	$1.3^{+0.1}_{-0.1}$	$-2.0^{+0.1}_{-0.1}$	$-0.21^{+0.04}_{-0.04}$	–	0	0
PRIMERCOS-88369	150.09601	2.4049284	27.5	$12.2^{+0.4}_{-0.5}$	$-20.8^{+0.1}_{-0.1}$	$8.3^{+0.3}_{-0.3}$	$1.1^{+0.1}_{-0.1}$	$-2.8^{+0.2}_{-0.2}$	$-0.47^{+0.13}_{-0.13}$	–	1	–
PRIMERCOS-120940	150.1929	2.4724908	26.9	$11.1^{+0.4}_{-0.5}$	$-20.3^{+0.1}_{-0.1}$	$8.1^{+0.2}_{-0.2}$	$1.1^{+0.1}_{-0.1}$	$-2.6^{+0.2}_{-0.1}$	$-0.17^{+0.36}_{-0.36}$	–	0	0
PRIMERCOS-124789	150.14424	2.4815228	26.3	$11.3^{+0.2}_{-0.2}$	$-21.7^{+0.1}_{-0.1}$	$8.9^{+0.1}_{-0.1}$	$1.7^{+0.1}_{-0.1}$	$-1.9^{+0.1}_{-0.1}$	$-0.43^{+0.02}_{-0.02}$	–	0	0
NGDEEP-31868	53.245544	-27.814308	28.0	$10.4^{+0.3}_{-0.6}$	$-19.5^{+0.1}_{-0.1}$	$8.2^{+0.4}_{-0.4}$	$0.7^{+0.1}_{-0.1}$	$-2.7^{+0.1}_{-0.1}$	$-0.44^{+0.03}_{-0.03}$	–	0	0
JADESGDS-1006	53.166012	-27.836111	28.4	$10.5^{+0.6}_{-0.9}$	$-18.9^{+0.1}_{-0.1}$	$9.0^{+0.2}_{-0.2}$	$0.5^{+0.1}_{-0.1}$	$-2.3^{+0.1}_{-0.1}$	$-1.09^{+0.05}_{-0.05}$	–	0	1
JADESGDS-1324	53.165936	-27.834238	27.7	$10.9^{+0.3}_{-0.3}$	$-19.6^{+0.1}_{-0.1}$	$8.7^{+0.2}_{-0.2}$	$0.8^{+0.1}_{-0.1}$	$-2.6^{+0.1}_{-0.1}$	$-0.52^{+0.06}_{-0.06}$	–	0	0
JADESGDS-4338	53.145283	-27.823597	28.5	$10.8^{+0.5}_{-0.5}$	$-18.5^{+0.1}_{-0.1}$	$7.9^{+0.2}_{-0.2}$	$0.5^{+0.1}_{-0.1}$	$-2.2^{+0.1}_{-0.2}$	$-0.44^{+0.04}_{-0.04}$	–	0	0
JADESGDS-5148	53.166344	-27.821558	28.9	12.63	$-18.7^{+0.1}_{-0.1}$	$8.6^{+0.2}_{-0.2}$	$0.5^{+0.1}_{-0.1}$	$-2.1^{+0.1}_{-0.1}$	$-0.73^{+0.04}_{-0.04}$	–	0	0
JADESGDS-9606	53.173447	-27.81217	29.1	$10.4^{+0.6}_{-0.8}$	$-17.8^{+0.1}_{-0.1}$	$8.5^{+0.8}_{-0.8}$	$0.2^{+0.1}_{-0.1}$	$-2.2^{+0.2}_{-0.2}$	$-0.51^{+0.04}_{-0.04}$	–	0	0
JADESGDS-32040	53.164761	-27.774624	28.3	11.67	$-19.5^{+0.1}_{-0.1}$	$8.4^{+0.2}_{-0.2}$	$0.7^{+0.1}_{-0.1}$	$-2.0^{+0.1}_{-0.1}$	$-0.83^{+0.21}_{-0.21}$	–	0	0
JADESGDS-33832	53.18993	-27.771496	28.9	$11.8^{+0.7}_{-0.5}$	$-18.1^{+0.1}_{-0.1}$	$7.6^{+0.2}_{-0.2}$	$0.3^{+0.1}_{-0.1}$	$-2.8^{+0.1}_{-0.2}$	$-0.32^{+0.04}_{-0.04}$	–	0	0
JADESGDS-45484	53.190506	-27.749823	28.5	$12.3^{+0.4}_{-0.4}$	$-19.0^{+0.1}_{-0.1}$	$7.6^{+0.2}_{-0.2}$	$0.5^{+0.1}_{-0.1}$	$-2.9^{+0.2}_{-0.1}$	$-1.06^{+0.05}_{-0.05}$	–	0	1
JADESGDS-46071	53.156372	-27.748444	29.3	$10.1^{+0.5}_{-0.6}$	$-18.7^{+0.1}_{-0.1}$	$8.1^{+0.1}_{-0.1}$	$0.1^{+0.1}_{-0.1}$	$-2.5^{+0.1}_{-0.1}$	$-1.19^{+0.22}_{-0.22}$	–	0	1
CEERS2-22626	214.9066	52.945515	27.8	$11.8^{+0.5}_{-0.5}$	$-20.6^{+0.1}_{-0.1}$	$9.7^{+0.1}_{-0.1}$	$1.0^{+0.2}_{-0.2}$	$-2.0^{+0.2}_{-0.2}$	$-0.39^{+0.16}_{-0.16}$	–	0	0
CEERS4-1384	214.80342	52.77536	27.6	$11.8^{+0.6}_{-0.6}$	$-19.7^{+0.1}_{-0.1}$	$8.2^{+0.4}_{-0.4}$	$0.8^{+0.1}_{-0.1}$	$-2.5^{+0.2}_{-0.2}$	$-0.42^{+0.03}_{-0.03}$	–	0	0
CEERS4-15984	214.73253	52.758087	27.8	10.01	$-19.6^{+0.1}_{-0.1}$	$8.1^{+0.1}_{-0.1}$	$0.7^{+0.1}_{-0.1}$	$-2.5^{+0.1}_{-0.1}$	$-0.77^{+0.04}_{-0.04}$	–	0	0
CEERS5-19423	214.97729	52.926521	27.3	$10.3^{+0.6}_{-0.6}$	$-20.3^{+0.1}_{-0.1}$	$8.3^{+0.3}_{-0.3}$	$1.0^{+0.1}_{-0.1}$	$-2.1^{+0.1}_{-0.1}$	$-0.96^{+0.02}_{-0.02}$	–	0	1
CEERS7-32002	215.15154	52.975494	28.2	$11.4^{+0.5}_{-0.4}$	$-21.0^{+0.1}_{-0.1}$	$8.0^{+0.5}_{-0.5}$	$0.6^{+0.1}_{-0.1}$	$-2.5^{+0.1}_{-0.2}$	$-0.75^{+0.08}_{-0.08}$	–	0	0
CEERS9-21898	214.93204	52.841896	27.4	$10.6^{+0.5}_{-0.6}$	$-20.5^{+0.1}_{-0.1}$	$8.2^{+0.2}_{-0.2}$	$0.9^{+0.1}_{-0.1}$	$-2.8^{+0.2}_{-0.2}$	$-0.27^{+0.03}_{-0.03}$	–	0	0
CEERS9-27488	214.88596	52.819065	27.7	$10.2^{+0.6}_{-0.5}$	$-19.7^{+0.1}_{-0.1}$	$8.6^{+0.5}_{-0.5}$	$0.7^{+0.1}_{-0.1}$	$-2.7^{+0.1}_{-0.1}$	$-0.67^{+0.05}_{-0.05}$	–	0	0
CEERS10-5233	214.81184	52.737122	26.9	9.77	$-19.8^{+0.1}_{-0.1}$	$9.4^{+0.1}_{-0.1}$	$1.2^{+0.1}_{-0.1}$	$-1.9^{+0.1}_{-0.1}$	$-0.26^{+0.03}_{-0.03}$	–	0	0
CEERS10-8265	214.81711	52.74836	27.2	$10.8^{+0.3}_{-0.5}$	$-20.1^{+0.1}_{-0.1}$	$8.5^{+0.3}_{-0.3}$	$1.3^{+0.2}_{-0.2}$	$-1.8^{+0.1}_{-0.1}$	$-0.82^{+0.03}_{-0.03}$	–	0	0
F150W-dropout												
PRIMERCOS-38203	150.1942	2.3099968	27.4	$13.8^{+1.1}_{-1.0}$	$-20.0^{+0.1}_{-0.1}$	$8.1^{+0.1}_{-0.1}$	$1.1^{+0.1}_{-0.1}$	$-3.0^{+0.2}_{-0.1}$	$-0.43^{+0.03}_{-0.03}$	–	0	0
JADESGDS-30934	53.149883	-27.776503	29.2	13.20	$-18.3^{+0.1}_{-0.1}$	$7.7^{+0.4}_{-0.4}$	$0.3^{+0.1}_{-0.1}$	$-2.6^{+0.2}_{-0.2}$	$-0.88^{+0.04}_{-0.04}$	–	0	1

NOTE— List of our final sources selected in Sec. 4.1. Measurements are quoted with 1σ error. † : Photometric redshift. Errors are omitted for objects with spectroscopic redshift measurements. f_{gal} : = 1 when flagged in the `galfit` analysis. f_{com} : = 1 when classified as compact (Sec. 4.4).

REFERENCES

- Akins, H. B., Casey, C. M., Allen, N., et al. 2023, arXiv e-prints, arXiv:2304.12347, doi: [10.48550/arXiv.2304.12347](https://doi.org/10.48550/arXiv.2304.12347)
- Allen, M. G., Groves, B. A., Dopita, M. A., Sutherland, R. S., & Kewley, L. J. 2008, *ApJS*, 178, 20, doi: [10.1086/589652](https://doi.org/10.1086/589652)
- Allen, R. J., Kacprzak, G. G., Glazebrook, K., et al. 2017, *ApJL*, 834, L11, doi: [10.3847/2041-8213/834/2/L11](https://doi.org/10.3847/2041-8213/834/2/L11)
- Arrabal Haro, P., Dickinson, M., Finkelstein, S. L., et al. 2023a, arXiv e-prints, arXiv:2303.15431, doi: [10.48550/arXiv.2303.15431](https://doi.org/10.48550/arXiv.2303.15431)
- . 2023b, arXiv e-prints, arXiv:2304.05378, doi: [10.48550/arXiv.2304.05378](https://doi.org/10.48550/arXiv.2304.05378)
- Astropy Collaboration, Robitaille, T. P., Tollerud, E. J., et al. 2013, *A&A*, 558, A33, doi: [10.1051/0004-6361/201322068](https://doi.org/10.1051/0004-6361/201322068)
- Astropy Collaboration, Price-Whelan, A. M., Sipőcz, B. M., et al. 2018, *AJ*, 156, 123, doi: [10.3847/1538-3881/aabc4f](https://doi.org/10.3847/1538-3881/aabc4f)
- Astropy Collaboration, Price-Whelan, A. M., Lim, P. L., et al. 2022, *ApJ*, 935, 167, doi: [10.3847/1538-4357/ac7c74](https://doi.org/10.3847/1538-4357/ac7c74)
- Bagley, M. B., Pirzkal, N., Finkelstein, S. L., et al. 2023a, arXiv e-prints, arXiv:2302.05466, doi: [10.48550/arXiv.2302.05466](https://doi.org/10.48550/arXiv.2302.05466)
- Bagley, M. B., Finkelstein, S. L., Koekemoer, A. M., et al. 2023b, *ApJL*, 946, L12, doi: [10.3847/2041-8213/acbb08](https://doi.org/10.3847/2041-8213/acbb08)
- Bergamini, P., Acebron, A., Grillo, C., et al. 2023a, *ApJ*, 952, 84, doi: [10.3847/1538-4357/acd643](https://doi.org/10.3847/1538-4357/acd643)
- . 2023b, *A&A*, 670, A60, doi: [10.1051/0004-6361/202244575](https://doi.org/10.1051/0004-6361/202244575)
- Bertin, E., & Arnouts, S. 1996, *A&AS*, 117, 393
- Bezanson, R., Labbe, I., Whitaker, K. E., et al. 2022, arXiv e-prints, arXiv:2212.04026, <https://arxiv.org/abs/2212.04026>
- Birnboim, Y., & Dekel, A. 2003, *MNRAS*, 345, 349, doi: [10.1046/j.1365-8711.2003.06955.x](https://doi.org/10.1046/j.1365-8711.2003.06955.x)
- Boucaud, A., Bocchio, M., Abergel, A., et al. 2016, *A&A*, 596, A63, doi: [10.1051/0004-6361/201629080](https://doi.org/10.1051/0004-6361/201629080)
- Bouwens, R., Illingworth, G., Oesch, P., et al. 2023a, *MNRAS*, doi: [10.1093/mnras/stad1014](https://doi.org/10.1093/mnras/stad1014)
- . 2023b, *MNRAS*, 523, 1009, doi: [10.1093/mnras/stad1014](https://doi.org/10.1093/mnras/stad1014)
- Bouwens, R. J., Illingworth, G. D., van Dokkum, P. G., et al. 2022, *ApJ*, 927, 81, doi: [10.3847/1538-4357/ac4791](https://doi.org/10.3847/1538-4357/ac4791)
- Bradley, L. D., Trenti, M., Oesch, P. A., et al. 2012, *ApJ*, 760, 108, doi: [10.1088/0004-637X/760/2/108](https://doi.org/10.1088/0004-637X/760/2/108)
- Braglia, F. G., Pierini, D., Biviano, A., & Böhringer, H. 2009, *A&A*, 500, 947, doi: [10.1051/0004-6361/200811589](https://doi.org/10.1051/0004-6361/200811589)
- Brammer, G. B., van Dokkum, P. G., & Coppi, P. 2008, *ApJ*, 686, 1503, doi: [10.1086/591786](https://doi.org/10.1086/591786)
- Bruce, V. A., Dunlop, J. S., Cirasuolo, M., et al. 2012, *MNRAS*, 427, 1666, doi: [10.1111/j.1365-2966.2012.22087.x](https://doi.org/10.1111/j.1365-2966.2012.22087.x)
- Bullock, J. S., Dekel, A., Kolatt, T. S., et al. 2001a, *ApJ*, 555, 240, doi: [10.1086/321477](https://doi.org/10.1086/321477)
- Bullock, J. S., Kolatt, T. S., Sigad, Y., et al. 2001b, *MNRAS*, 321, 559, doi: [10.1046/j.1365-8711.2001.04068.x](https://doi.org/10.1046/j.1365-8711.2001.04068.x)
- Bunker, A. J., Cameron, A. J., Curtis-Lake, E., et al. 2023, arXiv e-prints, arXiv:2306.02467, doi: [10.48550/arXiv.2306.02467](https://doi.org/10.48550/arXiv.2306.02467)
- Byler, N., Dalcanton, J. J., Conroy, C., & Johnson, B. D. 2017, *ApJ*, 840, 44, doi: [10.3847/1538-4357/aa6c66](https://doi.org/10.3847/1538-4357/aa6c66)
- Calvi, V., Trenti, M., Stiavelli, M., et al. 2016, *ApJ*, 817, 120, doi: [10.3847/0004-637X/817/2/120](https://doi.org/10.3847/0004-637X/817/2/120)
- Cappellari, M. 2013, *ApJL*, 778, L2, doi: [10.1088/2041-8205/778/1/L2](https://doi.org/10.1088/2041-8205/778/1/L2)
- Castellano, M., Pentericci, L., Cupani, G., et al. 2022, *A&A*, 662, A115, doi: [10.1051/0004-6361/202243348](https://doi.org/10.1051/0004-6361/202243348)
- Chabrier, G. 2003, *PASP*, 115, 763, doi: [10.1086/376392](https://doi.org/10.1086/376392)
- Chambers, K. C., Magnier, E. A., Metcalfe, N., et al. 2016, arXiv e-prints, arXiv:1612.05560, doi: [10.48550/arXiv.1612.05560](https://doi.org/10.48550/arXiv.1612.05560)
- Conroy, C., Gunn, J. E., & White, M. 2009, *ApJ*, 699, 486, doi: [10.1088/0004-637X/699/1/486](https://doi.org/10.1088/0004-637X/699/1/486)
- Conselice, C. J., Grogin, N. A., Jogee, S., et al. 2004, *ApJL*, 600, L139, doi: [10.1086/378556](https://doi.org/10.1086/378556)
- Costantin, L., Pérez-González, P. G., Vega-Ferrero, J., et al. 2023, *ApJ*, 946, 71, doi: [10.3847/1538-4357/acb926](https://doi.org/10.3847/1538-4357/acb926)
- Curtis-Lake, E., McLure, R. J., Dunlop, J. S., et al. 2016, *MNRAS*, 457, 440, doi: [10.1093/mnras/stv3017](https://doi.org/10.1093/mnras/stv3017)
- Curtis-Lake, E., Carniani, S., Cameron, A., et al. 2023, *Nature Astronomy*, 7, 622, doi: [10.1038/s41550-023-01918-w](https://doi.org/10.1038/s41550-023-01918-w)
- Daddi, E., Elbaz, D., Walter, F., et al. 2010, *ApJL*, 714, L118, doi: [10.1088/2041-8205/714/1/L118](https://doi.org/10.1088/2041-8205/714/1/L118)
- Dekel, A., & Birnboim, Y. 2006, *MNRAS*, 368, 2, doi: [10.1111/j.1365-2966.2006.10145.x](https://doi.org/10.1111/j.1365-2966.2006.10145.x)
- Dopita, M. A., Pereira, M., Kewley, L. J., & Capaccioni, M. 2002, *ApJS*, 143, 47, doi: [10.1086/342624](https://doi.org/10.1086/342624)
- Eisenstein, D. J., Willott, C., Alberts, S., et al. 2023, arXiv e-prints, arXiv:2306.02465, doi: [10.48550/arXiv.2306.02465](https://doi.org/10.48550/arXiv.2306.02465)
- Ferguson, H. C., Dickinson, M., Giavalisco, M., et al. 2004, *ApJL*, 600, L107, doi: [10.1086/378578](https://doi.org/10.1086/378578)
- Finkelstein, S. L., Bagley, M. B., Haro, P. A., et al. 2022, *ApJL*, 940, L55, doi: [10.3847/2041-8213/ac966e](https://doi.org/10.3847/2041-8213/ac966e)
- Finkelstein, S. L., Bagley, M. B., Ferguson, H. C., et al. 2023, *ApJL*, 946, L13, doi: [10.3847/2041-8213/acade4](https://doi.org/10.3847/2041-8213/acade4)

- Flores Velázquez, J. A., Gurvich, A. B., Faucher-Giguère, C.-A., et al. 2021, *MNRAS*, 501, 4812, doi: [10.1093/mnras/staa3893](https://doi.org/10.1093/mnras/staa3893)
- Foreman-Mackey, D., Hogg, D. W., Lang, D., & Goodman, J. 2013, *PASP*, 125, 306, doi: [10.1086/670067](https://doi.org/10.1086/670067)
- Foreman-Mackey, D., Sick, J., & Johnson, B. 2014, doi: [10.5281/zenodo.12157](https://doi.org/10.5281/zenodo.12157)
- Fujimoto, S., Ouchi, M., Nakajima, K., et al. 2022, arXiv e-prints, arXiv:2212.06863, doi: [10.48550/arXiv.2212.06863](https://doi.org/10.48550/arXiv.2212.06863)
- Fujimoto, S., Arrabal Haro, P., Dickinson, M., et al. 2023, *ApJL*, 949, L25, doi: [10.3847/2041-8213/acd2d9](https://doi.org/10.3847/2041-8213/acd2d9)
- Fukugita, M., Ichikawa, T., Gunn, J. E., et al. 1996, *AJ*, 111, 1748, doi: [10.1086/117915](https://doi.org/10.1086/117915)
- Furtak, L. J., Zitrin, A., Plat, A., et al. 2023, *ApJ*, 952, 142, doi: [10.3847/1538-4357/acdc9d](https://doi.org/10.3847/1538-4357/acdc9d)
- Grogin, N. A., Kocevski, D. D., Faber, S. M., et al. 2011, *ApJS*, 197, 35, doi: [10.1088/0067-0049/197/2/35](https://doi.org/10.1088/0067-0049/197/2/35)
- Guo, Y., Giavalisco, M., Ferguson, H. C., Cassata, P., & Koekemoer, A. M. 2012, *ApJ*, 757, 120, doi: [10.1088/0004-637X/757/2/120](https://doi.org/10.1088/0004-637X/757/2/120)
- Guo, Y., McIntosh, D. H., Mo, H. J., et al. 2009, *MNRAS*, 398, 1129, doi: [10.1111/j.1365-2966.2009.15223.x](https://doi.org/10.1111/j.1365-2966.2009.15223.x)
- Hainline, K. N., Johnson, B. D., Robertson, B., et al. 2023, arXiv e-prints, arXiv:2306.02468, doi: [10.48550/arXiv.2306.02468](https://doi.org/10.48550/arXiv.2306.02468)
- Harikane, Y., Nakajima, K., Ouchi, M., et al. 2023a, arXiv e-prints, arXiv:2304.06658, doi: [10.48550/arXiv.2304.06658](https://doi.org/10.48550/arXiv.2304.06658)
- Harikane, Y., Zhang, Y., Nakajima, K., et al. 2023b, arXiv e-prints, arXiv:2303.11946, doi: [10.48550/arXiv.2303.11946](https://doi.org/10.48550/arXiv.2303.11946)
- Harris, C. R., Millman, K. J., van der Walt, S. J., et al. 2020, *Nature*, 585, 357, doi: [10.1038/s41586-020-2649-2](https://doi.org/10.1038/s41586-020-2649-2)
- Hasinger, G., Capak, P., Salvato, M., et al. 2018, *ApJ*, 858, 77, doi: [10.3847/1538-4357/aabacf](https://doi.org/10.3847/1538-4357/aabacf)
- Ho, L. C., Filippenko, A. V., & Sargent, W. L. W. 1997, *ApJS*, 112, 315, doi: [10.1086/313041](https://doi.org/10.1086/313041)
- Holwerda, B. W., Bouwens, R., Oesch, P., et al. 2015, *ApJ*, 808, 6, doi: [10.1088/0004-637X/808/1/6](https://doi.org/10.1088/0004-637X/808/1/6)
- Hoopes, C. G., Heckman, T. M., Salim, S., et al. 2007, *ApJS*, 173, 441, doi: [10.1086/516644](https://doi.org/10.1086/516644)
- Huang, K.-H., Ferguson, H. C., Ravindranath, S., & Su, J. 2013, *The Astrophysical Journal*, 765, 68, doi: [10.1088/0004-637X/765/1/68](https://doi.org/10.1088/0004-637X/765/1/68)
- Huertas-Company, M., Iyer, K. G., Angeloudi, E., et al. 2023, arXiv e-prints, arXiv:2305.02478, doi: [10.48550/arXiv.2305.02478](https://doi.org/10.48550/arXiv.2305.02478)
- Illingworth, G. 2009, *Galaxies at z=7-10 in the Reionization Epoch: Luminosity Functions to $\mu 0.2L^*$ from Deep IR Imaging of the HUDF and HUDF05 Fields*, HST Proposal ID 11563. Cycle 17
- Ishikawa, Y., Morishita, T., Stiavelli, M., et al. 2022, *ApJ*, 936, 167, doi: [10.3847/1538-4357/ac8874](https://doi.org/10.3847/1538-4357/ac8874)
- Ito, K., Valentino, F., Brammer, G., et al. 2023, arXiv e-prints, arXiv:2307.06994, doi: [10.48550/arXiv.2307.06994](https://doi.org/10.48550/arXiv.2307.06994)
- Jansen, R. A., & Windhorst, R. A. 2018, *PASP*, 130, 124001, doi: [10.1088/1538-3873/aae476](https://doi.org/10.1088/1538-3873/aae476)
- Jones, T., Sanders, R., Chen, Y., et al. 2023, arXiv e-prints, arXiv:2301.07126, doi: [10.48550/arXiv.2301.07126](https://doi.org/10.48550/arXiv.2301.07126)
- Juneau, S., Dickinson, M., Alexander, D. M., & Salim, S. 2011, *ApJ*, 736, 104, doi: [10.1088/0004-637X/736/2/104](https://doi.org/10.1088/0004-637X/736/2/104)
- Juneau, S., Bournaud, F., Charlot, S., et al. 2014, *ApJ*, 788, 88, doi: [10.1088/0004-637X/788/1/88](https://doi.org/10.1088/0004-637X/788/1/88)
- Kauffmann, G., Heckman, T. M., White, S. D. M., et al. 2003, *MNRAS*, 341, 54, doi: [10.1046/j.1365-8711.2003.06292.x](https://doi.org/10.1046/j.1365-8711.2003.06292.x)
- Kawamata, R., Ishigaki, M., Shimasaku, K., Oguri, M., & Ouchi, M. 2015, *ApJ*, 804, 103, doi: [10.1088/0004-637X/804/2/103](https://doi.org/10.1088/0004-637X/804/2/103)
- Kawamata, R., Ishigaki, M., Shimasaku, K., et al. 2018, *ApJ*, 855, 4, doi: [10.3847/1538-4357/aaa6cf](https://doi.org/10.3847/1538-4357/aaa6cf)
- Kennicutt, Robert C., J. 1998, *ApJ*, 498, 541, doi: [10.1086/305588](https://doi.org/10.1086/305588)
- Kennicutt, R. C., & Evans, N. J. 2012, *ARA&A*, 50, 531, doi: [10.1146/annurev-astro-081811-125610](https://doi.org/10.1146/annurev-astro-081811-125610)
- Kocevski, D. D., Onoue, M., Inayoshi, K., et al. 2023, arXiv e-prints, arXiv:2302.00012, doi: [10.48550/arXiv.2302.00012](https://doi.org/10.48550/arXiv.2302.00012)
- Koekemoer, A. M., Faber, S. M., Ferguson, H. C., et al. 2011, *ApJS*, 197, 36, doi: [10.1088/0067-0049/197/2/36](https://doi.org/10.1088/0067-0049/197/2/36)
- Labbe, I., Greene, J. E., Bezanson, R., et al. 2023, arXiv e-prints, arXiv:2306.07320, doi: [10.48550/arXiv.2306.07320](https://doi.org/10.48550/arXiv.2306.07320)
- Larson, R. L., Finkelstein, S. L., Hutchison, T. A., et al. 2022, *ApJ*, 930, 104, doi: [10.3847/1538-4357/ac5dbd](https://doi.org/10.3847/1538-4357/ac5dbd)
- Larson, R. L., Finkelstein, S. L., Kocevski, D. D., et al. 2023, arXiv e-prints, arXiv:2303.08918, doi: [10.48550/arXiv.2303.08918](https://doi.org/10.48550/arXiv.2303.08918)
- Marshall, M. A., Wilkins, S., Di Matteo, T., et al. 2022, *MNRAS*, 511, 5475, doi: [10.1093/mnras/stac380](https://doi.org/10.1093/mnras/stac380)
- Mascia, S., Pentericci, L., Calabro', A., et al. 2023, arXiv e-prints, arXiv:2301.02816, doi: [10.48550/arXiv.2301.02816](https://doi.org/10.48550/arXiv.2301.02816)
- Matthee, J., Naidu, R. P., Brammer, G., et al. 2023, arXiv e-prints, arXiv:2306.05448, doi: [10.48550/arXiv.2306.05448](https://doi.org/10.48550/arXiv.2306.05448)

- McGuire, J. T. W., Tanvir, N. R., Levan, A. J., et al. 2016, *ApJ*, 825, 135, doi: [10.3847/0004-637X/825/2/135](https://doi.org/10.3847/0004-637X/825/2/135)
- Mehta, V., Scarlata, C., Capak, P., et al. 2018, *ApJS*, 235, 36, doi: [10.3847/1538-4365/aab60c](https://doi.org/10.3847/1538-4365/aab60c)
- Merlin, E., Bonchi, A., Paris, D., et al. 2022, *ApJL*, 938, L14, doi: [10.3847/2041-8213/ac8f93](https://doi.org/10.3847/2041-8213/ac8f93)
- Miyazaki, S., Komiyama, Y., Kawanomoto, S., et al. 2018, *PASJ*, 70, S1, doi: [10.1093/pasj/psx063](https://doi.org/10.1093/pasj/psx063)
- Mo, H. J., Mao, S., & White, S. D. M. 1998, *MNRAS*, 295, 319, doi: [10.1046/j.1365-8711.1998.01227.x](https://doi.org/10.1046/j.1365-8711.1998.01227.x)
- Momcheva, I. G., Brammer, G. B., van Dokkum, P. G., et al. 2016, *ApJS*, 225, 27, doi: [10.3847/0067-0049/225/2/27](https://doi.org/10.3847/0067-0049/225/2/27)
- Morishita, T. 2021, *ApJS*, 253, 4, doi: [10.3847/1538-4365/abce67](https://doi.org/10.3847/1538-4365/abce67)
- Morishita, T. 2023, *mtakahiro/bbnpn: v1.3, v1.3*, Zenodo, doi: [10.5281/zenodo.10067906](https://doi.org/10.5281/zenodo.10067906)
- Morishita, T., Ichikawa, T., & Kajisawa, M. 2014, *ApJ*, 785, 18, doi: [10.1088/0004-637X/785/1/18](https://doi.org/10.1088/0004-637X/785/1/18)
- Morishita, T., & Stiavelli, M. 2022, arXiv e-prints, arXiv:2207.11671. <https://arxiv.org/abs/2207.11671>
- . 2023, *ApJL*, 946, L35, doi: [10.3847/2041-8213/acbf50](https://doi.org/10.3847/2041-8213/acbf50)
- Morishita, T., Abramson, L. E., Treu, T., et al. 2017, *ApJ*, 835, 254, doi: [10.3847/1538-4357/835/2/254](https://doi.org/10.3847/1538-4357/835/2/254)
- Morishita, T., Trenti, M., Stiavelli, M., et al. 2018, *ApJ*, 867, 150, doi: [10.3847/1538-4357/aae68c](https://doi.org/10.3847/1538-4357/aae68c)
- Morishita, T., Abramson, L. E., Treu, T., et al. 2019, *ApJ*, 877, 141, doi: [10.3847/1538-4357/ab1d53](https://doi.org/10.3847/1538-4357/ab1d53)
- Morishita, T., Stiavelli, M., Trenti, M., et al. 2020, *ApJ*, 904, 50, doi: [10.3847/1538-4357/abba83](https://doi.org/10.3847/1538-4357/abba83)
- Morishita, T., Roberts-Borsani, G., Treu, T., et al. 2023, *ApJL*, 947, L24, doi: [10.3847/2041-8213/acb99e](https://doi.org/10.3847/2041-8213/acb99e)
- Mosleh, M., Williams, R. J., Franx, M., & Kriek, M. 2011, *ApJ*, 727, 5, doi: [10.1088/0004-637X/727/1/5](https://doi.org/10.1088/0004-637X/727/1/5)
- Mosleh, M., Williams, R. J., Franx, M., et al. 2012, *ApJL*, 756, L12, doi: [10.1088/2041-8205/756/1/L12](https://doi.org/10.1088/2041-8205/756/1/L12)
- Murphy, E. J., Condon, J. J., Schinnerer, E., et al. 2011, *ApJ*, 737, 67, doi: [10.1088/0004-637X/737/2/67](https://doi.org/10.1088/0004-637X/737/2/67)
- Naidu, R. P., Oesch, P. A., van Dokkum, P., et al. 2022, *ApJL*, 940, L14, doi: [10.3847/2041-8213/ac9b22](https://doi.org/10.3847/2041-8213/ac9b22)
- Nakajima, K., Ouchi, M., Isobe, Y., et al. 2023, arXiv e-prints, arXiv:2301.12825, doi: [10.48550/arXiv.2301.12825](https://doi.org/10.48550/arXiv.2301.12825)
- Oesch, P. A., Stiavelli, M., Carollo, C. M., et al. 2007, *ApJ*, 671, 1212, doi: [10.1086/522423](https://doi.org/10.1086/522423)
- Oesch, P. A., Bouwens, R. J., Carollo, C. M., et al. 2010, *ApJL*, 709, L21, doi: [10.1088/2041-8205/709/1/L21](https://doi.org/10.1088/2041-8205/709/1/L21)
- Oesch, P. A., Brammer, G., van Dokkum, P. G., et al. 2016, *ApJ*, 819, 129, doi: [10.3847/0004-637X/1/2/129](https://doi.org/10.3847/0004-637X/1/2/129)
- Oke, J. B., & Gunn, J. E. 1983, *ApJ*, 266, 713, doi: [10.1086/160817](https://doi.org/10.1086/160817)
- Ono, Y., Ouchi, M., Curtis-Lake, E., et al. 2013, *ApJ*, 777, 155, doi: [10.1088/0004-637X/777/2/155](https://doi.org/10.1088/0004-637X/777/2/155)
- Ono, Y., Harikane, Y., Ouchi, M., et al. 2022, arXiv e-prints, arXiv:2208.13582, doi: [10.48550/arXiv.2208.13582](https://doi.org/10.48550/arXiv.2208.13582)
- . 2023, arXiv e-prints, arXiv:2309.02790, doi: [10.48550/arXiv.2309.02790](https://doi.org/10.48550/arXiv.2309.02790)
- Onoue, M., Inayoshi, K., Ding, X., et al. 2023, *ApJL*, 942, L17, doi: [10.3847/2041-8213/aca9d3](https://doi.org/10.3847/2041-8213/aca9d3)
- Overzier, R. A., Guo, Q., Kauffmann, G., et al. 2009, *MNRAS*, 394, 577, doi: [10.1111/j.1365-2966.2008.14264.x](https://doi.org/10.1111/j.1365-2966.2008.14264.x)
- Owers, M. S., Randall, S. W., Nulsen, P. E. J., et al. 2011, *ApJ*, 728, 27, doi: [10.1088/0004-637X/728/1/27](https://doi.org/10.1088/0004-637X/728/1/27)
- Paris, D., Merlin, E., Fontana, A., et al. 2023, arXiv e-prints, arXiv:2301.02179, doi: [10.48550/arXiv.2301.02179](https://doi.org/10.48550/arXiv.2301.02179)
- Peng, C. Y., Ho, L. C., Impey, C. D., & Rix, H.-W. 2002, *AJ*, 124, 266, doi: [10.1086/340952](https://doi.org/10.1086/340952)
- . 2010, *AJ*, 139, 2097, doi: [10.1088/0004-6256/139/6/2097](https://doi.org/10.1088/0004-6256/139/6/2097)
- Pentericci, L., McLure, R. J., Garilli, B., et al. 2018, *A&A*, 616, A174, doi: [10.1051/0004-6361/201833047](https://doi.org/10.1051/0004-6361/201833047)
- Perrin, M. D., Sivaramakrishnan, A., Lajoie, C.-P., et al. 2014, in *Society of Photo-Optical Instrumentation Engineers (SPIE) Conference Series*, Vol. 9143, *Space Telescopes and Instrumentation 2014: Optical, Infrared, and Millimeter Wave*, ed. J. Oschmann, Jacobus M., M. Clampin, G. G. Fazio, & H. A. MacEwen, 91433X, doi: [10.1117/12.2056689](https://doi.org/10.1117/12.2056689)
- Popping, G., Pillepich, A., Calistro Rivera, G., et al. 2022, *MNRAS*, 510, 3321, doi: [10.1093/mnras/stab3312](https://doi.org/10.1093/mnras/stab3312)
- Rayner, J. T., Toomey, D. W., Onaka, P. M., et al. 2003, *PASP*, 115, 362, doi: [10.1086/367745](https://doi.org/10.1086/367745)
- Reddy, N. A., Topping, M. W., Sanders, R. L., Shapley, A. E., & Brammer, G. 2023, *ApJ*, 952, 167, doi: [10.3847/1538-4357/acd754](https://doi.org/10.3847/1538-4357/acd754)
- Richard, J., Claeysens, A., Lagattuta, D., et al. 2021, *A&A*, 646, A83, doi: [10.1051/0004-6361/202039462](https://doi.org/10.1051/0004-6361/202039462)
- Rieke, M., & the JADES Collaboration. 2023, arXiv e-prints, arXiv:2306.02466, doi: [10.48550/arXiv.2306.02466](https://doi.org/10.48550/arXiv.2306.02466)
- Roberts-Borsani, G., Morishita, T., Treu, T., Leethochawalit, N., & Trenti, M. 2022a, *ApJ*, 927, 236, doi: [10.3847/1538-4357/ac4803](https://doi.org/10.3847/1538-4357/ac4803)
- Roberts-Borsani, G., Treu, T., Chen, W., et al. 2022b, arXiv e-prints, arXiv:2210.15639. <https://arxiv.org/abs/2210.15639>
- Roberts-Borsani, G., Morishita, T., Treu, T., et al. 2022c, *ApJL*, 938, L13, doi: [10.3847/2041-8213/ac8e6e](https://doi.org/10.3847/2041-8213/ac8e6e)

- Roberts-Borsani, G. W., Bouwens, R. J., Oesch, P. A., et al. 2016, *ApJ*, 823, 143, doi: [10.3847/0004-637X/823/2/143](https://doi.org/10.3847/0004-637X/823/2/143)
- Robertson, B. E., Tacchella, S., Johnson, B. D., et al. 2023, *Nature Astronomy*, 7, 611, doi: [10.1038/s41550-023-01921-1](https://doi.org/10.1038/s41550-023-01921-1)
- Roper, W. J., Lovell, C. C., Vijayan, A. P., et al. 2022a, *MNRAS*, 514, 1921, doi: [10.1093/mnras/stac1368](https://doi.org/10.1093/mnras/stac1368)
- . 2022b, *MNRAS*, 514, 1921, doi: [10.1093/mnras/stac1368](https://doi.org/10.1093/mnras/stac1368)
- Sanders, R. L., Shapley, A. E., Topping, M. W., Reddy, N. A., & Brammer, G. B. 2023, arXiv e-prints, arXiv:2303.08149, doi: [10.48550/arXiv.2303.08149](https://doi.org/10.48550/arXiv.2303.08149)
- Schlawin, E., Leisenring, J., McElwain, M. W., et al. 2021, *AJ*, 161, 115, doi: [10.3847/1538-3881/abd8d4](https://doi.org/10.3847/1538-3881/abd8d4)
- Schlegel, D. J., Finkbeiner, D. P., & Davis, M. 1998, *ApJ*, 500, 525, doi: [10.1086/305772](https://doi.org/10.1086/305772)
- Schmidt, K. B., Treu, T., Brammer, G. B., et al. 2014, *ApJL*, 782, L36, doi: [10.1088/2041-8205/782/2/L36](https://doi.org/10.1088/2041-8205/782/2/L36)
- Scoville, N. Z., Evans, A. S., Thompson, R., et al. 2000, *AJ*, 119, 991, doi: [10.1086/301248](https://doi.org/10.1086/301248)
- Sérsic, J. L. 1963, *Boletín de la Asociación Argentina de Astronomía La Plata Argentina*, 6, 41
- Shapley, A. E., Reddy, N. A., Kriek, M., et al. 2015, *ApJ*, 801, 88, doi: [10.1088/0004-637X/801/2/88](https://doi.org/10.1088/0004-637X/801/2/88)
- Shen, S., Mo, H. J., White, S. D. M., et al. 2003, *MNRAS*, 343, 978, doi: [10.1046/j.1365-8711.2003.06740.x](https://doi.org/10.1046/j.1365-8711.2003.06740.x)
- Shen, X., Borrow, J., Vogelsberger, M., et al. 2023, arXiv e-prints, arXiv:2304.06742, doi: [10.48550/arXiv.2304.06742](https://doi.org/10.48550/arXiv.2304.06742)
- Shibuya, T., Ouchi, M., & Harikane, Y. 2015, *ApJS*, 219, 15, doi: [10.1088/0067-0049/219/2/15](https://doi.org/10.1088/0067-0049/219/2/15)
- Shim, H., & Chary, R.-R. 2013, *ApJ*, 765, 26, doi: [10.1088/0004-637X/765/1/26](https://doi.org/10.1088/0004-637X/765/1/26)
- Simard, L., Mendel, J. T., Patton, D. R., Ellison, S. L., & McConnell, A. W. 2011, *ApJS*, 196, 11, doi: [10.1088/0067-0049/196/1/11](https://doi.org/10.1088/0067-0049/196/1/11)
- Skelton, R. E., Whitaker, K. E., Momcheva, I. G., et al. 2014, *ApJS*, 214, 24, doi: [10.1088/0067-0049/214/2/24](https://doi.org/10.1088/0067-0049/214/2/24)
- Smit, R., Bouwens, R. J., Labbé, I., et al. 2016, *ApJ*, 833, 254, doi: [10.3847/1538-4357/833/2/254](https://doi.org/10.3847/1538-4357/833/2/254)
- Speagle, J. S., Steinhardt, C. L., Capak, P. L., & Silverman, J. D. 2014, *ApJS*, 214, 15, doi: [10.1088/0067-0049/214/2/15](https://doi.org/10.1088/0067-0049/214/2/15)
- Steidel, C. C., Adelberger, K. L., Dickinson, M., et al. 1998, *ApJ*, 492, 428, doi: [10.1086/305073](https://doi.org/10.1086/305073)
- Stern, J., Faucher-Giguère, C.-A., Fielding, D., et al. 2021, *ApJ*, 911, 88, doi: [10.3847/1538-4357/abd776](https://doi.org/10.3847/1538-4357/abd776)
- Stiavelli, M. 2005, Searching for galaxies at $z \gtrsim 6.5$ in the Hubble Ultra Deep Field, HST Proposal ID 10632. Cycle 14
- Stiavelli, M., Morishita, T., Chiaberge, M., et al. 2023, *ApJL*, 957, L18, doi: [10.3847/2041-8213/ad0159](https://doi.org/10.3847/2041-8213/ad0159)
- Szomoru, D., Franx, M., & van Dokkum, P. G. 2012, *ApJ*, 749, 121, doi: [10.1088/0004-637X/749/2/121](https://doi.org/10.1088/0004-637X/749/2/121)
- Tacchella, S., Johnson, B. D., Robertson, B. E., et al. 2023, *MNRAS*, 522, 6236, doi: [10.1093/mnras/stad1408](https://doi.org/10.1093/mnras/stad1408)
- Tang, M., Stark, D. P., Chen, Z., et al. 2023, arXiv e-prints, arXiv:2301.07072, doi: [10.48550/arXiv.2301.07072](https://doi.org/10.48550/arXiv.2301.07072)
- Tanvir, N. R., Levan, A. J., Fruchter, A. S., et al. 2012, *ApJ*, 754, 46, doi: [10.1088/0004-637X/754/1/46](https://doi.org/10.1088/0004-637X/754/1/46)
- Trenti, M., Perna, R., Levesque, E. M., Shull, J. M., & Stocke, J. T. 2012a, *ApJL*, 749, L38, doi: [10.1088/2041-8205/749/2/L38](https://doi.org/10.1088/2041-8205/749/2/L38)
- Trenti, M., Bradley, L. D., Stiavelli, M., et al. 2012b, *ApJ*, 746, 55, doi: [10.1088/0004-637X/746/1/55](https://doi.org/10.1088/0004-637X/746/1/55)
- Treu, T., Roberts-Borsani, G., Bradac, M., et al. 2022, *ApJ*, 935, 110, doi: [10.3847/1538-4357/ac8158](https://doi.org/10.3847/1538-4357/ac8158)
- Treu, T., Calabrò, A., Castellano, M., et al. 2023, *ApJL*, 942, L28, doi: [10.3847/2041-8213/ac9283](https://doi.org/10.3847/2041-8213/ac9283)
- van der Wel, A., Bell, E. F., Häussler, B., et al. 2012, *ApJS*, 203, 24, doi: [10.1088/0067-0049/203/2/24](https://doi.org/10.1088/0067-0049/203/2/24)
- van der Wel, A., Franx, M., van Dokkum, P. G., et al. 2014, *ApJ*, 788, 28, doi: [10.1088/0004-637X/788/1/28](https://doi.org/10.1088/0004-637X/788/1/28)
- Vulcani, B., Bamford, S. P., Häußler, B., et al. 2014, *MNRAS*, 441, 1340, doi: [10.1093/mnras/stu632](https://doi.org/10.1093/mnras/stu632)
- Weaver, J. R., Davidzon, I., Toft, S., et al. 2022, arXiv e-prints, arXiv:2212.02512, doi: [10.48550/arXiv.2212.02512](https://doi.org/10.48550/arXiv.2212.02512)
- Windhorst, R. A., Cohen, S. H., Jansen, R. A., et al. 2023, *AJ*, 165, 13, doi: [10.3847/1538-3881/aca163](https://doi.org/10.3847/1538-3881/aca163)
- Wuyts, S., Förster Schreiber, N. M., van der Wel, A., et al. 2011, *ApJ*, 742, 96, doi: [10.1088/0004-637X/742/2/96](https://doi.org/10.1088/0004-637X/742/2/96)
- Yang, L., Roberts-Borsani, G., Treu, T., et al. 2021, *MNRAS*, 501, 1028, doi: [10.1093/mnras/staa3713](https://doi.org/10.1093/mnras/staa3713)
- Yang, L., Leethochawalit, N., Treu, T., et al. 2022a, *MNRAS*, 514, 1148, doi: [10.1093/mnras/stac1236](https://doi.org/10.1093/mnras/stac1236)
- Yang, L., Morishita, T., Leethochawalit, N., et al. 2022b, *ApJL*, 938, L17, doi: [10.3847/2041-8213/ac8803](https://doi.org/10.3847/2041-8213/ac8803)